Formulation and Validation of a Nonlinear Shell Element for the Analysis of Reinforced Concrete and Masonry Structures

David Burchnall

Thesis submitted to the faculty of the

Virginia Polytechnic Institute and State University

in partial fulfillment of the requirements for the degree of

Master of Science

in

Civil Engineering

Ioannis Koutromanos, Chair

Carin L. Roberts-Wollmann

Cristopher D. Moen

May 6, 2014

Blacksburg, VA

Keywords: shell element, geometric nonlinearity, reinforced concrete and masonry

Formulation and Validation of a Nonlinear Shell Element for the Analysis of Reinforced Concrete and Masonry Structures

David Burchnall

Abstract

Reinforced concrete (RC) shear wall buildings constitute a significant portion of the building inventory in many earthquake-prone regions. A similar type of structural system is fully-grouted reinforced masonry (RM) shear wall structures. The accurate determination of the nonlinear response of reinforced concrete and reinforced masonry (RC/RM) walls subjected to lateral loading is of uttermost importance for ensuring the safety of the built environment.

Analytical models provide a cost efficient and comprehensive tool to study the nonlinear response of RC/RM structures, as compared to experimental tests. Predictive models should capture nonlinear material behavior as well as the geometrically nonlinear response of RC/RM shear wall structures during major seismic events.

This thesis outlines the formulation and validation of a nonlinear shell element for the simulation of RC/RM structures. The proposed shell element enhances an existing formulation of a four-node Discrete Kirchhoff shell element through the inclusion of a corotational approach to account for geometric nonlinearities and of nonlinear material models to capture the effect of cracking and crushing in concrete or masonry and the nonlinear hysteretic behavior of reinforcing steel.

The analytical results obtained from multiple linear and nonlinear analyses are compared against theoretical solutions and experimental test data. These comparative validation studies show the enhanced shell element can satisfactorily capture the salient features of the response of nonlinear reinforced concrete/masonry shear wall structures including axial-shear-flexure interaction, damage patterns, and in-plane and out-of-plane loading.

Acknowledgements

The completion of this thesis was made possible by the support and encouragement of others. I am very grateful for the time and effort these individuals have provided to me.

First, I would like to give a special thank you to my advisor, Professor Ioannis Koutromanos, for his constant availability and vital insight on this thesis. Professor Koutromanos provided me with valuable knowledge through continued mentoring, teaching and guidance. My gratitude also goes out to the other members of my committee, Professor Cristopher Moen and Professor Carin Roberts-Wollmann, for providing instruction and guidance throughout the completion of this study. I would like to thank the Virginia Polytechnic Institute and State University Civil Engineering department and the Via family/program for providing me with the prestigious and generous Charles Via Fellowship.

I would also like to thank Professor Marios Panagiotou of UC Berkeley as well as Professor Benson Shing and Mr. Marios Mavros of UC San Diego for providing experimental data used in the validation analyses.

I am eternally grateful for my close family and friends who have been crucial in my growth as a person and an engineer. I would like to send a special thank you to my parents, John and Ruth Anne Burchnall, and my brother, Mark Burchnall, for their unceasing guidance and support. Finally, I want to thank my fiancée, Whitney Grabarz, for her continued patience and encouragement.

Table of Contents

List of Figures

List of Tables

Chapter 1: Introduction

Reinforced concrete (RC) or fully-grouted reinforced masonry (RM) shear walls are common lateral loading systems for residential and commercial buildings. These systems are made of readily available and cost efficient materials, and are intended to provide adequate strength and stiffness to control lateral displacements. However, during major seismic events, RC/RM shear walls can exhibit large nonlinear deformations causing substantial inelastic damage that may jeopardize the structural integrity of the building. Therefore, the accurate determination of the nonlinear response of reinforced concrete and masonry shear walls during such extreme load events is of uttermost importance for ensuring the safety of the built environment.

Even though experiments provide useful data on the nonlinear responses of RC/RM structures, they are often expensive, time consuming, and specimen size limited. Information from experimental tests is limited to the number and location of the installed instrumentation. Analytical models, on the other hand, provide cost effective and comprehensive tools to analyze nonlinear behavior of RC/RM shear wall structures. Predictive shear wall computational models should capture the axial-shear-flexure interaction, in-plane and out-of-plane behavior and damage patterns. Once validated with experimental results, analytical models can be used to conduct parametric studies leading to structurally efficient, cost effective, and reliable designs of civil structures.

1.1: Objective

The objective of this study is to outline the formulation of a nonlinear shell element for the analysis of RC/RM structures and to verify the element using experimental data and theoretical solutions. The proposed shell element enhances an existing formulation of a four-node Discrete Kirchhoff shell element by including (1) a corotational approach to account for geometric nonlinearities (large displacement and rotations) and (2) nonlinear material models for both concrete/masonry and reinforcing steel.

1.2: Outline of Thesis

Chapter 2 details a literature review of previous research related to the nonlinear analysis of reinforced concrete and masonry structures. Emphasis is laid on analytical models used to study the nonlinear behavior of RC/RM shear walls, slabs/panels and wall-slab building systems. Three analytical methods are examined: (1) finite element models, (2) truss models, and (3) beam models (both traditional and fiber).

Chapter 3 outlines the formulation of the proposed shell element including the kinematic assumptions, through thickness integration approach, and material models (for both concrete/masonry and steel). The corotational approach used to account for geometric nonlinearities (large displacements and rotations) is also described.

Chapter 4 presents several linear analyses of elastic beams and plates using the shell element and compares the results against benchmark analytical and theoretical results. Nonlinear simulations are also performed on elastic structures to verify the corotational approach.

In chapter 5, the proposed shell element formulations and material models are used to simulate the experimental results of a reinforced concrete column, a seven-story reinforced concrete wall-slab building slice, and a two-story reinforced masonry (fully-grouted) wall-slab

building system. In these experiments, the RC column was subjected to quasi-static cyclic loading while both the seven-story wall-slab RC building slice and the two-story RM wall-slab building system were subjected to dynamic loading recorded from earthquake ground motions. Nonlinear static analyses were conducted on models of these structures. The load-displacement response and damage patterns of the experimental tests are compared to the analytical results for validation.

Chapter 6 contains conclusions and recommendations for future research.

.

Chapter 2: Literature Review

This chapter summarizes the literature pertaining to nonlinear analysis methods for reinforced concrete/masonry shear wall structures. Fully-grouted masonry, where all voids in the masonry units are filled with grout, has a similar behavior to that of concrete and thus the same types of constitutive models can be used for both. As such, the literature in this chapter primarily focuses on nonlinear analysis of reinforced concrete structures. The available analysis methods can be broadly distinguished into three categories, namely, beam models, truss models and finite element models.

2.1: Beam Models

The first efforts to simulate nonlinear cyclic behavior of wall structures using nonlinear beam models were by Clough et al. (1965). This model captured flexure-dominated inelastic behavior by using an elasto-plastic beam element (where two plastic hinges can form) and an elastic beam in parallel. Otani and Sozen (1972) used cantilever beams in which an idealized tri-linear moment curvature relationship was implemented to account for material flexural nonlinearities. Both of these models neglected shear deformations in their formulations, and thus are most suitable to analyze slender shear walls where flexure behavior dominates the response. Takayanagi and Schobrich (1976) then accounted for shear deformations by simply reducing the shear stiffness proportionally with flexural stiffness as the shear wall behaves inelastically.

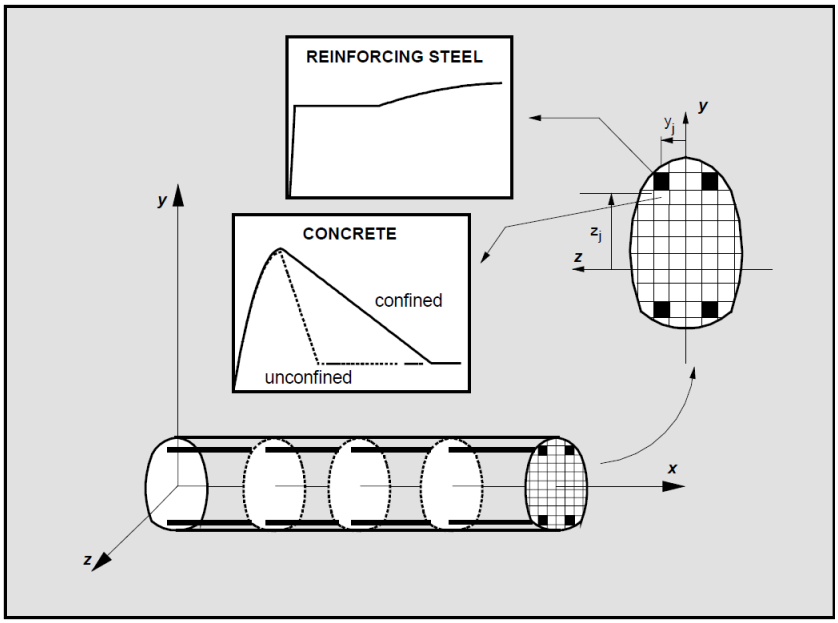

Figure 2.1: Fiber Model. Taucer, F., Spacone, E., and Filippou, F. (1991), A Fiber Beam-Column Element for Seismic Response Analysis of Reinforced Concrete Structures. Vol. 91. 17. Earthquake Engineering Research Center, College of Engineering, University of California. Used under fair use, 2014.

Mahin and Bertero (1975) proposed a new beam modeling approach called a fiber model. In a fiber beam model, the section is discretized into multiple fibers, each one assumed to be in state of uniaxial stress. Given the strain and curvature of the reference line of the beam, the strain of each fiber in a section can be determined. The stress of each fiber is then obtained, using the corresponding uniaxial material model. The axial force and bending moment of the section are calculated by summing the contributions of the fibers. Figure 2.1 provides a depiction of the fiber model. Taucer et al. (1991) also used a fiber model to analyze reinforced concrete shear walls. In this model, the resulting force and section stiffness was calculated following the flexibility approach and enforcing equilibrium and compatibility. Shear effects were neglected in the Taucer et al. model and therefore it is only applicable for the analysis of slender shear walls.

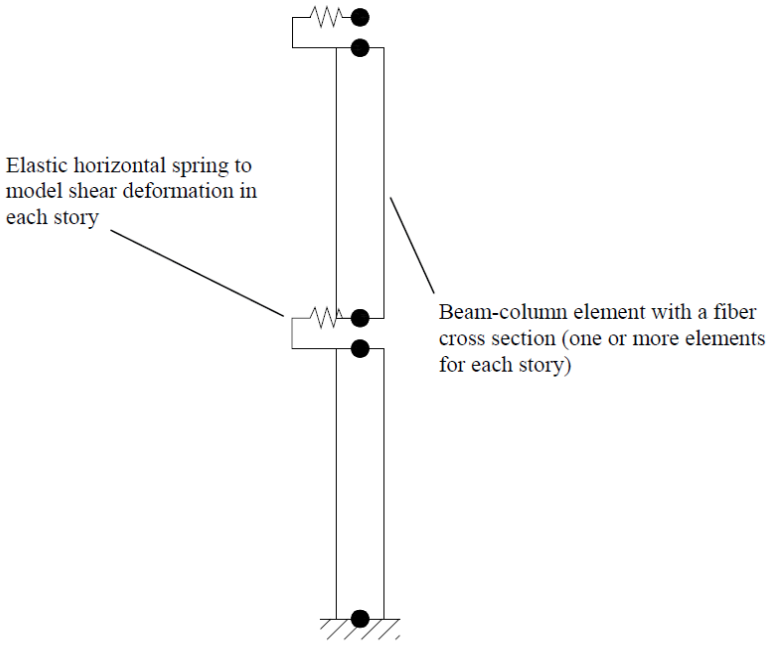

Figure 2.2: Beam Model with Shear Deformations included. Koutromanos, I., and B. Shing. 2010. "Trial Application: Reinforced Masonry Shear Wall Structures." In Evaluation of the FEMA P-695 Methodology for Quantification of Building Seismic Performance Factors. *National Institute of Standards and Technology, USA*. Used under fair use, 2014.

A beam model with a fiber element approach was used by Koutromanos and Shing (2010) to analyze reinforced masonry (fully-grouted) shear walls subjected to seismic loads. In their approach, shear walls were discretized into fiber layers of material, which consisted of either masonry or steel. The uniaxial material model for the steel reinforcement incorporated rupture and buckling. This beam model used horizontal elastic springs at each story to account for shear deformations as seen in Figure 2.2. The representation of shear deformations using elastic springs is an oversimplification of nonlinear behavior, especially for shear-dominated walls.

In summary, beam models predict flexure-dominated reinforced concrete/masonry shear wall behavior with good accuracy, but current techniques lack formulations that replicate the behavior of shear-dominated walls.

2.2: Truss Models

In the truss model approach, the shear wall is idealized as a two-dimensional assemblage of horizontal, vertical, and diagonal truss elements, as shown in Figure 2.3. Horizontal and vertical truss elements represent the longitudinal and transverse steel reinforcement along with surrounding concrete while diagonal elements account for the diagonal compression field. Each truss element is assigned its respective area and constitutive laws.

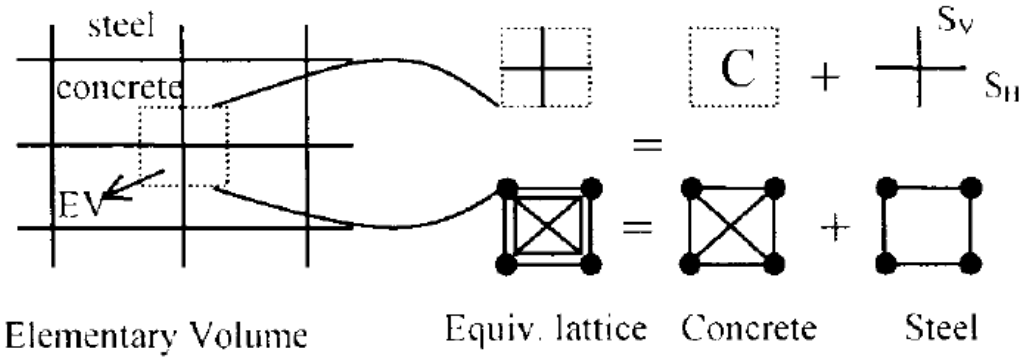

Figure 2.3: Equivalent Reinforced Concrete Truss Model. Mazars, J., Kotronis, P., and Davenne, L. (2002), "A New Modelling Strategy for the Behaviour of Shear Walls under Dynamic Loading." Earthquake Engineering & Structural Dynamics 31 (4): 937–54. Used under fair use, 2014.

Vallenas et al. (1979) used truss models to analyze the nonlinear behavior of reinforced concrete shear walls. In this truss analogy, each floor was modeled with one diagonal compression truss to account for the concrete diagonal compression field. Diagonal tension truss elements were not included. Horizontal trusses modeled the transverse steel reinforcements, which were lumped at slab levels.

Mazars et al. (2002) and Panagiotou et al. (2012) formulated truss models to simulate reinforced concrete shear walls subjected to static and dynamic loading. Unlike Vallenas et al. (1979), Mazars et al. (2002) and Panagiotou et al. (2012) used an assemblage of horizontal, vertical and diagonal elements between the stories of a building as shown in Figure 2.4. In these

models, the diagonal trusses represented concrete only, and the horizontal and vertical trusses represented reinforcing steel bars with their surrounding concrete.

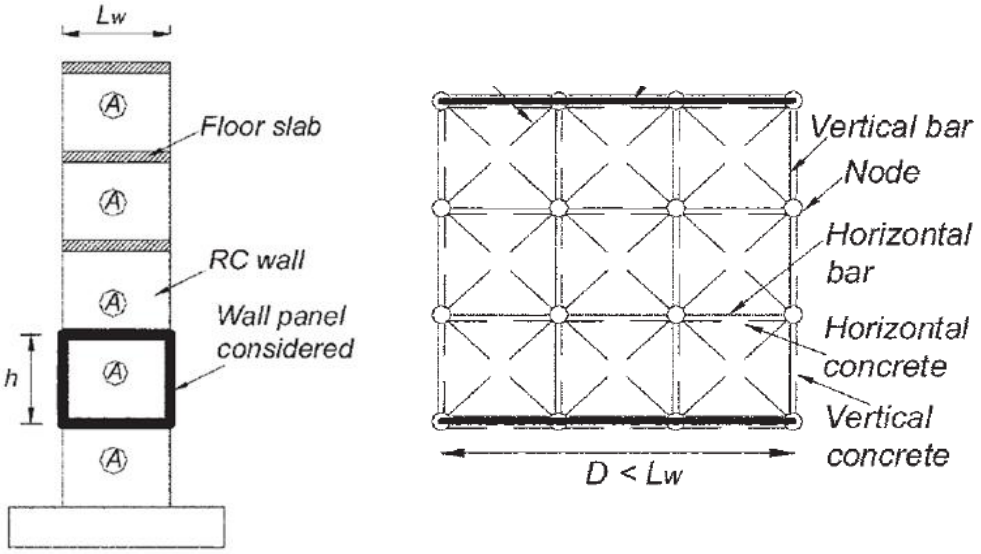

Figure 2.4: Reinforced Concrete Wall Truss Model. Panagiotou, M., Restrepo, J., Schoettler, M., and Kim, G. (2012), "Nonlinear Cyclic Truss Model for Reinforced Concrete Walls." ACI Structural Journal: 205–214. Used under fair use, 2014.

The Panagiotou et al. (2012) truss model also incorporated the effect of transverse strains on the diagonal compressive field, which is shown, based on empirical data, to reduce the peak compressive strength of cracked concrete. This effect was implemented by using diagonal zero-stiffness tensile strain gauges and compression struts as shown in Figure 2.5a. Figure 2.5b shows how the peak compressive strength reduces with the increase of transverse tensile strains. In addition, Panagiotou et al. utilized the concrete fracture energy concept to account for the mesh size effect. More details on the mesh size effect can be found in Chapter 3.

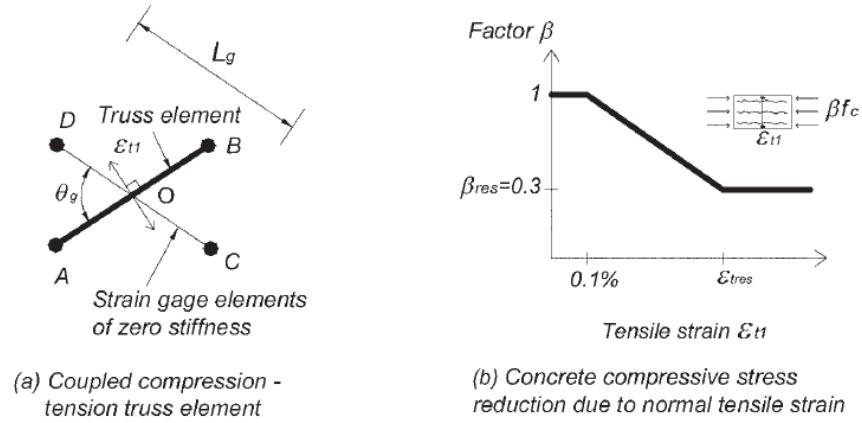

Figure 2.5: Model used to reduce Peak Compressive Strength due to the Presence of Transverse, Tensile Strain. Panagiotou, M., Restrepo, J., Schoettler, M., and Kim, G. (2012), "Nonlinear Cyclic Truss Model for Reinforced Concrete Walls." ACI Structural Journal: 205–214. Used under fair use, 2014.

Truss models provide a more sophisticated method to analyze reinforced concrete/masonry shear walls than beam models, but have certain limitations. The accuracy of a truss model is highly dependent on the angle of the diagonal compression struts (Mazars et al. 2002). Further, truss models do not account for out-of-plane loading and thus cannot adequately model the slab-wall interaction in three-dimensional building systems.

2.3: Finite Element Models

Finite element models provide another method of analyzing nonlinear reinforced concrete/masonry shear wall structures. In these models, a physical space is discretized into a mesh of finite elements as shown in Figure 2.6. This technique utilizes material constitutive laws and assumes a deformation pattern using approximate shape functions. Solutions are then obtained using the displacements/forces at discrete locations along a finite element known as nodes. If a sufficiently small mesh size is utilized along with an appropriate deformation pattern

(shape functions) and constitutive material models, the finite element model yields representative results.

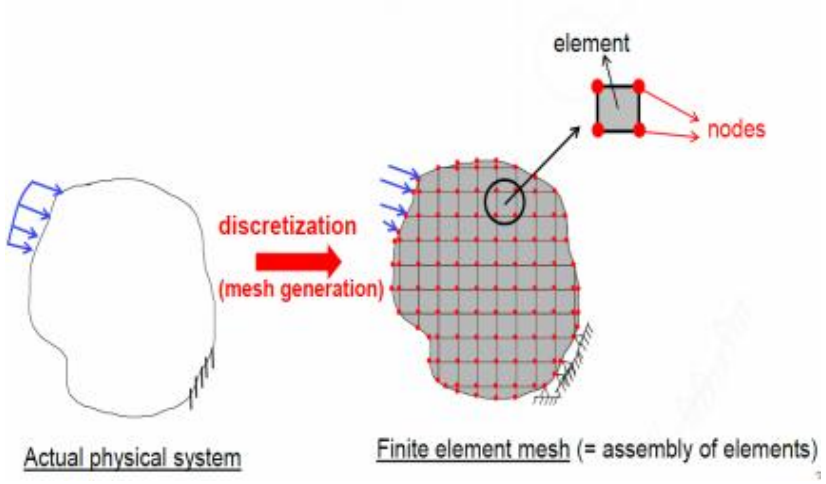

Figure 2.6: Finite Element Discretization (Koutromanos 2013)

The finite element analysis of reinforced concrete/masonry walls is based on the use of two-dimensional plane stress, shell, or three-dimensional solid elements. The elements use appropriate material models to describe the nonlinear behavior of concrete and masonry.

One of the material models employed in many finite element models is the smeared-crack model. The smeared-crack approach smears or averages the effects of cracks over a nonzero crack-band length, which for constant strain conditions equals the element length. Concrete/fully-grouted masonry is assumed to behave isotropically before fracture and orthotropically after fracture. Typically, two orthogonal cracks may form at each gauss point of the elements. The first crack forms when the maximum principal stress exceeds the tensile cutoff criterion and is oriented perpendicular to the maximum principal stress direction. Similarly, the second crack forms when the orthogonal stress exceeds the tensile cutoff criterion. Reinforcing steel can also be smeared into the element and is assumed to have only uniaxial strength in the specified orientation.

Smeared-crack models are divided into two different types: rotating smeared-crack model and fixed smeared-crack model. The rotating smeared-crack model rotates the cracks following the orientation of the orthogonal principal strain coordinate axes. The fixed smeared-crack model fixes the axes of orthotropy (crack normal and crack parallel) as well as the orientation of the crack after a crack has formed. The rotating-crack approach can provide adequate results for localized cracks at arbitrary loadings, but it is not suitable for cyclic loading scenarios (Kim et al. 2002).

Another material model utilized by finite element analyses is the damage-plasticity model for concrete/masonry. This model, originally developed by Lubliner et al. (1989) and enhanced by Lee and Fenves (1998) for the analysis of reinforced concrete structures subjected to cyclic loading, can be implemented in the commercial program ABAQUS (Simulia 2006). The damage-plasticity model assumes all inelastic strain, including strain from cracking, can be modeled using an isotropic plasticity model and uses damage variables to account for tensile damage (e.g. cracking) and compressive damage (e.g. crushing).

2.3.1: Two-dimensional Plane Stress Elements

Two-dimensional plane stress elements have two translational degrees of freedom (DOFs) at each node and can only develop in-plane resistance. Figure 2.7 represents a 4-node quadrilateral plane stress element with the associated DOFs at each node. Two-dimensional plane stress elements are often used to model and analyze reinforced concrete/masonry shear walls or panels/slabs subjected to only in-plane loads.

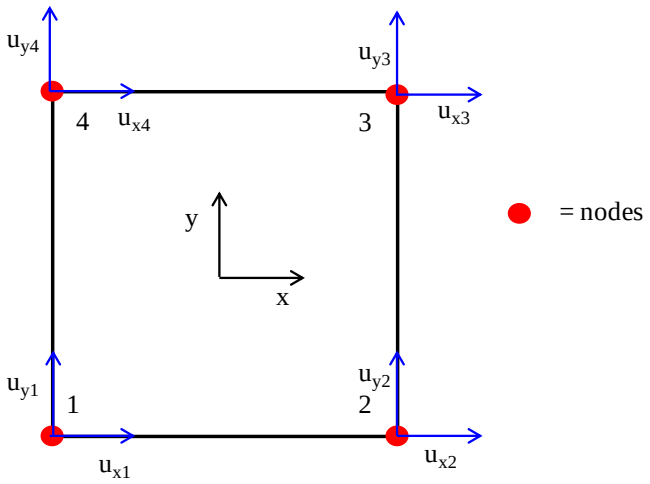

Figure 2.7: Four-node Quadrilateral Plane Stress Element

Vecchio (1989) utilized two-dimensional plane stress quadrilateral and triangular elements with a rotating smeared-crack approach for the analysis of reinforced concrete structures. The Vecchio (1989) element accounted for material nonlinearities by incorporating the Modified Compression Field Theory developed by Vecchio and Collins (1986). This method first introduces a new material stiffness matrix using the secant moduli in orthogonal directions for each material. An iterative scheme is then utilized until the proposed stiffness matrix converges to the element material matrix found using compatibility. The Vecchio (1989) model reduced the peak compressive strength of cracked concrete subjected to biaxial stresses. It also captured the tension stiffening effect in concrete by making the tensile softening of concrete shallower. The analytical model proposed by Vecchio (1989) was able to reproduce the nonlinear load-deformation response of panels, deep beams, and wall structures subjected to static monotonic loading. Chang et al. (1987) described a similar element that incorporated shear transferring through aggregate interlock and dowel actions across cracked concrete sections by reducing the shear stiffness. The Chang et al. (1987) model predicted well the shear stress-strain behavior of four reinforced concrete panels subjected to only static monotonic loading.

Lofti and Shing (1991) used a plane stress element that utilizes the fixed smeared-crack approach or the rotating smeared-crack approach for the analysis of fully-grouted reinforced masonry shear walls. The primary goal of their research was to capture strength and failure mechanisms of both flexure-dominated and shear-dominated reinforced masonry wall panels. The smeared-crack model was able to represent flexure-dominated behavior but was not able to capture shear-dominated behavior of the wall panel specimens. It was concluded that smeared-crack continuum elements provide a weak representation of displacement discontinuities since cracks are smeared over a nonzero crack-band length leading to an overestimation of strength when large shear cracks form.

Lee and Fenves (1998) proposed the aforementioned damage-plasticity model for the analysis of reinforced concrete structures subjected to cyclic and monotonic loading. The model accounted for cyclic loading by defining separate damage variables for tension and compression. It also incorporated the degradation of stiffness due to damage as well as its recovery during crack opening and closing. The damage-plasticity model was implemented in a quadrilateral plane stress element and validated against experimental results from reinforced concrete structures subjected to uniaxial or biaxial (cyclic and monotonic) loading.

Ile and Reynouard (2000) utilized a four-node quadrilateral plane stress element with a fixed smeared-crack approach to analyze reinforced concrete shear wall structures. The model was initially used to reproduce the load-deformation response and damage patterns of isolated reinforced concrete shear walls subjected to in-plane quasi-static (cyclic and monotonic) loading. The analytical model was then extended to analyze a one-story reinforced concrete shear wall structure (Figure 2.8) with top and bottom slabs subjected to dynamic loading. The top slab and the additional masses that were added to the actual structure were modeled using perfectly elastic

elements. Analytical results from this model were in good agreement with the dynamic hysteretic response of the one-story experimental reinforced concrete shear wall.

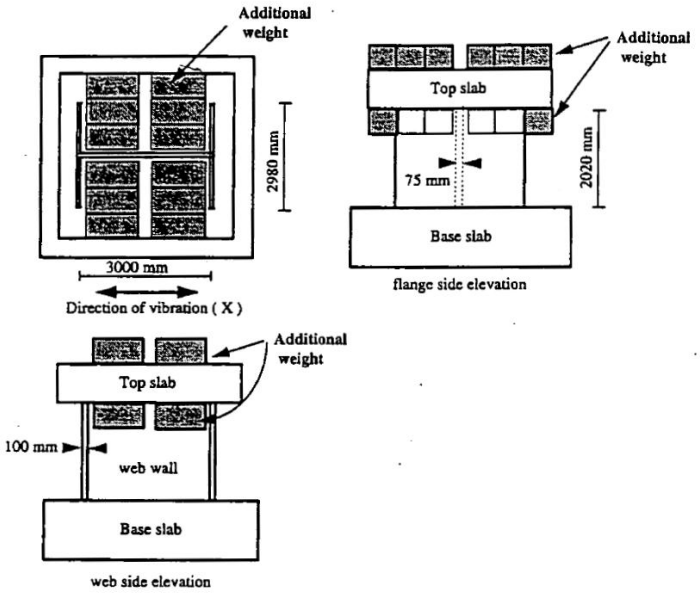

Figure 2.8: Reinforce Concrete Shear Wall Structure. Ile, N., and Reynouard, J. (2000), "Nonlinear Analysis of Reinforced Concrete Shear Wall under Earthquake Loading." *Journal of Earthquake Engineering* 4 (2): 183–213. Used under fair use, 2014.

Two-dimensional plane stress elements can be utilized to simulate shear walls/panels where primarily in-plane behavior is needed. However, two-dimensional plane stress elements do not account for out-of-plane loading caused by shear wall interactions with other structural elements.

2.3.2: Shell Elements

Shell elements resist both in-plane and out-of-plane loading and thus represent a more comprehensive alternative to two-dimensional plane stress elements. Each node of a shell element has five DOFs, which consist of three displacements (all three dimensions) and the two in-plane rotations. Shell elements can also include a small stiffness for the drilling DOF or the rotation normal to the face of the element, which allows for an easy connection between the shell

element and other finite elements such as three-dimensional beam-column elements (Kim et al. 2002). If the small stiffness is not included for the drilling DOF, issues with connectivity and the solution of the global stiffness equations may arise when the shell element is used in a three-dimensional mesh. Figure 2.9 shows the internal loadings of a shell element.

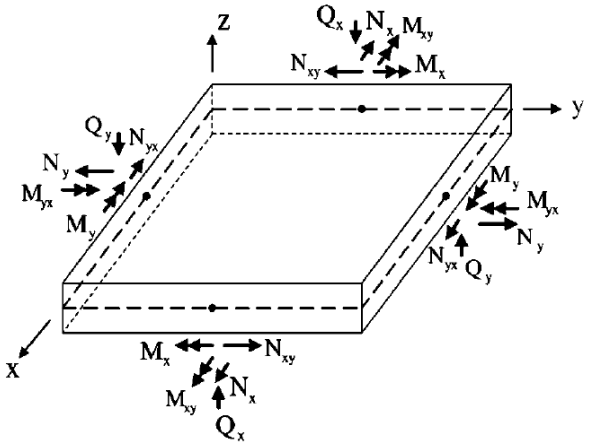

Figure 2.9: Internal Loadings in a Shell Element. Kim, T.-H., Lee, K.-M., and Shin, H.M. (2002), "Nonlinear Analysis of Reinforced Concrete Shells Using Layered Elements with Drilling Degree of Freedom." ACI Structural Journal 99 (4). Used under fair use, 2014.

The two types of shell elements are categorized into Reissner-Mindlin and Discrete Kirchhoff shell elements. The kinematics and formulations of these shell elements are described in more detail in Chapter 3.

2.3.2.i: Reissner-Mindlin Shell Elements

Reissner-Mindlin shell elements use an extension of the Timoshenko beam theory to shells in which out-of-plane shear deformations are considered and the through thickness shear stress distribution is assumed to be constant.

Polak and Vecchio (1993) and Hu and Schnobrich (1991) utilized 9-node heterosis shell elements with the layered sectional formulation and the rotating smeared-crack approach for the

analysis of reinforced concrete structures. The layered approach can easily account for nonlinear material property variation through the thickness of the element without resorting to a complete three-dimensional finite element (Hu and Schnobrich 1991). Each layer is assumed to be in a two-dimensional plane stress state and is assigned concrete, masonry, or steel material properties as shown in Figure 2.10. Once the stresses are determined in each layer, the stress resultants are found by numerically integrating through the thickness of the element. Both of these models were able to simulate the nonlinear load-deformation response of the experimental results.

Massicotte et al. (1990) detailed a 16-node Lagrangian shell element (Figure 2.11). The element incorporated the fixed and rotating smeared-crack approach with the layered formulation, and implemented a large strain, large displacement formulation to account for geometric nonlinearities in reinforced concrete structures.

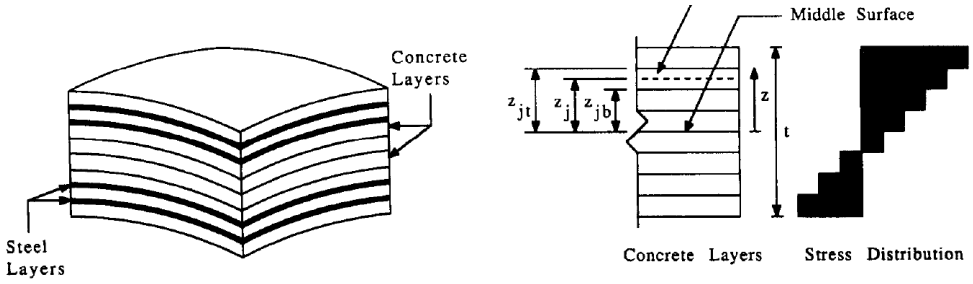

Figure 2.10: Layered Shell Element and Stress Distribution. Hu, H.-T., and Schnobrich, W.C. (1991), "Nonlinear Finite Element Analysis of Reinforced Concrete Plates and Shells Under Monotonic Loading." Computers & Structures 38 (5): 637–651. Used under fair use, 2014.

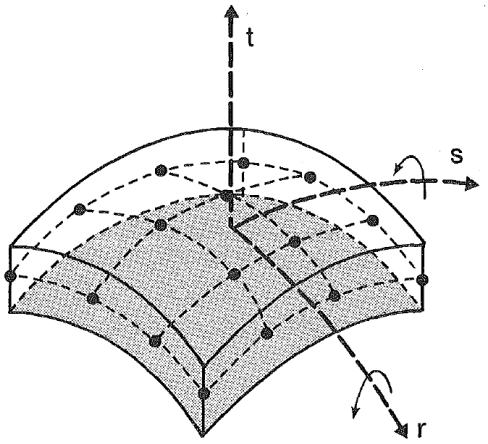

Figure 2.11: 16-node Lagrangian Shell Element. Massicotte, B., MacGregor, J., and Elwi, A. (1990), "Behavior of Concrete Panels Subjected to Axial and Lateral Loads." Journal of Structural Engineering 116 (9): 2324–2343. Used under fair use, 2014.

Liu and Teng (2008) developed a 9-node heterosis shell element using a non-layered/stress resultant formulation. With this approach, the in-plane stress distributions in the concrete were assumed based on a defined stress-strain relationship and linear strain distribution through the thickness. The stress-strain relationships for concrete and steel were the Hognestad's model and an elasto-plastic model with linear strain hardening respectively. The Liu and Teng (2008) model was able to analyze simple reinforced concrete slabs/panels subjected to in-plane and out-of-plane loading, but lacked verification against reinforced concrete wall-slab building systems.

2.3.2.ii: Discrete Kirchhoff Shell Elements

The Kirchhoff-Love shell theory is an extension of the Euler-Bernoulli beam theory to shells. The main difference between Kirchhoff-Love and Reissner-Mindlin is that the Kirchhoff-Love shell theory neglects out-of-plane shear deformations/strains limiting its applicability to

relatively thin shell-type structures. Further details regarding the kinematics and formulations of Discrete Kirchhoff shell elements can be found in Chapter 3.

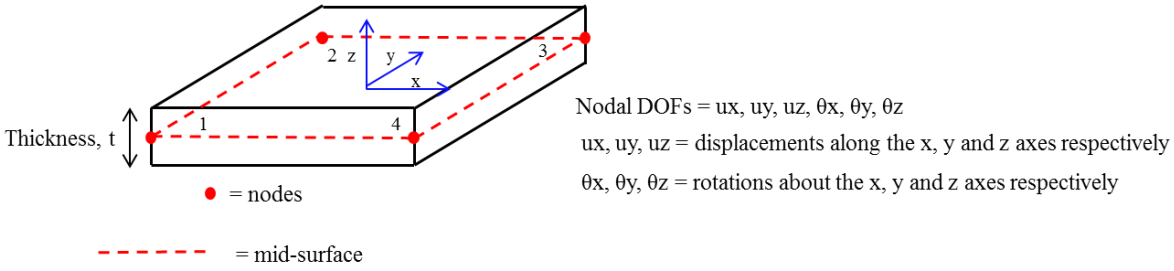

Figure 2.12: Four-node Quadrilateral Shell Element with Drilling DOF

Ile and Reynouard (2000) outlined a two-dimensional plane stress nonlinear material model that was utilized in a Discrete Kirchhoff triangular shell element. This model used a fixed smeared-crack approach with an Ottosen criterion. The Ottosen failure surface has an advantage of being continuous and convex at any point (Ile and Reynouard 2000). Discrete Kirchhoff triangular shell elements were used to model the web and flange walls of the single-story reinforced concrete shear wall, as shown in Figure 2.8, while three-dimensional elastic solid elements were used to analyze the top slab and additional masses. The analytical model reproduced the shear-dominated failure pattern and the hysteretic nonlinear load-displacement response of the test specimen subjected to dynamic loading. However, the location of the damage was not properly captured.

Kim et al. (2002) improved an existing four-node Discrete Kirchhoff quadrilateral flat shell element to incorporate drilling degrees of freedom as shown in Figure 2.12. This shell element was formulated using (1) a two-dimensional plane stress element with drilling degrees of freedom to represent the membrane behavior, and (2) a Discrete Kirchhoff plate element to capture the bending behavior. The element was able to reproduce the nonlinear load-deformation

response of reinforced concrete panels, shells, and beams subjected to static (cyclic and monotonic) in-plane and out-of-plane loading.

Discrete Kirchhoff shell elements can analyze relatively thin reinforced concrete/masonry structures subjected to in-plane and out-of-plane loading. Reinforced concrete/masonry walls and slabs/panels are often relatively thin and therefore it is adequate to neglect out-of-plane shear deformations.

2.3.3: Three-Dimensional Solid Elements

Three-dimensional solid elements can also be used to analyze reinforced concrete/masonry shear wall structures. In these models, three translational DOFs are assigned to each node of the element.

Cervera et al. (1987) used a 20-node isoparametric three-dimensional solid element, shown in Figure 2.13, to study reinforced concrete panels, deep beams, slabs, and slab-column connections. The model successfully captured the nonlinear load-deformation response as well as flexure-dominated and shear-dominated damage patterns of the experimental specimens subjected to static monotonic loading. The reinforced concrete panels used to validate the Cervera et al. simulations were tested by Vecchio and Collins (1982). It is worth noting that these results were previously reproduced by Chang et al. (1987) using a two-dimensional plane stress element.

Although three-dimensional solid elements can predict the behavior of reinforced concrete structures, they are often not practical and computationally inefficient which hinders their applicability to multi-story complex reinforced concrete/masonry shear wall structures.

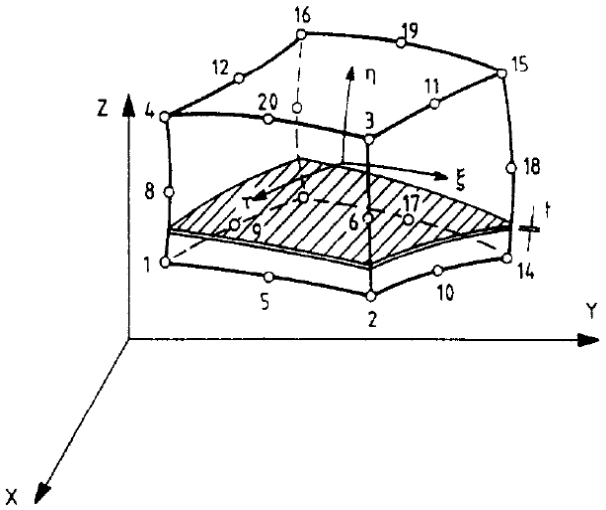

Figure 2.13: Twenty-Node Three-Dimensional Isoparametric Solid Element. Cervera, M., Hinton, E., and Hassan, O. (1987), "Nonlinear Analysis of Reinforced Concrete Plate and Shell Structures Using 20-noded Isoparametric Brick Elements." Computers & Structures 25 (6): 845–869. Used under fair use, 2014.

2.4: Conclusion

After reviewing the literature, nonlinear finite element analysis becomes an attractive option to model reinforced concrete/masonry shear wall structures. Nonlinear finite element analysis can be used to model many complex three-dimensional systems and loading conditions; and with the rapid advancements in computing power, it becomes an extremely viable option. Further, shell elements can model the in-plane and out-of-plane behavior exhibited in shear wall structures without resorting to using computationally intense three-dimensional solid elements.

Chapter 3: Analysis Methodology

Shell elements provide an accurate way of modeling reinforced concrete/masonry shear walls, slabs and three-dimensional wall-slab building systems. Shear walls and slabs need to resist/carry lateral loads (e.g. seismic or wind loading) as well as out-of-plane loads (e.g. gravity and bending loads). Since shell elements can resist in-plane and out-of-plane loading, they become an attractive way to model the complex three-dimensional behavior of reinforced concrete/masonry shear walls and slabs in wall-slab building systems.

The shell element discussed and evaluated in this thesis is an enhanced version of a flat, 4-node Discrete Kirchhoff quadrilateral (DKQ4) shell element. The enhanced element has been implemented in the program FEAP (Taylor 2007). The proposed shell element improves on the existing formulation of the DKQ4 element by introducing the corotational approach, a through-thickness Lobatto integration approach, and inelastic material models.

Figure 3.1 represents a three-dimensional view of a shell element with local coordinate axes. The four nodes are located at corners of the mid-surface, which is taken as the reference surface. Each node develops resistance along five Degrees of Freedom (DOF), namely displacements in three directions and the two rotations about the planar axis's of the shell. An option to include a small stiffness for the rotational degree of freedom (drilling degree of freedom) about the axis normal to the face of the shell element is also supported. The small stiffness can be included for the drilling DOF to prevent issues with connectivity and the solution of the global stiffness equations when the shell element is used in a three-dimensional mesh.

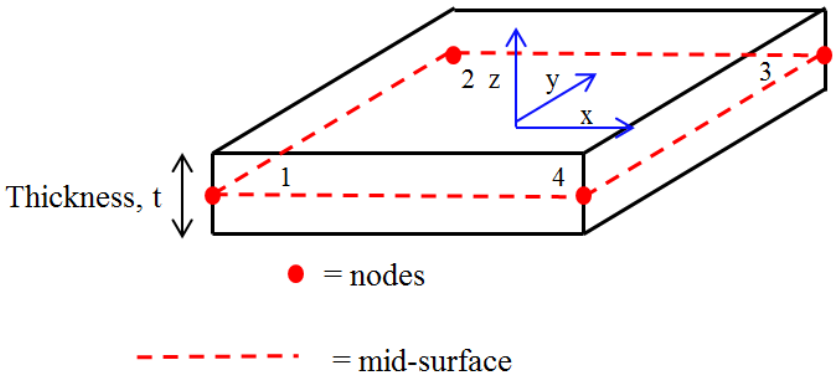

Figure 3.1: Shell Element

3.1: Shell Element Kinematics and Calculation of Stress Resultants and Nodal Forces/Moments

Two shell theories commonly used in shell element formulations are the Kirchhoff-Love and Reissner-Mindlin shell theories. The Kirchhoff-Love shell theory is an extension of the Euler-Bernoulli beam theory to shells. The Kirchhoff-Love shell theory utilizes the following kinematic assumptions.

1. Plane sections normal to the mid-surface remain plane and perpendicular to the mid-surface in the deformed configuration. This means out-of-plane shear deformations are neglected.
2. The stress perpendicular to the shell face is zero or negligible ($\sigma_{zz} = 0$).
3. The out-of-plane displacements are constant through the thickness of the shell element. Thus, the out-of-plane displacements can be taken with respect to the reference surface (mid-surface).

The Reissner-Mindlin shell theory is similar to the Kirchhoff-Love theory, except that plane sections normal to the mid-surface remain plane but not necessarily perpendicular to the mid-surface in the deformed configuration. Therefore, out-of-plane shear deformations are accounted for. The Reissner-Mindlin shell theory also assumes a constant shear stress through the thickness. A visualization of the Reissner-Mindlin assumptions is shown in Figure 3.2.

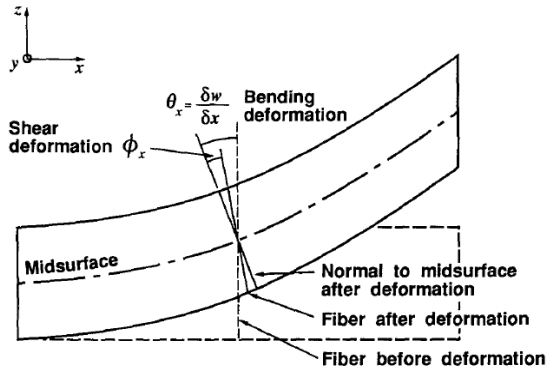

Figure 3.2: Visualization of Reissner-Mindlin Kinematic Assumptions. Polak, M., and Vecchio, F. (1993), "Nonlinear Analysis of Reinforced-Concrete Shells." Journal of Structural Engineering 119 (12): 3439–3462. Used under fair use, 2014.

Both of these shell theories have advantages and disadvantages. The Reissner-Mindlin theory only requires multi-dimensional shape functions that satisfy C^0 continuity for the out-of-plane displacements. Continuity specifies how smooth or continuous the trial solution and weight functions need to be to ensure convergence. In order to satisfy C^0 continuity, the displacements need to be continuous along interelement boundaries. Figure 3.3 details examples of one-dimensional continuity functions. Although the Reissner-Mindlin shell theory can be applied to thick and thin shells, poor convergence for thin plates/shells can occur because of the shear-locking phenomenon (Hughes 2000). This issue is commonly solved by utilizing a heterosis element with selective reduced integration. The heterosis element (Figure 3.4) has nine nodes and uses Lagrangian shape functions for the two rotational degrees of freedom about the in-plane

axes and serendipity shape functions for the three translational degrees of freedom. The middle node only has the two rotational degrees of freedom. Figure 3.5 shows examples of Lagrangian and serendipity quadrilateral elements. Selective reduced integration is then used to further solve the shear-locking phenomenon for the analysis of thin plates. This entails using a full integration rule for the bending and membrane portion of the stiffness matrix, while using a reduced integration rule for the out-of-plane shear contribution to the stiffness matrix.

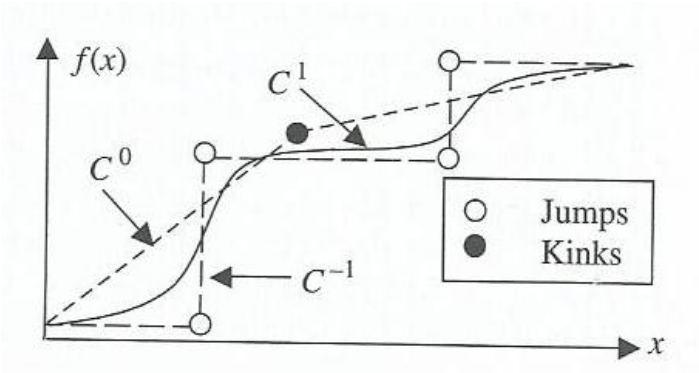

Figure 3.3: C^{-1}, C^{0}, and C^{1} Continuity Functions. Fish, J., and Belytschko, T. (2007), *A First Course in Finite Elements*. John Wiley and Sons. Used under fair use, 2014.

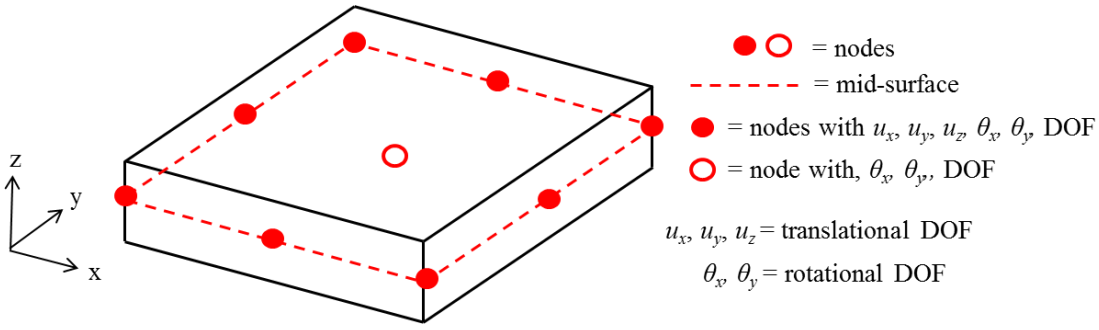

Figure 3.4: Heterosis Element

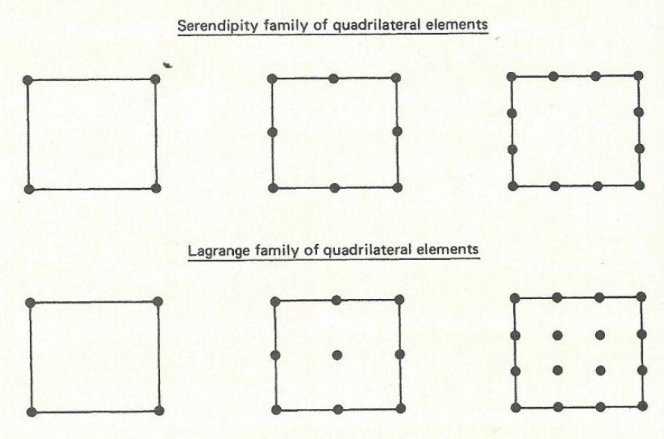

Figure 3.5: Lagrange and Serendipity Quadrilateral Elements. Hughes, T. 2000. *The Finite Element Method: Linear Static and Dynamic Finite Element Analysis*. Dover Publications, Inc. Used under fair use, 2014.

The Kirchhoff-Love shell theory requires shape functions that satisfy C^1 multidimensional continuity for the out-of-plane displacements. In order to satisfy this requirement, the out-of-plane displacements and its derivatives with respect to the planar axes need to be continuous along interelement boundaries. However, shape functions that satisfy multidimensional C^1 continuity are extremely hard to develop. Therefore, Discrete Kirchhoff elements (i.e. Discrete Kirchhoff Quadrilaterals and Discrete Kirchhoff Triangles) are used where the Kirchhoff-Love assumptions are satisfied at specified discrete points rather than the whole element domain. Since out-of-plane shear deformations are neglected, Discrete Kirchhoff elements can be used to simulate thin shells, but are not valid for thick shells (or non-thin shells).

The shell element discussed in this thesis uses a synthesis of a conventional 4-node quadrilateral plane stress element and a 4-node Discrete Kirchhoff plate element to model the in-plane (membrane) and out-of-plane (flexural) behavior respectively. The 4-node Discrete Kirchhoff shell element is of interest because it only has four nodes (improving computational efficiency compared to a heterosis shell element) and does not need adjustments to obtain

convergence for thin plates/shells. The element used to represent the in-plane (membrane) behavior of the shell element is the 4-node, two-dimensional isoparametric quadrilateral element (Q4) shown in Figure 3.6. Each node has two DOF (two in-plane displacements). This type of element utilizes two-dimensional mapping to go from the physical space to the parametric space allowing it to analyze irregular quadrilaterals in the physical space. The mapping can be seen in the following equations.

$$x(\xi,\eta) = \sum_{i=1}^{4} (N_i^{Q4}(\xi,\eta) \times x_i) \quad \text{and} \quad y(\xi,\eta) = \sum_{i=1}^{4} (N_i^{Q4}(\xi,\eta) \times y_i) \qquad \textbf{(1), (2)}$$

$$x_i, y_i = \text{ x and y coordinates in the physical space at node i}$$

$$N_i^{Q4}(\xi,\eta) = \text{ 4-node quadrilateral shape functions listed below}$$

The 2x2 Jacobian matrix, [J], is also needed for relating the derivatives of the physical coordinates with respect to the parametric coordinates for each element (Fish and Belytschko 2007). The Jacobian matrix, [J], and its inverse, $[J]^{-1}$, are needed for mapping and numerical integration (Gauss and Lobatto quadrature).

$$[J] = \begin{bmatrix} \frac{\partial x}{\partial \xi} & \frac{\partial y}{\partial \xi} \\ \frac{\partial x}{\partial \eta} & \frac{\partial y}{\partial \eta} \end{bmatrix} \qquad \textbf{(3)}$$

$$[J]^{-1} = \begin{bmatrix} \frac{\partial \xi}{\partial x} & \frac{\partial \eta}{\partial x} \\ \frac{\partial \xi}{\partial y} & \frac{\partial \eta}{\partial y} \end{bmatrix} \qquad \textbf{(4)}$$

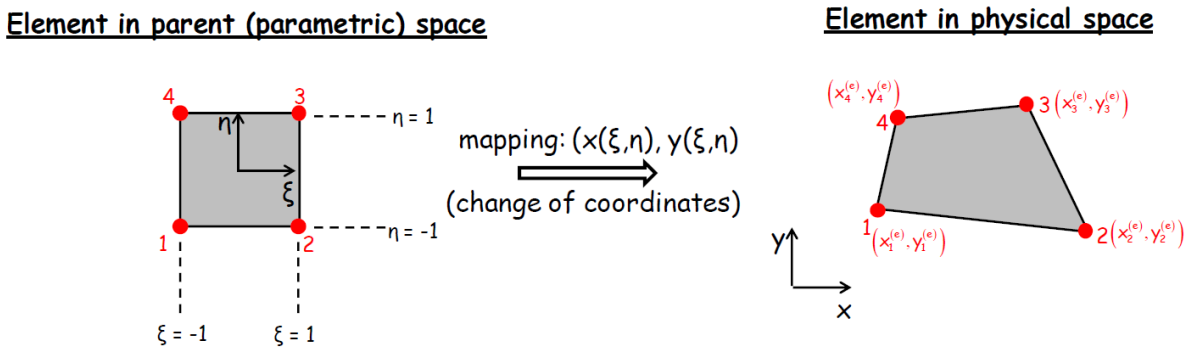

Figure 3.6: Four-node Isoparametric Quadrilateral Plane Stress Element (Koutromanos 2013)

The Q4 uses the following four shape functions to approximate the in-plane deformation pattern.

$$N_1^{Q4}(\xi,\eta) = \frac{1}{4} \times (1-\xi) \times (1-\eta) \quad \textbf{(5)}$$

$$N_2^{Q4}(\xi,\eta) = \frac{1}{4} \times (1+\xi) \times (1-\eta) \quad \textbf{(6)}$$

$$N_3^{Q4}(\xi,\eta) = \frac{1}{4} \times (1+\xi) \times (1+\eta) \quad \textbf{(7)}$$

$$N_4^{Q4}(\xi,\eta) = \frac{1}{4} \times (1-\xi) \times (1+\eta) \quad \textbf{(8)}$$

The in-plane deformation pattern for each element, $\{u^e_m(\xi,\eta)\}$, can be found by the following equation.

$$\{u_m^e(\xi,\eta)\} = \left[N^{Q4}(\xi,\eta)\right] \times \{U_m^e\} \quad \textbf{(9)}$$

where,

$$\left[N^{Q4}(\xi,\eta)\right] = \quad \textbf{(10)}$$

$$\begin{bmatrix} N_1^{Q4}(\xi,\eta) & 0 & N_2^{Q4}(\xi,\eta) & 0 & N_3^{Q4}(\xi,\eta) & 0 & N_4^{Q4}(\xi,\eta) & 0 \\ 0 & N_1^{Q4}(\xi,\eta) & 0 & N_2^{Q4}(\xi,\eta) & 0 & N_3^{Q4}(\xi,\eta) & 0 & N_4^{Q4}(\xi,\eta) \end{bmatrix}$$

and

$$\{U_m^e\} = \text{in-plane element nodal displacements vector} = \left\{u_{x1}^e \quad u_{y1}^e \quad u_{x2}^e \quad u_{y2}^e \quad u_{x3}^e \quad u_{y3}^e \quad u_{x4}^e \quad u_{y4}^e\right\}^T \tag{11}$$

Once the membrane nodal displacements are known, the membrane strains, $\{\varepsilon_m\}$, are calculated at the mid-surface of the shell element using the following equation. These membrane strains are useful in determining stresses from constitutive relationships.

$$\{\varepsilon_m\} = \left[B^{Q4}\right] \times \{U_m^e\} \tag{12}$$

where,

$$\{\varepsilon_m\} = \begin{Bmatrix} \varepsilon_{mx} \\ \varepsilon_{my} \\ \varepsilon_{mxy} \end{Bmatrix} \tag{13}$$

$\varepsilon_{mx}, \varepsilon_{my} =$ in-plane normal strains; $\varepsilon_{mxy} =$ in-plane shear strain

$$\left[B^{Q4}\right] = \begin{bmatrix} \frac{\partial N_1^{Q4}}{\partial x} & 0 & \frac{\partial N_2^{Q4}}{\partial x} & 0 & \frac{\partial N_3^{Q4}}{\partial x} & 0 & \frac{\partial N_4^{Q4}}{\partial x} & 0 \\ 0 & \frac{\partial N_1^{Q4}}{\partial y} & 0 & \frac{\partial N_2^{Q4}}{\partial y} & 0 & \frac{\partial N_3^{Q4}}{\partial y} & 0 & \frac{\partial N_4^{Q4}}{\partial y} \\ \frac{\partial N_1^{Q4}}{\partial y} & \frac{\partial N_1^{Q4}}{\partial x} & \frac{\partial N_2^{Q4}}{\partial y} & \frac{\partial N_2^{Q4}}{\partial x} & \frac{\partial N_3^{Q4}}{\partial y} & \frac{\partial N_3^{Q4}}{\partial x} & \frac{\partial N_4^{Q4}}{\partial y} & \frac{\partial N_4^{Q4}}{\partial x} \end{bmatrix} \tag{14}$$

and,

$$\frac{\partial N_i^{Q4}(\xi,\eta)}{\partial x} = \frac{\partial N_i^{Q4}(\xi,\eta)}{\partial \xi} \times \frac{\partial \xi}{\partial x} + \frac{\partial N_i^{Q4}(\xi,\eta)}{\partial \eta} \times \frac{\partial \eta}{\partial x} \tag{15}$$

$$\frac{\partial N_i^{Q4}(\xi,\eta)}{\partial y} = \frac{\partial N_i^{Q4}(\xi,\eta)}{\partial \xi} \times \frac{\partial \xi}{\partial y} + \frac{\partial N_i^{Q4}(\xi,\eta)}{\partial \eta} \times \frac{\partial \eta}{\partial y} \tag{16}$$

$\frac{\partial \xi}{\partial x}, \frac{\partial \xi}{\partial y}, \frac{\partial \eta}{\partial x}$ and $\frac{\partial \eta}{\partial y}$ can be found from the inverse of the Jacobian array, [J].

The plate bending and displacement behavior of the shell element is accounted for using the plate element developed by Batoz and Tahar (1982). As stated previously, the Discrete Kirchhoff approach satisfies the Kirchhoff-Love assumptions (shear deformations are neglected) at discrete points. The proposed shell element satisfies the Kirchhoff-Love assumptions along the boundaries of the element, which introduces the need to have intermediate calculation nodes at the mid-spans of each element side raising the total number of nodes to eight.

Batoz and Tahar (1982) base the formulation of the four-node Discrete Kirchhoff quadrilateral element on the discretization of strain energy in which only flexural strain energy, U_b^e, is included (transverse shear strain energy is neglected). In this formulation, the flexural strain energy is a function of the generalized strain vector (bending curvatures) and the flexural stress resultant vector (moments per unit width) shown below.

$$\{\varepsilon_f\} = \text{ curvatures from bending} =$$

$$\begin{Bmatrix} \varphi_x \\ \varphi_y \\ \varphi_{xy} \end{Bmatrix} = \begin{Bmatrix} \frac{\partial \theta_x}{\partial x} \\ \frac{\partial \theta_y}{\partial y} \\ \frac{\partial \theta_x}{\partial y} + \frac{\partial \theta_y}{\partial x} \end{Bmatrix} \quad \textbf{(17)}$$

$$\{\sigma_f^{res}\} = \text{ 3x1 flexural stress resultant vector (moments per unit width)} =$$

$$\begin{Bmatrix} M_{xx} \\ M_{yy} \\ M_{xy} \end{Bmatrix} \quad \textbf{(18)}$$

Where, θ_x and θ_y are the rotations normal to the undeformed mid-surface in the x-z and y-z planes respectively.

It is then convenient to note that the element strain energy due to bending, U_b^e, depends only on the rotations normal to the undeformed mid-surface. These rotations only require C^0 multidimensional shape functions, which are readily available. θ_x and θ_y are then defined by incomplete cubic polynomial expressions utilizing the isoparametric shape functions of the 8-node serendipity element. It is important to note there are four corner nodes and four intermediate mid-nodes (for formulation purposes).

$$\theta_x = \sum_{i=1}^{8} N(\xi,\eta)_i \times \boldsymbol{\theta}_{xi} \qquad \theta_y = \sum_{i=1}^{8} N(\xi,\eta)_i \times \boldsymbol{\theta}_{yi} \qquad \textbf{(19), (20)}$$

$$\boldsymbol{\theta}_{xi}, \boldsymbol{\theta}_{yi} = \text{nodal rotations at corner nodes and mid-nodes}$$

8-node Serendipity Shape Functions:

$$N(\xi,\eta)_1 = -\frac{1}{4} \times (1-\xi) \times (1-\eta) \times (1+\xi+\eta) \qquad \textbf{(21)}$$

$$N(\xi,\eta)_2 = \frac{1}{2} \times (1-\xi) \times (1+\xi) \times (1-\eta) \qquad \textbf{(22)}$$

$$N(\xi,\eta)_3 = -\frac{1}{4} \times (1+\xi) \times (1-\eta) \times (1-\xi+\eta) \qquad \textbf{(23)}$$

$$N(\xi,\eta)_4 = \frac{1}{2} \times (1+\xi) \times (1+\eta) \times (1-\eta) \qquad \textbf{(24)}$$

$$N(\xi,\eta)_5 = -\frac{1}{4} \times (1+\xi) \times (1+\eta) \times (1-\xi-\eta) \qquad \textbf{(25)}$$

$$N(\xi,\eta)_6 = \frac{1}{2} \times (1-\xi) \times (1+\xi) \times (1+\eta) \qquad \textbf{(26)}$$

$$N(\xi,\eta)_7 = -\frac{1}{4} \times (1-\xi) \times (1+\eta) \times (1+\xi-\eta) \qquad \textbf{(27)}$$

$$N(\xi,\eta)_8 = \frac{1}{2} \times (1-\xi) \times (1+\eta) \times (1-\eta) \qquad \textbf{(28)}$$

Figure 3.7 provides a detailed version of a general DKQ4 and pertinent geometric parameters and coordinate systems that are used in the derivation of the plate element. The Kirchhoff-Love

assumptions (shear deformations are neglected) are implemented at the corner and middle nodes as described below.

1. Corner nodes:

$$\theta_{xi} + \frac{\partial w_i}{\partial x} = 0 \quad \theta_{yi} + \frac{\partial w_i}{\partial y} = 0 \quad i = 1, 2, 3, 4 \text{ (i.e. shear strains=0)} \qquad \textbf{(29), (30)}$$

2. Mid-nodes:

$$\theta_{sk} + \frac{\partial w_k}{\partial s} = 0 \qquad k = 5, 6, 7, 8 \text{ (i.e. shear strains=0)} \qquad \textbf{(31)}$$

$s =$ direction along the boundary of the element as seen in Figure 3.7

$w =$ Transverse (Out-of-plane) Displacement

$\theta_{sk} =$ Rotation at mid-node k about the s-axis as seen in Figure 3.7

The direction along the element boundary corresponds to the s-axis and the direction perpendicular to the element boundary corresponds to n.

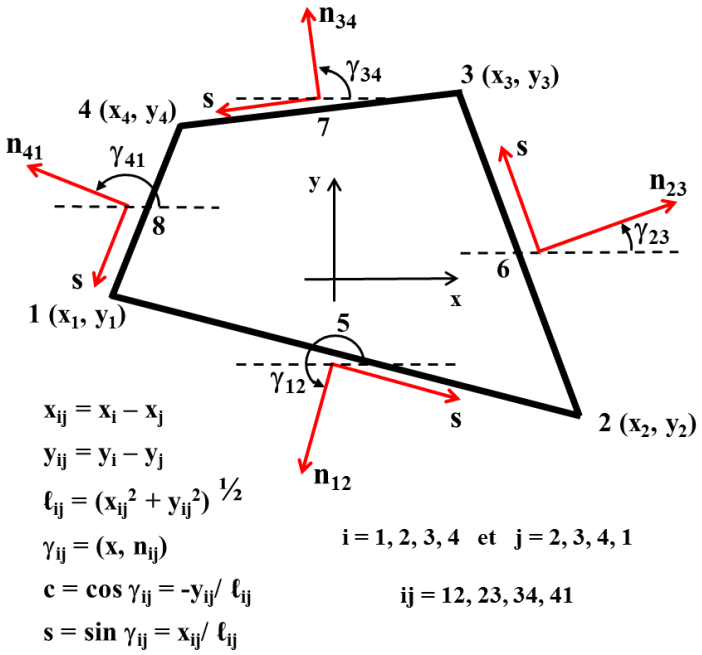

Figure 3.7: Geometry of a General DKQ4. Batoz, J.-L., and Tahar, B. 1982, "Evaluation of a New Quadrilateral Thin Plate Bending Element." ***International Journal for Numerical Methods in Engineering*** **18 (11): 1655–77. Used under fair use, 2014.**

The transverse displacement field, w, is defined along the element's boundary and is calculated using cubic Hermite polynomial interpolation functions. Cubic Hermite polynomial shape functions are also used in Euler-Bernoulli beam elements and can satisfy one-dimensional C^1 continuity. Since these shape functions are only used along the boundaries (one-dimensional space) for the transverse displacement field, the C^1 continuity requirement for the Kirchhoff-Love shell theory is satisfied at these locations. The derivative of the transverse displacement deformation pattern with respect to the s-axis at each mid-node yields the rotations along the entire element boundary.

$$\frac{\partial w_k}{\partial s} = \frac{-3}{2 \times l_{ij}} \times (w_i - w_j) - \frac{1}{4} \times \left(\frac{\partial w_i}{\partial s} - \frac{\partial w_j}{\partial s} \right) \quad \textbf{(32)}$$

k = 5, 6, 7, 8; ij = sides 12, 23, 34, 41; l_{ij} = Length of side ij

The rotation about the n-axis is then found to vary linearly along each of the element sides.

$$\theta_{nk} = \frac{1}{2} \times (\theta_{ni} - \theta_{nj}) = -\frac{1}{2} \times (\frac{\partial w_i}{\partial n} - \frac{\partial w_j}{\partial n}) \quad \textbf{(33)}$$

k = 5, 6, 7, 8 mid-nodes of sides ij = 12, 23, 34, 41

θ_{nk} = Rotation at midnode k about the n-axis as seen in Figure 3.7

The transverse displacements and rotations are now defined along the entire boundary of the element. It is important to note these displacements are only defined along the boundary (not the interior) and vary independently along the sides. Because the derivative of the transverse displacement and the rotation with respect to the s-axis are of the same quadratic expressions, the Kirchhoff-Love assumptions are satisfied along the entire boundary of the DKQ4. The DKQ4 will converge to thin plate theory but is not applicable for the analysis of thick plates/shells (Batoz and Tahar 1982). The rotations and displacements are compatible along the entire boundary of the DKQ4.

An expression can then be written to find the curvatures from the nodal displacement/rotation vector.

$$\{\varepsilon_f\} = \begin{Bmatrix} \phi_x \\ \phi_y \\ \phi_{xy} \end{Bmatrix} = [B_f] \times \{U_f\} \quad \textbf{(34)}$$

$$\{U_f\} = \{w_1 \quad \theta_{x1} \quad \theta_{y1} \quad w_2 \quad \theta_{x2} \quad \theta_{y2} \quad w_3 \quad \theta_{x3} \quad \theta_{y3} \quad w_4 \quad \theta_{x4} \quad \theta_{y4}\}^T \quad \textbf{(35)}$$

$\{U_f\}$ = nodal displacement/rotation vector

$[B_f]$ is a 3x12 matrix whose components are combinations of 8-node serendipity element shape functions and their derivatives with respect to x, y, ξ and η. The expressions giving the components of $[B_f]$ are provided in Batoz and Tahar (1982).

3.1.1: Corotational Approach: Accounting for Geometric Nonlinearities

Reinforced concrete/masonry structures subjected to extreme loading (e.g. seismic) can often incur large displacements because of significant inelastic damage (or near collapse/ultimate failure). The assumption made for linear analysis that the change in geometry due to the displacements is negligible may no longer be valid. The nonlinearity in behavior due to large displacements is referred to as geometric nonlinearity.

An efficient way to account for geometric nonlinearities for reinforced concrete/masonry structural engineering systems/elements is to utilize the corotational approach, which is a formulation of large displacement/small strain theory. The large displacement/small strain theory is computationally efficient as it allows the use of a linear displacement-strain relationship, which simplifies the relation between stresses and nodal forces. Also, since stresses and strains are found in the local coordinate system of the deformed configuration, the relationship between stresses and strains is independent of rigid body motion (Belytschko and Hsieh 1973). This means the effects of stress-rates and/or strain-rates can be incorporated (Belytschko and Hsieh 1973). During extreme cyclic loading applications (e.g. certain seismic events), steel loses the majority of its strength at strains of approximately 5% while concrete loses all of its resistance at strains much less than 5%. This means reinforced concrete/masonry structures are expected to lose almost all of their resistance before reaching large strains, thus making small strain theory suitable.

The shell element of this thesis incorporates a corotational approach to account for large rotations and displacements. The main idea behind the corotational framework is that the local coordinate system follows the rigid body motion of the element (Figure 3.8).

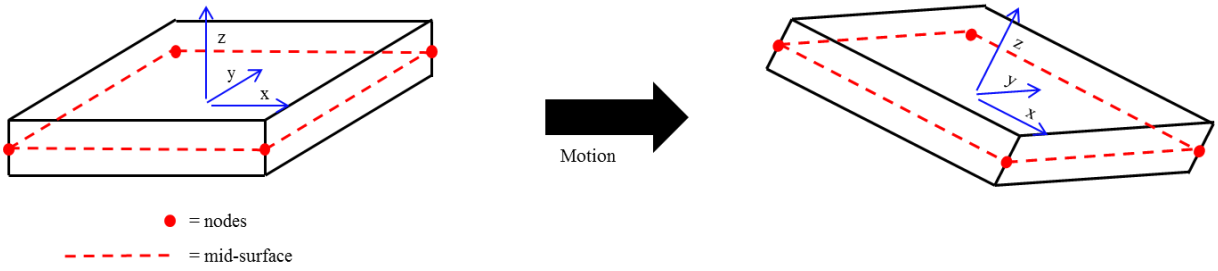

Figure 3.8: Demonstration of Local Coordinate System following Rigid Body Motion

The two major steps in the corotational process are calculating the rigid body motion of the local coordinate system and subtracting out the rigid body displacements/rotations from the total displacements/rotations. Once these two steps are completed, the deformational displacements and rotations are obtained. After the deformational displacements and rotations are known, strains and stresses can be determined using compatibility and constitutive relationships.

Belytschko and Hsieh (1973) developed a corotational approach to account for large rotations of a beam element (having only one rotation). Rankin and Brogan (1986) extended this approach to large rotation analysis in three dimensions. The Rankin and Brogan (1986) approach is implemented in the proposed shell element. The following steps give a brief overview on how the shell element accounts for large rotations/displacements:

1. Find the initial coordinate transformation matrix, $[E_o]$, in the original configuration that relates the global and local element coordinate axes.

2. Find the current coordinate transformation matrix, [E], in the new, deformed configuration that relates the global and local element coordinate axes.

3. Calculate the deformational part of the displacements in the local coordinate system.

$$\{u'\} = [E]^T \times (\{u\} + \{x\}) - \{x'\} \quad \textbf{(36)}$$

{u} = nodal displacements/rotations in the global coordinate system

{x} = nodal coordinates in global coordinate system in undeformed configuration

{x'} = nodal coordinates in local coordinate system in deformed configuration

4. Remove the rigid body rotation from the total nodal rotations.

The three rotations at each node in the global coordinate system are expressed by a triad (three rotations), which is rigidly attached to the node. The triad rotates with the respective node from the initial state (axes are parallel to global coordinate system axes), S_o, to its current, deformed state, S. This rotation is expressed by a transformation matrix, $[T_s]$, and is updated incrementally.

$$[T_s]_{new} = [T] \times [T_s]_{old} \quad \textbf{(37)}$$

$$[T_s]_{initial} = [I] \text{ (i.e. no rotation has taken place)} \quad \textbf{(38)}$$

$$[T] = [I] + \frac{1}{1 + \frac{|w|^2}{4}} \times ([\Omega] + 0.5 \times [\Omega]^2) \quad \textbf{(39)}$$

The above expression for [T] is second-order accurate.

*Note: $[T]^T[T] = [I]$ can be verified.

$$[\Omega] = \begin{bmatrix} 0 & -\delta\theta_z & \delta\theta_y \\ \delta\theta_z & 0 & -\delta\theta_x \\ -\delta\theta_y & \delta\theta_x & 0 \end{bmatrix} \quad \textbf{(40)}$$

$$[\Omega]^2 = \begin{bmatrix} -\delta\theta_z{}^2 - \delta\theta_y{}^2 & \delta\theta_x \times \delta\theta_y & \delta\theta_x \times \delta\theta_z \\ \delta\theta_x \times \delta\theta_y & -\delta\theta_z{}^2 - \delta\theta_x{}^2 & \delta\theta_z \times \delta\theta_y \\ \delta\theta_x \times \delta\theta_z & \delta\theta_y \times \delta\theta_z & -\delta\theta_x{}^2 - \delta\theta_y{}^2 \end{bmatrix} \quad \textbf{(41)}$$

where $|w|^2 = \delta\theta_x^2 + \delta\theta_y^2 + \delta\theta_z^2$, and

$\delta\theta_x$, $\delta\theta_y$, $\delta\theta_z$ are nodal rotation increments.

Once $[T_s]_{new}$ is known, $[\bar{T}]$ can be expressed in the current local coordinate system.

$$[\bar{T}] = [E]^T \times [T_s] \times [E_0] \quad \textbf{(42)}$$

It is important to note the approach is second-order accurate and therefore is approximate. The "pure" rotations or the deformational rotations can now be found using the following equations. These are the deformational nodal rotations in the local coordinate system with the rigid body rotations subtracted out of the total rotations.

$$[\Omega]_{pure} = 2 \times ([\bar{T}] - [I]) \times ([\bar{T}] + [I])^{-1} \quad \textbf{(43)}$$

Then, it is known that

$$[\Omega]_{pure} = \begin{bmatrix} 0 & -\theta^{E3} & \theta^{E2} \\ \theta^{E3} & 0 & -\theta^{E1} \\ -\theta^{E2} & \theta^{E1} & 0 \end{bmatrix} \quad \textbf{(44)}$$

Where θ^{E1}, θ^{E2}, θ^{E3} constitute the deformational rotation vector at the respective node. A more detailed formulation of the corotational approach to handle large rotations in three dimensions can be found in Rankin and Brogan (1986) and Nour-Omid and Rankin (1991).

3.1.2: Calculation of Stress Resultants and Nodal Forces/Moments

From the previous sections, the generalized strains (bending curvatures and membrane strains) are determined from the nodal displacements and rotations. The stresses, stress resultants (membrane forces and moments per unit length) and nodal forces/moments are determined in this section. The shell element discussed in this thesis allows for six integration points through the thickness with corresponding materials consisting of either concrete/fully-grouted masonry or smeared reinforcing steel. Each material is assumed to be in a state of two-

dimensional plane stress and therefore only two-dimensional constitutive laws are needed. The smeared reinforcing steel can only carry load in the specified uniaxial direction.

The in-plane strains at each integration point through the thickness are determined using the membrane strains at mid-surface and the curvatures from the bending behavior as shown below.

$$\varepsilon_x^i = \varepsilon_{mx} + z \times \phi_x; \quad \varepsilon_y^i = \varepsilon_{my} + z \times \phi_y; \quad \varepsilon_{xy}^i = \varepsilon_{mxy} + z \times \phi_{xy} \qquad \textbf{(45), (46), (47)}$$

$\varepsilon_x^i, \varepsilon_y^i, \varepsilon_{xy}^i =$ two-dimensional in-plane strains at integration point i

$\varepsilon_{mx}, \varepsilon_{my}, \varepsilon_{mxy} =$ membrane strains in the x-y plane at the mid-surface of the element

$z =$ distance from mid-surface of element to the integration point i

$\phi_x, \phi_y, \phi_{xy} =$ bending and twisting curvatures in the x-y plane

Once the in-plane strains are determined, the in-plane stresses can be determined at each integration point through the thickness using the shell element's two-dimensional, plane stress constitutive relationships.

$$\begin{Bmatrix} \sigma_x^i \\ \sigma_y^i \\ \sigma_{xy}^i \end{Bmatrix} = f(\begin{Bmatrix} \varepsilon_x^i \\ \varepsilon_y^i \\ \varepsilon_{xy}^i \end{Bmatrix}) \qquad \textbf{(48)}$$

$\sigma_x^i, \sigma_y^i, \sigma_{xy}^i =$ normal x, y stresses and in-plane shear stress (respectively) at integration point i

$f(\varepsilon) =$ represents the two-dimensional, plane stress constitutive model at integration point i

After the in-plane stresses are obtained, the stress resultants (membrane forces and moments per unit width) are found using one-dimensional Lobatto quadrature. Six integration

points are used to numerically integrate the stress distribution through the thickness to determine stress resultants. The integration points and respective weights can be seen in Table 3.1.

Table 3.1: Location of Quadrature Points and Values of Weighting Coefficients for One-dimensional Lobatto Quadrature

Lobatto Integration Point Number, i	Integration Point, ξ_i	Weight, w_i
1	-1.000000	0.066667
2	-0.765055	0.378475
3	-0.285232	0.554858
4	0.285232	0.554858
5	0.765055	0.378475
6	1.000000	0.066667

The following equations show how the stress resultants for each element are found using one-dimensional Lobatto quadrature. Mapping from the physical space (z, through-thickness dimension) to the parametric space (ξ) is established first.

$$z(\xi) = a \times \xi + b \quad \textbf{(49)}$$

$$a = \frac{z_2 - z_1}{2} \quad \text{and} \quad b = \frac{z_2 + z_1}{2} \quad \textbf{(50), (51)}$$

Since the integration is through the thickness,

$$z_2 = \frac{h}{2} \quad \text{and} \quad z_1 = \frac{-h}{2} \quad \textbf{(52)}$$

$$\text{where } h = \text{thickness of shell element}$$

Therefore,

$$a = \frac{h}{2}, b = 0 \text{ and } z(\xi) = \frac{h}{2} \times \xi \quad \textbf{(53), (54), (55)}$$

The Jacobian, J, is then determined.

$$J(\xi) = \frac{dz}{d\xi} = \frac{h}{2} \tag{56}$$

Lobatto integration is then used to numerically integrate the stress distribution through the thickness to find the stress resultants as seen in Figure 3.9.

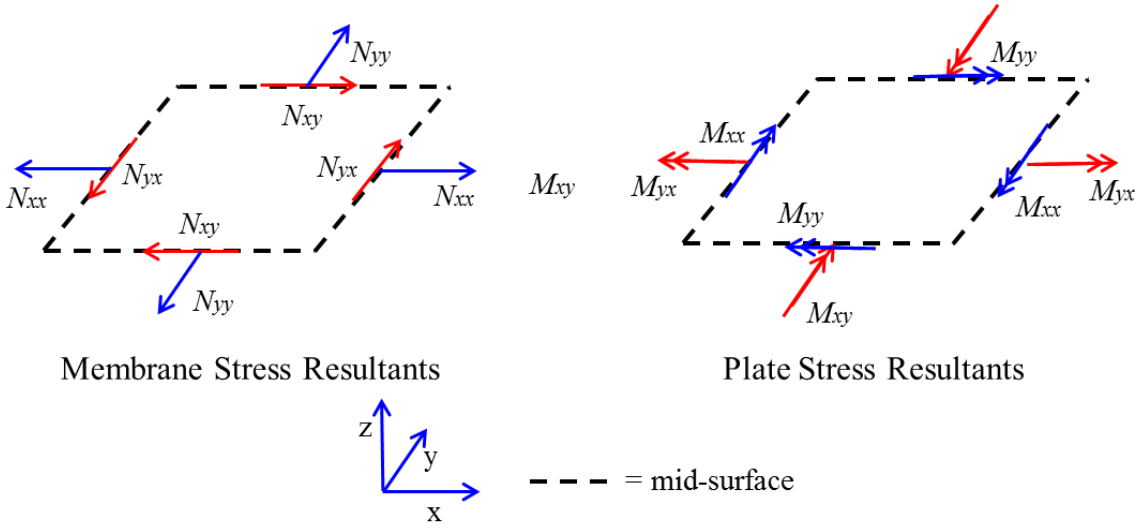

Figure 3.9: Stress Resultants

$$N_{xx} = \int_{-h/2}^{h/2} \sigma_x dz = \int_{-1}^{1} \sigma_x(z(\xi)) \times J(\xi) d\xi = \sum_{i=1}^{6} \sigma_x^i(z(\xi_i)) \times w_i \times J(\xi_i) \tag{57}$$

$$N_{yy} = \int_{-h/2}^{h/2} \sigma_y dz = \int_{-1}^{1} \sigma_y(z(\xi)) \times J(\xi) d\xi = \sum_{i=1}^{6} \sigma_y^i(z(\xi_i)) \times w_i \times J(\xi_i) \tag{58}$$

$$N_{xy} = \int_{-h/2}^{h/2} \sigma_{xy} dz = \int_{-1}^{1} \sigma_{xy}(z(\xi)) \times J(\xi) d\xi = \sum_{i=1}^{6} \sigma_{xy}^i(z(\xi_i)) \times w_i \times J(\xi_i) \tag{59}$$

$$\begin{aligned} M_{xx} &= \int_{-h/2}^{h/2} \sigma_x z dz = \int_{-1}^{1} \sigma_x(z(\xi)) \times \frac{h}{2} \times \xi \times J(\xi) d\xi \\ &= \sum_{i=1}^{6} \sigma_x^i(z(\xi_i)) \times \frac{h}{2} \times \xi_i \times w_i \times J(\xi_i) \end{aligned} \tag{60}$$

$$M_{yy} = \int_{-h/2}^{h/2} \sigma_y z dz = \int_{-1}^{1} \sigma_y\big(z(\xi)\big) \times \frac{h}{2} \times \xi \times J(\xi) d\xi$$
$$= \sum_{i=1}^{6} \sigma_y^i(z(\xi_i)) \times \frac{h}{2} \times \xi_i \times w_i \times J(\xi_i) \quad \textbf{(61)}$$

$$M_{xy} = \int_{-h/2}^{h/2} \sigma_{xy} z dz = \int_{-1}^{1} \sigma_{xy}\big(z(\xi)\big) \times \frac{h}{2} \times \xi \times J(\xi) d\xi$$
$$= \sum_{i=1}^{6} \sigma_{xy}^i(z(\xi_i)) \times \frac{h}{2} \times \xi_i \times w_i \times J(\xi_i) \quad \textbf{(62)}$$

N_{xx}, N_{yy}, N_{xy} = membrane stress resultants = membrane forces per unit width

M_{xx}, M_{yy}, M_{xy} = plate stress resultants = bending moments per unit width

i = Lobatto integration point

This through thickness integration approach with Lobatto quadrature offers a convenient and simplified way of determining stress resultants. It also allows for nonlinear material property variation through the thickness of the shell element.

Gauss quadrature is utilized to determine nodal forces and moments for each shell element from the aforementioned stress resultants. A 2x2 integration (4 integration points) scheme is used to perform the two-dimensional numerical integration. The location of quadrature points and values of weighting coefficients for 2x2 Gauss quadrature can be found in Table 3.2.

Table 3.2: Location of Quadrature Points and Values of Weighting Coefficients for 2x2 Gauss Quadrature

Gauss Integration Point Number, i	Integration Point, ξ_i	Integration Point, η_i	Weight, w_i
1	-0.577350	-0.577350	1.000000
2	0.577350	-0.577350	1.000000
3	0.577350	0.577350	1.000000
4	-0.577350	0.577350	1.000000

The membrane forces at each of the four nodes are determined using the following equation.

$$\{f_m\} = \sum_{i=1}^{4} [B^{Q4}(\xi_i, \eta_i)]_i^T \times \{\sigma_m^{res}(\xi_i, \eta_i)\} \times J(\xi_i, \eta_i) \times w_i \quad \textbf{(63)}$$

Where,

$$\{f_m\} = \text{membrane nodal force vector (in-plane nodal forces)} = \begin{Bmatrix} f_{x1} & f_{y1} & f_{x2} & f_{y2} & f_{x3} & f_{y3} & f_{x4} & f_{y4} \end{Bmatrix}^T \quad \textbf{(64)}$$

$$\{\sigma_m^{res}\} = \text{membrane stress resultant vector} = \begin{Bmatrix} N_x \\ N_y \\ N_{xy} \end{Bmatrix} \quad \textbf{(65)}$$

$J(\xi_i, \eta_i) =$ determinant of 2x2 Jacobian matrix at each Gauss integration point

i = Gauss integration point

The out-of-plane forces and moments at each of the four nodes are found using the following equation.

$$\{f_f\} = \sum_{i=1}^{4} [B_f(\xi_i, \eta_i)]_i^T \times \{\sigma_f^{res}(\xi_i, \eta_i)\} \times J(\xi_i, \eta_i) \times w_i \quad \textbf{(66)}$$

Where,

$$\{f_f\} = \text{out-of-plane nodal forces and moments} = \begin{Bmatrix} f_{z1} & m_{x1} & m_{y1} & f_{z2} & m_{x2} & m_{y2} & f_{z3} & m_{x3} & m_{y3} & f_{z4} & m_{x4} & m_{y4} \end{Bmatrix}^T \quad \textbf{(67)}$$

$J(\xi_i, \eta_i) =$ determinant of 2x2 Jacobian matrix at each Gauss integration point

i = Gauss integration point

It is important to note the nodal forces/moments are determined from the nodal displacements/rotations.

3.2: Material Models

The material at each Lobatto point through the thickness is assumed to be in a state of two-dimensional plane stress and can be either concrete/fully-grouted masonry or smeared steel reinforcement. The shell element employs a two-dimensional plane stress, fixed smeared-crack model developed by Koutromanos (2011). Fully-grouted masonry has a similar behavior to that of concrete. Thus, the same type of material model is used for both concrete and masonry.

3.2.1: Smeared-crack Continuum Material Model

The smeared-crack approach averages or "smears" the effects of cracks across a nonzero crack-band length, which for constant strain conditions equals the element length. There are two different approaches when using a smeared-crack model. The first approach is the rotating-crack model, which allows two cracks to form at each Gauss point and the direction of each crack continuously rotates to be consistent with the direction of the orthogonal principal strain axes (Kim et al. 2002). This method is not suitable for cyclic loads (Kim et al 2002). The second method, which is implemented in the shell element discussed in this thesis, is the fixed smeared-crack model. In this approach, two orthogonal cracks can occur at each Gauss point and the orientations of the cracks remain fixed after the maximum principal stress exceeds the tension cutoff criterion of the material.

The uncracked material is described by the composite yield surface shown in Figure 3.10, which expresses the combination of a von Mises criterion to capture inelastic behavior due to large compressive strains in the uncracked material and a tension cutoff criterion to detect

cracking. The isotropic strain hardening-softening law for von Mises strength can be seen in Figure 3.10b. When the plastic strain exceeds a threshold value, ε_{2p}, the concrete is assumed to be crushed and the tensile strength is reduced to a very small value. Preliminary analyses show that reducing the tensile strength to zero can cause issues with convergence. The first crack forms when the maximum principal stress reaches the tension limit (tension cutoff criterion). Once the material becomes cracked, a nonlinear orthotropic model is employed in the crack normal and parallel directions. The uniaxial stress-strain curves for the nonlinear orthotropic model are shown in Figure 3.11 for monotonic loading as well as unloading/reloading rules for cyclic loading. A second crack forms perpendicular to the first crack, when the stress parallel to the first crack reaches the tension limit of the material. The shear stress/strain law in the crack normal and parallel coordinate system is assumed to be elastic-perfectly plastic with the peak shear strength being half of the tensile strength of the concrete/masonry.

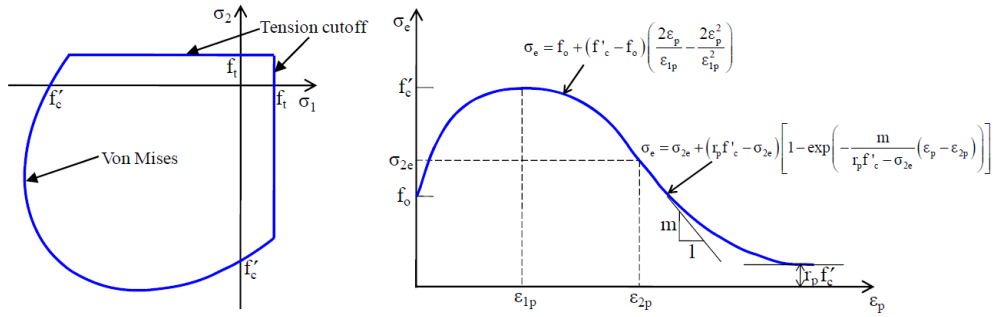

(a) Failure surface before tensile fracture

(b) Strain hardening-softening law for Von Mises strength

Figure 3.10: Isotropic Material Law before Fracture. Koutromanos, I. (2011), "Numerical Analysis of Masonry-Infilled Reinforced Concrete Frames Subjected to Seismic Loads and Experimental Evaluation of Retrofit Techniques." *Ph.D. Dissertation*, University of California, San Diego, La Jolla, CA, 355pp. Used under fair use, 2014.

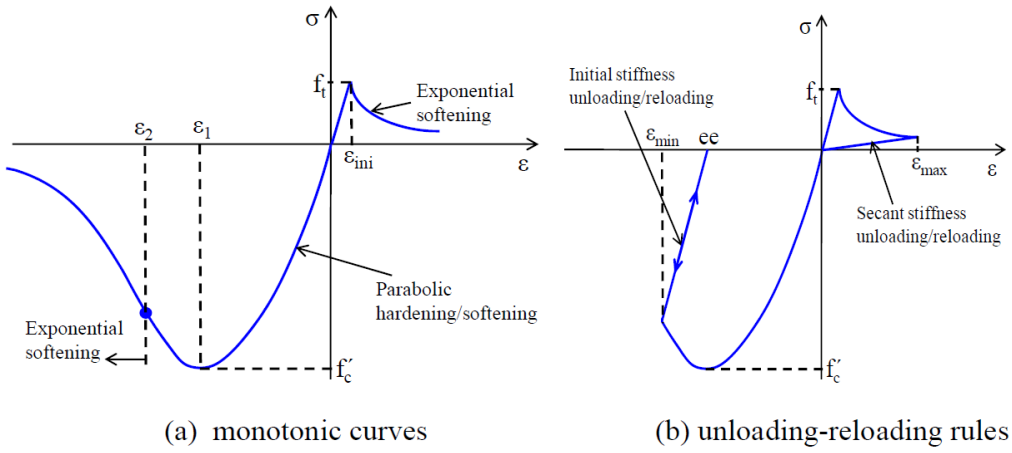

Figure 3.11: Orthotropic Material Law after Fracture. Koutromanos, I. (2011), "Numerical Analysis of Masonry-Infilled Reinforced Concrete Frames Subjected to Seismic Loads and Experimental Evaluation of Retrofit Techniques." *Ph.D. Dissertation*, University of California, San Diego, La Jolla, CA, 355pp. Used under fair use, 2014.

As seen in Figure 3.11b, the orthotropic material model employs a secant stiffness unloading/reloading rule under uniaxial tension and an initial stiffness unloading/reloading rule under uniaxial compression. Similar to the plasticity model, once the compressive strain exceeds a threshold value, ε_2, the concrete is considered crushed and the tensile strength is reduced to a small, residual value. A smooth transition is provided from the plasticity model to the nonlinear orthotropic model for the material that experiences inelastic compressive strains before cracking. Figure 3.12 shows this smooth transition and depicts the uniaxial cyclic behavior of the smeared-crack model starting with a compressive stress. The plasticity model gives the compressive constitutive law in the initial cycle. The compressive stress-strain relation in the following cycle is given by the nonlinear orthotropic model because the tension criterion has been reached (i.e. a crack has formed).

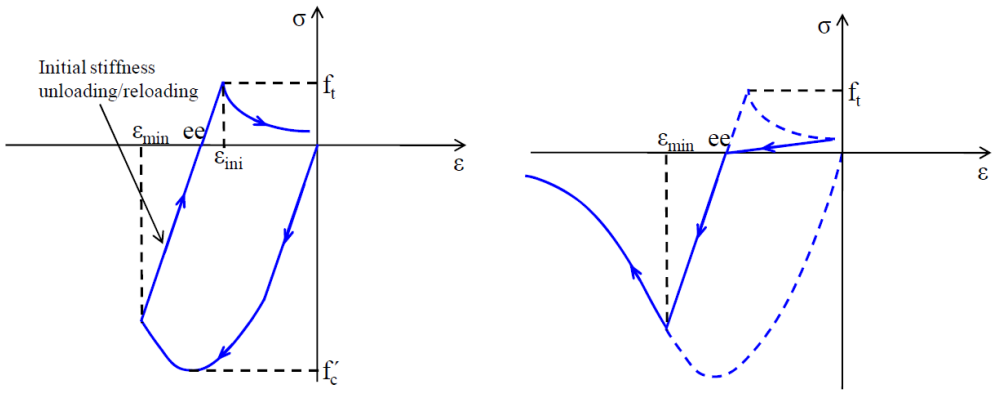

Figure 3.12: Uniaxial Cyclic Behavior of the Smeared-Cracked Model. Koutromanos, I. (2011), "Numerical Analysis of Masonry-Infilled Reinforced Concrete Frames Subjected to Seismic Loads and Experimental Evaluation of Retrofit Techniques." *Ph.D. Dissertation*, University of California, San Diego, La Jolla, CA, 355pp. Used under fair use, 2014.

3.2.2: Reinforcing Steel Material Model

The steel reinforcement can be modeled as smeared reinforcement at a specified location through the thickness of the shell element or as one-dimensional truss elements. A perfect bond is assumed between concrete and steel reinforcing bars. The material model for the smeared reinforcement is elasto-plastic with linear kinematic hardening. If one-dimensional truss elements are used to model the reinforcing steel, the elasto-plastic material model with linear hardening or the Dodd-Restrepo model can be implemented. The Dodd-Restrepo model more accurately reproduces the monotonic and cyclic loading (unloading and reloading) behavior of actual steel reinforcement. As seen in Figure 3.13, the Dodd-Restrepo model has a clear yield plateau and strain hardening region, which is consistent with empirical data. In addition, the Dodd-Restrepo steel material model captures the Bauschinger effect as seen in Figure 3.14.

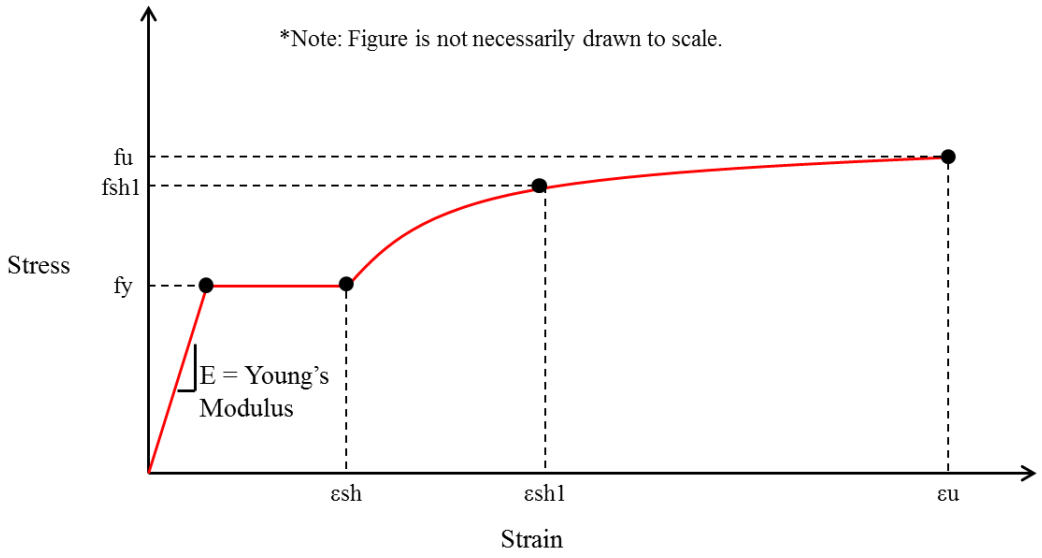

Figure 3.13: Dodd-Restrepo Monotonic Stress-Strain Curve

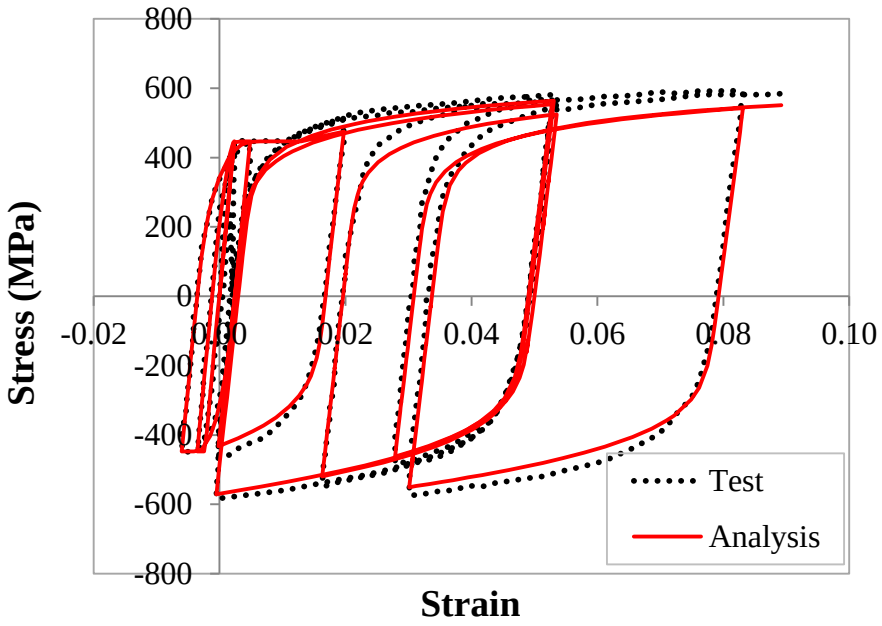

Figure 3.14: Dodd-Restrepo Cyclic Stress-Strain Curve (Koutromanos 2014)

3.3: Demonstration of Material Behavior

The primary purpose of this analysis is to demonstrate the nonlinear material behavior of concrete/masonry including the effect of transverse strains on the diagonal compression field of

cracked concrete. The shell element enables the user to implement this effect according to the expressions detailed in the Modified Compression Field Theory (MCFT) (Vecchio and Collins 1986). The effect of transverse strains on the diagonal compression field is accounted for by reducing the peak compressive strength of cracked concrete. Another objective of this analysis is to verify the smooth transition from isotropic (before fracture) to nonlinear orthotropic (after fracture) material models. To accomplish both of these objectives, a single shell element is subjected to pure in-plane shear and the effects of transverse strains on the diagonal compression field are both considered and neglected. For continued reference, this effect will be referred to as the biaxial effect.

The element is pinned at the bottom left node, restrained in the horizontal direction at the bottom right node and restrained in the vertical direction at the top left node as seen in Figure 3.15. The dimensions of the element are 50 in. x 50 in. x 8 in. (thickness). Compressive strength of concrete is 3.0 ksi, tensile strength is 0.4 ksi, and Young's modulus is 2,000 ksi. There is no reinforcement included in this analysis. The analysis is a static, displacement controlled simulation and the post-peak nonlinear behavior is desired. The maximum horizontal/vertical imposed nodal displacements are 0.2 inches as seen in Figure 3.15. The shear stress vs. shear strain curves are then plotted for the two analysis cases (biaxial effect considered and neglected) and can be found in Figure 3.16.

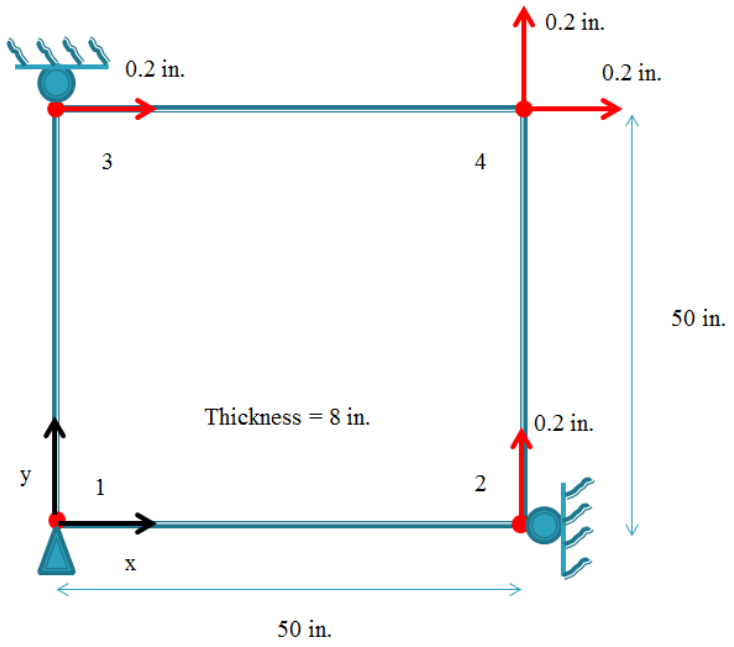

Figure 3.15: Single Element in Pure Shear

The transition is smooth from isotropic to orthotropic material models as seen in Figure 3.16. Point A on Figure 3.16 represents the maximum principal stress exceeding the tensile cutoff criterion (0.4 ksi) and hence when a crack forms. There is a small increase in strength at this point caused by the switch from isotropic (before fracture) to orthotropic (after fracture) material models. At this point, the compressive orthotropic strength of the concrete is slightly greater than the compressive isotropic strength and this behavior is supported by empirical evidence. Point B from Figure 3.16 represents the stress parallel to the crack reaching the peak compressive strength for the analysis with biaxial effect implemented while Point C represents the stress parallel to the crack reaching the peak compressive strength when the biaxial effect is neglected. As expected, the stress at Point C is greater than the stress at Point B, which means the parameter that accounts for the reduction in peak compressive strength due to the biaxial

effect is working properly. The softening is even steeper for the element that has implemented the biaxial effect and this is consistent with empirical results/data.

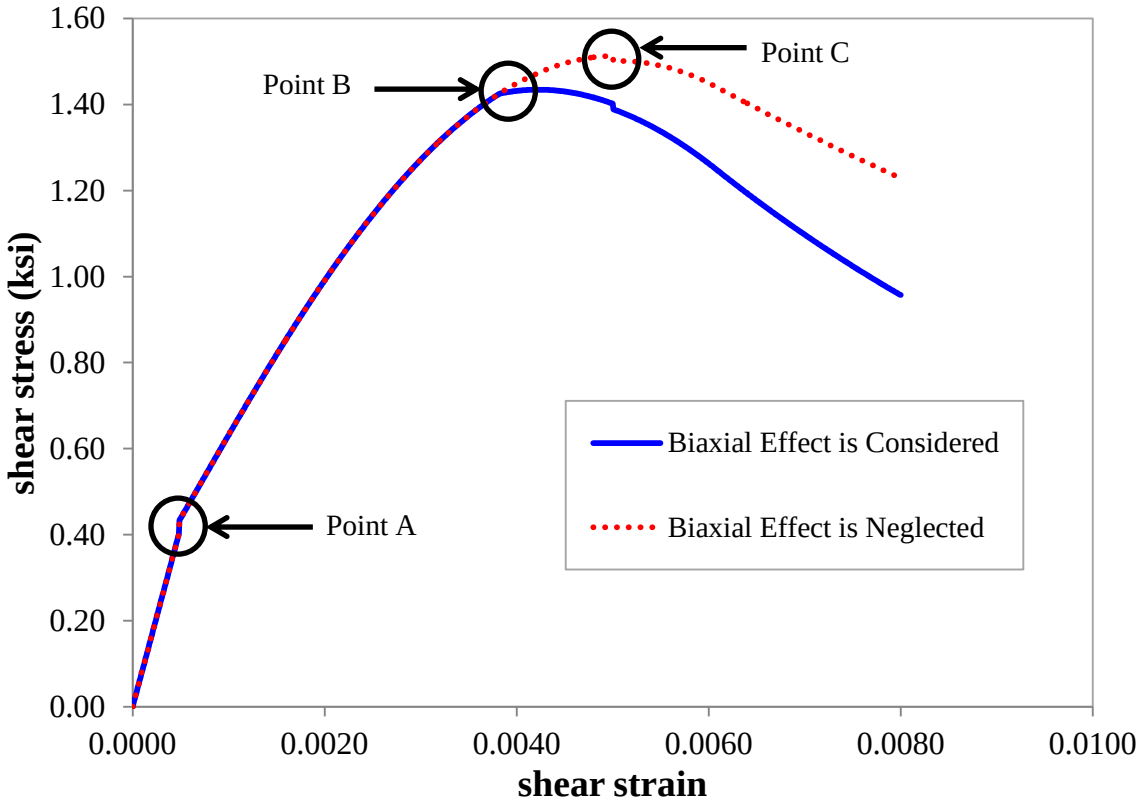

Figure 3.16: Shear Stress vs. Shear Strain for Single Element in Pure Shear

3.4: Demonstration of Spurious Mesh Size Effect

When using finite element modeling to analyze reinforced concrete/masonry structures, the size of the mesh spuriously affects the analytical results when softening occurs. This problem creates a lack of objectivity and inconsistencies in the softening portions of concrete stress/strain curves in tension and compression for different element sizes/meshes. The spurious mesh size effect is caused by localization of strain in certain elements once the peak compressive/tensile strength is reached. For tension, the lack of objectivity issue is resolved by adjusting the tension softening parameter, m_t, using the concrete fracture energy concept. The tension softening

parameter controls the exponential tensile softening of the material and is detailed in Koutromanos (2011). For compression, this problem is addressed by putting a single element with the same size as standard concrete test cylinders under pure uniaxial compression and matching the force-displacement compressive softening with a single element under pure uniaxial compression of the desired element size. The spurious mesh size effect as well as a solution to produce consistent softening of analytical results is demonstrated by conducting multiple analyses on a simple rectangular structure subjected to uniaxial tension.

In these analyses, a 5 in. x 1 in. x 0.25 in. (thickness) concrete (no steel reinforcement) rectangular structure was subjected to pure uniaxial tension. The concrete was assumed to have a Young's modulus, compressive strength, tensile strength and residual tensile strength of 2,000 ksi, 3.0 ksi, 0.4 ksi and 0.02 ksi respectively. Pure uniaxial tension was enforced using displacement-control at the two top nodes. The structure was discretized into three model variations, having 1, 2 and 4 elements along the long dimension (5 in. dimension). The 1 and 2 element models with loading and boundary conditions can be seen in Figure 3.17. The first analyses used a tension softening parameter of 700 (for every mesh) to see how the element/mesh size affected the analytical results when softening occurred. The stress-average strain curves for each mesh/element size were plotted and are shown in Figure 3.18.

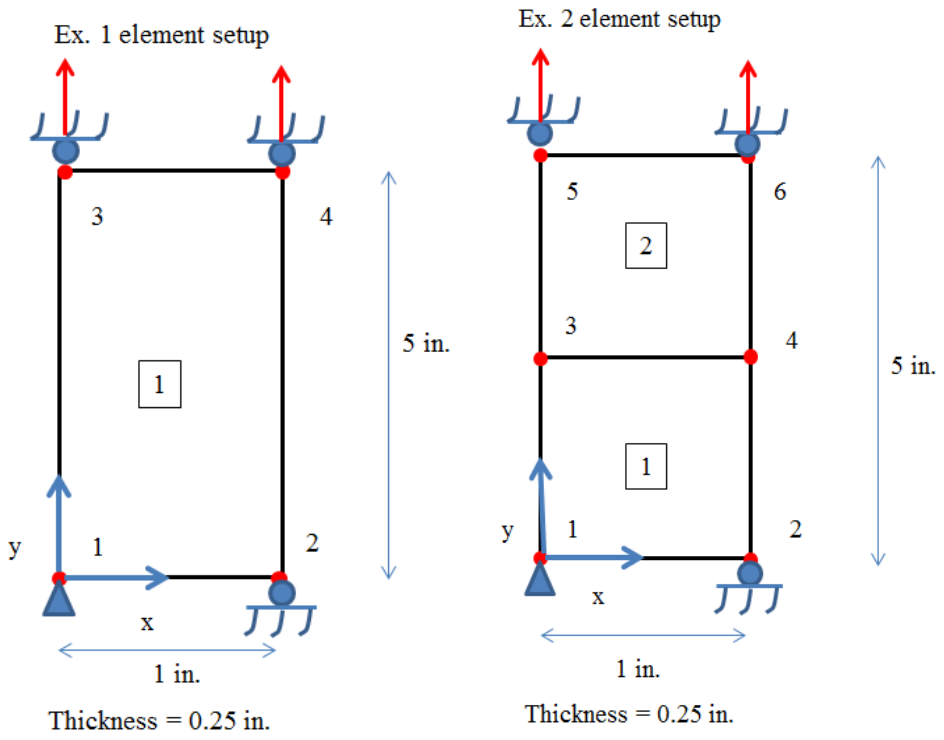

Figure 3.17: Uniaxial Tension Analysis Setup

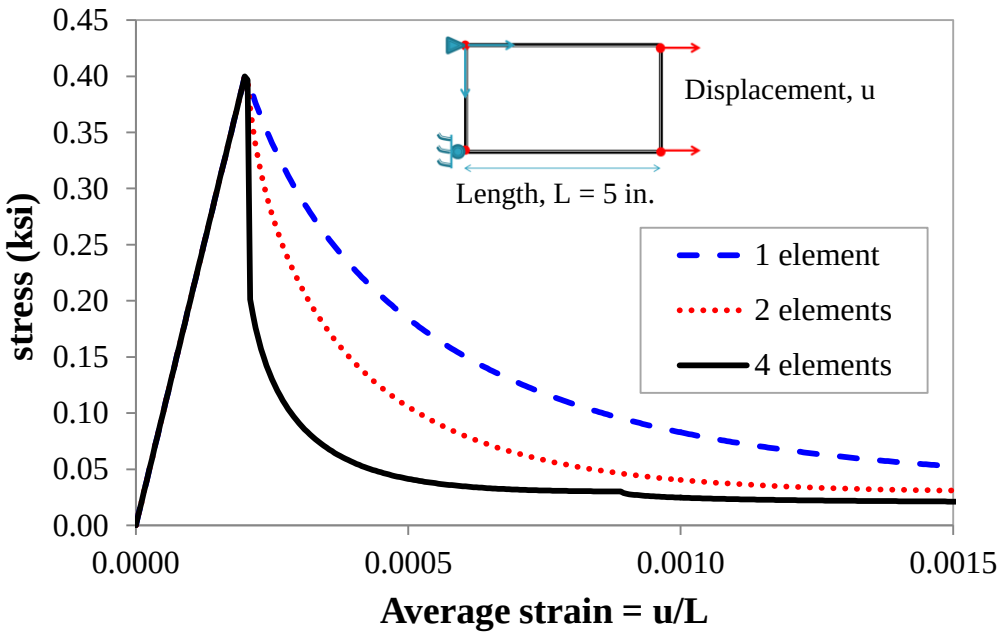

Figure 3.18: Uniaxial Tension Stress-Average Strain Curves before adjusting Tension Softening Parameters

As seen in Figure 3.18, the softening portions of the tension stress/strain curves were not consistent based on mesh/element size. The analysis with 1 element had the most shallow tension softening while the analysis with 4 elements had the steepest tension softening. This means the tension softening of the 1 element analysis needed to be made steeper and the tension softening of the 4 element analysis needed to be made more shallow. The cause of the spurious mesh size effect can be seen in Figure 3.19. When the four element analysis was at peak tensile strength (Figure 3.19(a)), there was the same amount of strain (0.0002) in each element. After strength degradation was initiated (Figure 3.19(b)), a large amount of strain (0.00074) localized in the top element. This localization of strain in certain elements produced inconsistencies in analytical results when softening occured based on the spurious mesh size effect.

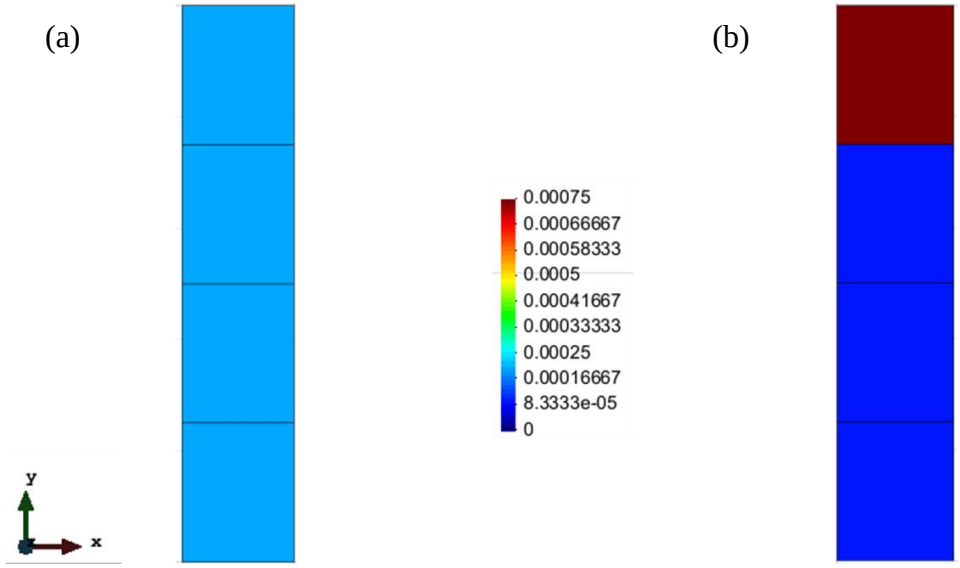

Figure 3.19: Strain ε_y at (a) Peak Tensile Strength and (b) after Initiation of Strength Degradation

The tension softening parameters were then adjusted using the concrete fracture energy concept. This concept utilizes an assumed concrete axial stress (f_c) vs. crack opening (u) curve as seen in Figure 3.20 (Panagiotou et al. 2012). The fracture energy, G_f, is found as the area under

the assumed f_c vs. u curve. The f_c vs. u curve is based on maximum aggregate size and the compressive strength of the concrete.

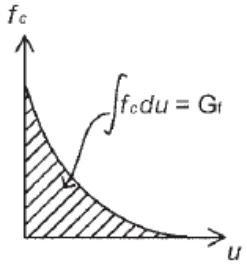

Figure 3.20: Assumed f_c vs. u Curve. Panagiotou, M., Restrepo, J., Schoettler, M., and Kim, G. (2012), "Nonlinear Cyclic Truss Model for Reinforced Concrete Walls." ACI Structural Journal: 205–214. Used under fair use, 2014.

It is important to note G_f is independent of mesh/element size. The strain, ε, is then found by smearing the effects of the crack opening, u, over the element size, L. The f_c vs. ε relationship can then be seen in Figure 3.21.

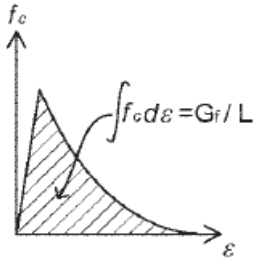

Figure 3.21: Uniaxial, Monotonic Assumed Stress-Strain Law. Panagiotou, M., Restrepo, J., Schoettler, M., and Kim, G. (2012), "Nonlinear Cyclic Truss Model for Reinforced Concrete Walls." ACI Structural Journal: 205–214. Used under fair use, 2014.

From Figure 3.21, the area under the uniaxial stress/strain curve is found to be:

$$g_f = \frac{G_f}{L} \tag{68}$$

The adjusted tension softening parameters can then be found using the following equations.

$$g_f = \frac{\Delta f \times f_t}{m_t} \tag{69}$$

$$m_{t,\,adjusted} = \frac{L \times \Delta f \times f_t}{G_f} \tag{70}$$

where $m_{t,\,adjusted}$ = adjusted tension softening parameter

$$\Delta f = f_t - f_{res} \tag{71}$$

f_t = tensile strength

f_{res} = residual tensile strength

The values of the adjusted tension softening parameters for the three different meshes can be found in Table 3.3. As expected, the adjusted tension softening parameter for the 1 element mesh is greater (steeper softening) and the adjusted tension softening parameter for the 4 element mesh is smaller (more shallow softening).

Table 3.3: Adjusted Tension Softening Parameters

fc' = 3 ksi, Length = 5 in., W = 1 in., t = 0.25 in.		
No. of elements	L (in)	m_t
1	5	1871.75
2	2.5	935.87
4	1.25	467.94

The uniaxial tension stress-average strain curves are again plotted in Figure 3.22 except now incorporating the adjusted tension softening parameters. The concrete fracture energy concept was able to regularize the tensile softening parameters, m_t, and produce consistent analytical results for different mesh/element sizes when softening occurred.

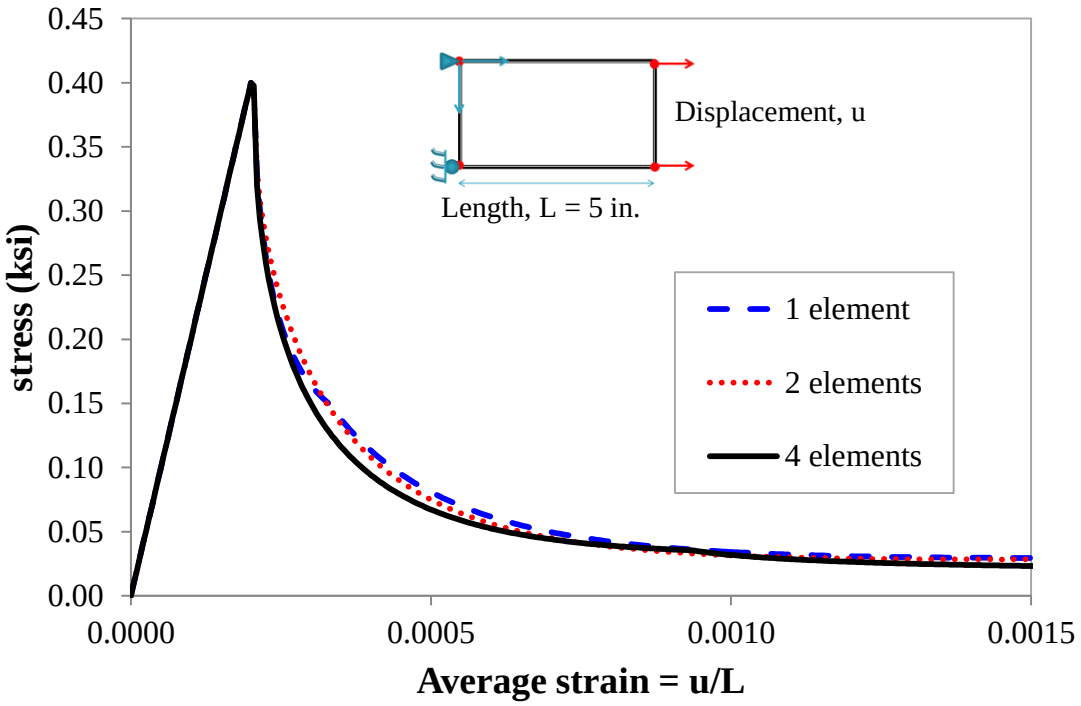

Figure 3.22: Uniaxial Tension Stress-Average Strain Curves after adjusting Tension Softening Parameters

Chapter 4: Verification of Element Kinematics

4.1: Introduction

The shell element formulations and material models presented in Chapter 3 are validated here and in Chapter 5 against experimental data and theoretical solutions. The results of these verification analyses will determine the accuracy of the model and the aforementioned methodology. In this chapter, the shell element is used to analyze several elastic structures with the modeling results compared to benchmark solutions. These elastic structures include cantilever and simply supported beams and plates, as well as three corotational approach verifications involving cantilevered walls and a single element subjected to three-dimensional rigid body motion. Next, in Chapter 5, the shell element is validated against experimental results of reinforced concrete and reinforced masonry structures.

4.2: Elastic Cantilever Beam

The first benchmark analysis was conducted for a cantilever beam subjected to a single transverse load at the tip. The purpose of this analysis was to validate the shell element against a simple, elastic example as well as to observe response differences between element size and aspect ratios. The boundary conditions, load (10 kips), length of beam, beam thickness (6 in.) and Young's modulus (E = 2,500 ksi) were held constant while the element size, element aspect ratio and beam cross section width were varied. Two different analysis cases were performed. Case 1 utilizes rectangular elements across a series of analyses using 2, 4, 8 and 16 elements to discretize the beam. Case 2 utilizes 8 square elements along a narrower beam and was for results comparison with the 8 rectangular elements analysis in Case 1. Pertinent material and geometric properties can be seen in Figure 4.1.

The deflection at the tip of the beam was recorded and compared with the exact theoretical solution. Figure 4.2 displays the results of the analysis (labeled "approximate") as a ratio of the exact solution. The results matched well with the theoretical solution for all element sizes with increasing accuracy as more elements are used. This was expected as finer meshes better approximate the theoretical deformed shape. Further, the accuracy is slightly increased when using the square elements vs. the rectangular elements. Bending about the x-axis was also observed in these analyses, since the rotations about the x-axis, θ_x, were not restrained along the beam member. In fact, the rotations in the narrow beam (case 2) were slightly higher than the wide beam (case 1) causing the small difference between the deflection results for the square vs. rectangular elements.

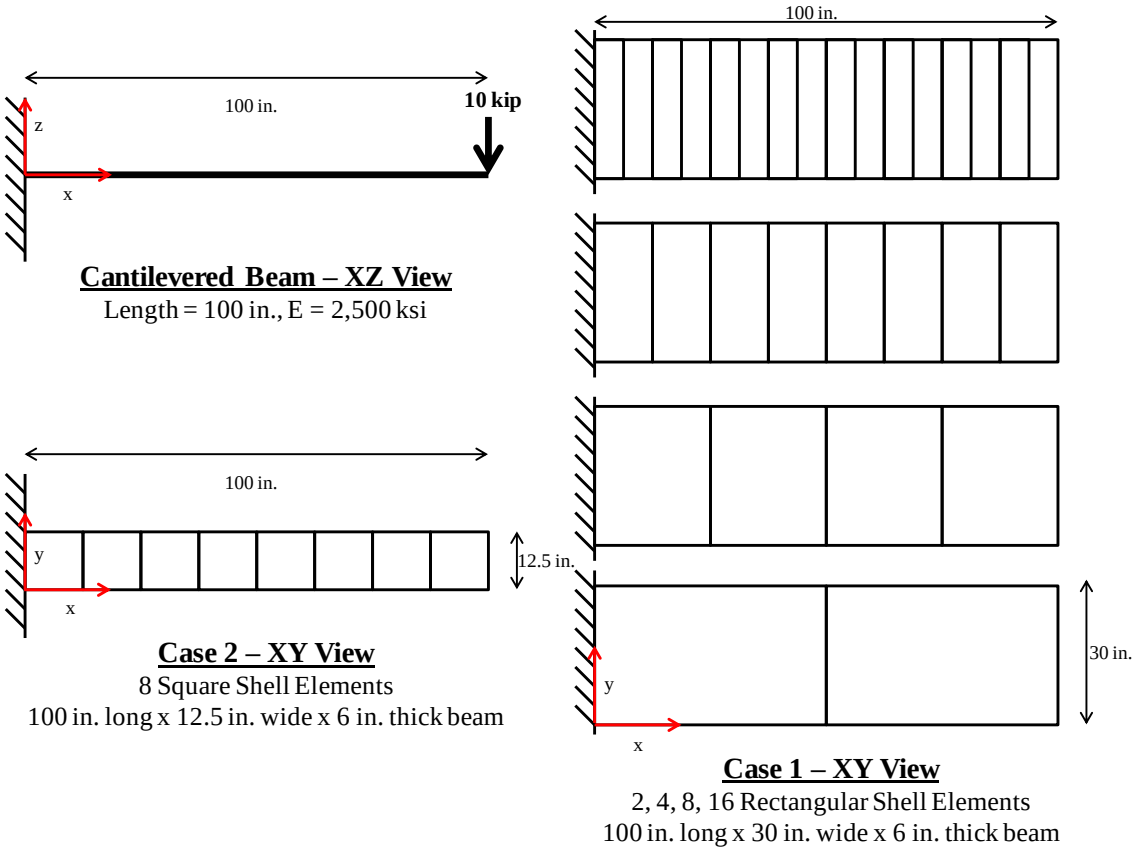

Figure 4.1: Geometric and Material Properties for Elastic Cantilever Beam

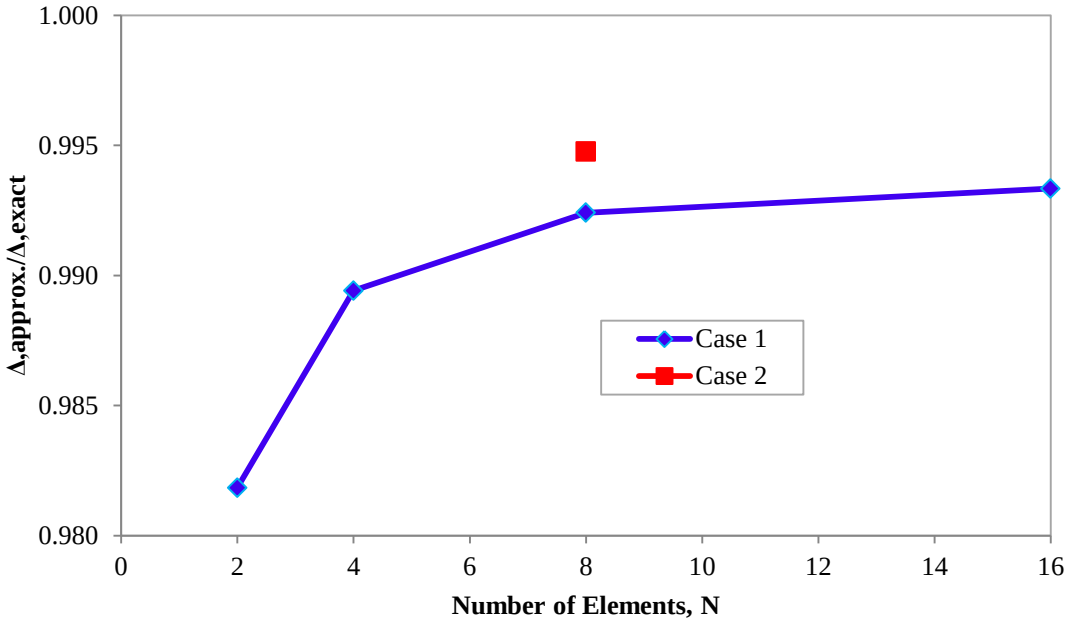

Figure 4.2: Elastic Cantilever Beam, Tip Deflection Results - shown as a ratio of analytical results divided by exact results

4.3: Elastic Simply Supported Beam

The second benchmark analysis was conducted for a simply supported beam with a static load applied at midspan. The purpose of this analysis is to validate the shell element against a simple, elastic example as well as to observe the effects of the element aspect ratio. The boundary conditions, load (10 kip), length of beam, beam thickness (6 in.), number of elements (8) and Young's modulus (E = 2,500 ksi) are held constant while the beam cross section width and related element aspect ratio are varied. Two different analysis cases are performed. Case 1 utilizes 8 rectangular elements across the length of the beam. Case 2 utilizes 8 square elements across a narrower beam. Pertinent material and geometric properties can be seen in Figure 4.3. The deflection at midspan was measured and compared to the exact solution. Figure 4.4 displays the results of the analysis (labeled "approximate") as a ratio of the exact, theoretical solution.

The model was very accurate for both cases, with slight accuracy gained when using the square vs. rectangular elements. Bending about the x-axis was also observed in these analyses, since the rotations about the x-axis, θ_x, again were not restrained along the beam member. As in the prior analysis, the rotations in the narrow beam (case 2) were slightly higher than the wide beam (case 1) causing the small difference between the deflection results for the square vs. rectangular elements.

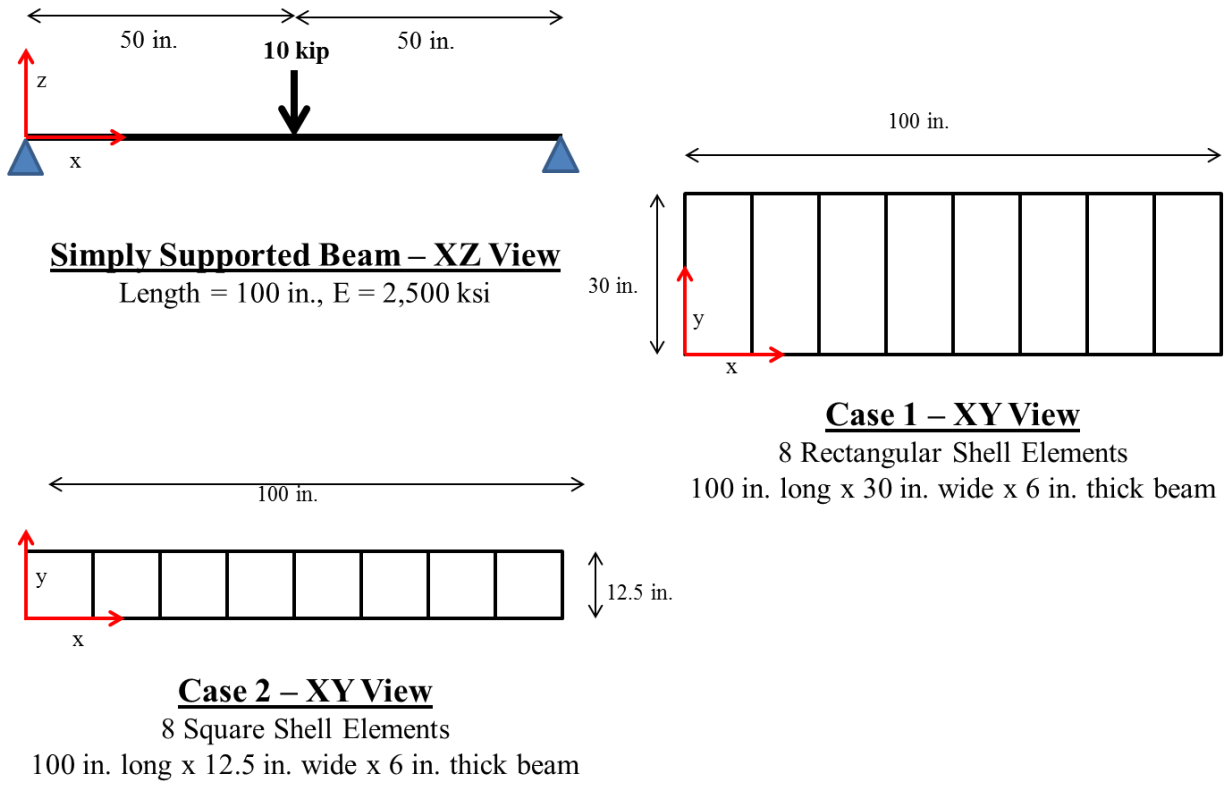

Figure 4.3: Geometric and Material Properties for Elastic Simply Supported Beam

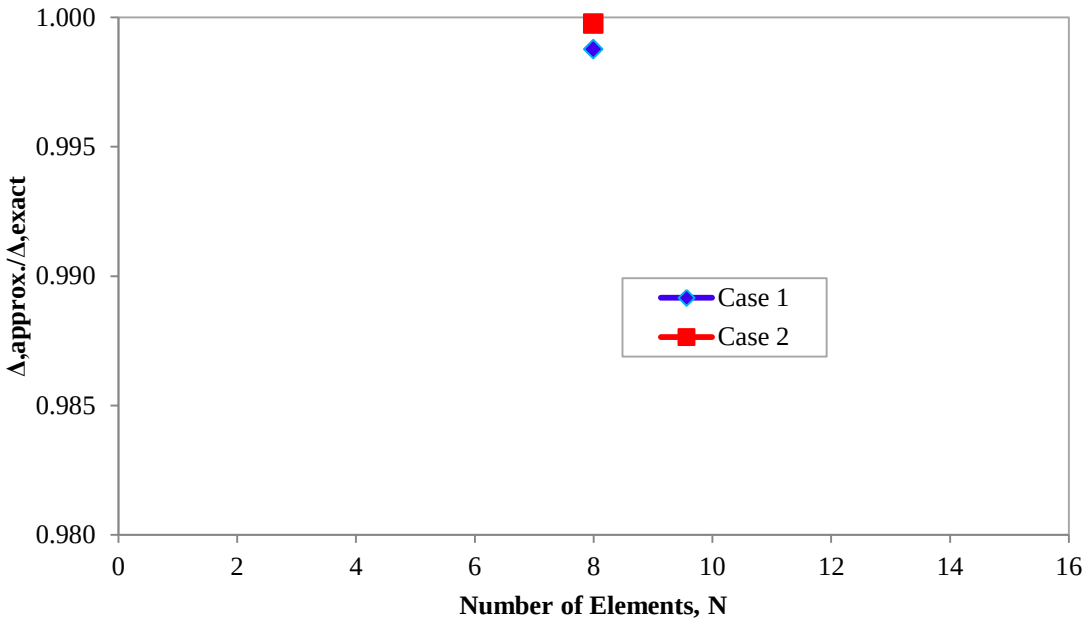

Figure 4.4: Elastic Simply Supported Beam, Midspan Deflection Results - shown as a ratio of analytical results divided by exact results

4.4: Elastic Simply Supported Plate

An elastic square plate having simple supports along its perimeter and subjected to a uniform normal load was then analyzed. This validation analysis was intended to observe the effects of a more refined mesh (smaller elements) on the accuracy of the results. Square elements were used to discretize the plate with analyses conducted using 4 (2 elements along each side), 16, and 64 elements. A uniform load of 0.1 ksi was applied normal to the face of the plate in the z-direction. The material and geometric properties can be seen in Figure 4.5.

The out-of-plane deflection was computed at the center of the slab and compared with the exact, theoretical solution. Figure 4.6 displays the results of the analysis (labeled “approximate”) as a ratio of the exact solution. The shell element satisfactorily predicted the center out-of-plane

deflection for all mesh/element sizes. The accuracy of the model significantly increased when refining the mesh from 4 elements ($\Delta_{analysis}$ / Δ_{exact} = 0.93) to 16 elements ($\Delta_{analysis}$ / Δ_{exact} = 0.995). The increase of accuracy by refining the mesh from 16 ($\Delta_{analysis}$ / Δ_{exact} = 0.995) to 64 ($\Delta_{analysis}$ / Δ_{exact} = 0.998) elements was not nearly as significant. Therefore, it seems that the optimal mesh for this analysis was 16 square elements. The increase in accuracy due to refining the mesh is caused by the assumed deformation pattern more closely approximating the theoretical deformed shape.

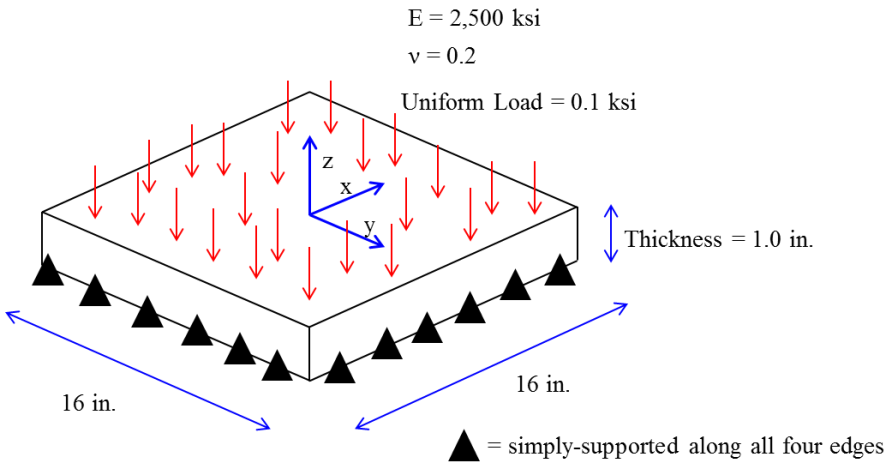

Figure 4.5: Geometric and Material Properties for Elastic Simply Supported Plate

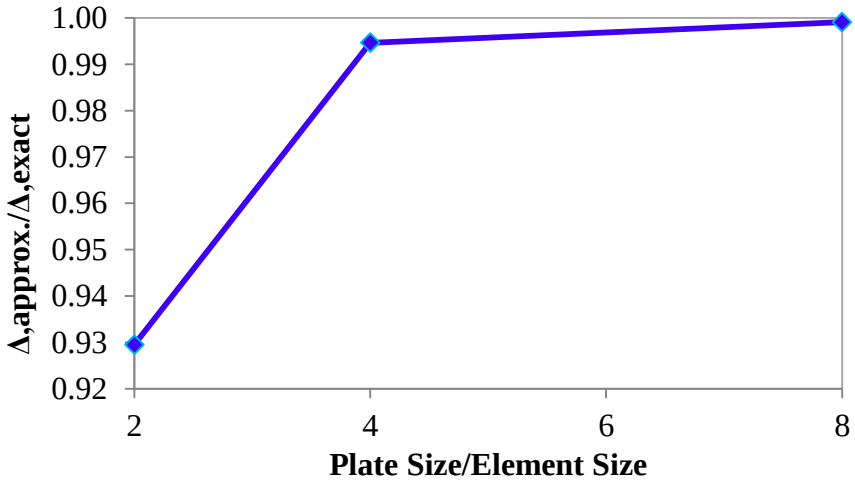

Figure 4.6: Elastic Simply Supported Plate, Center Point Deflections - shown as a ratio of analytical results divided by exact results

4.5: Elastic Cantilever Plate – Case 1

Batoz and Tahar (1982) describe a finite element analysis study of a linear elastic plate fixed on one end and twisted at the other, free end as seen in Figure 4.7. They compare single element model solutions across a number of plate bending finite element formulations, providing another benchmark suitable for verifying the shell element of this thesis. One element is used to model the entire plate, with the free end of the plate twisted by applying equal and opposite unit normal direction forces at each free corner node. The modulus of elasticity, Poisson's ratio and thickness of the cantilever plate element respectively are 10^7 ksi, 0.25 and 0.05 in. The length of the beam/plate in the analysis is varied and the out-of-plane displacement, w, at the free end is plotted against the length, as seen in Figure 4.7.

Batoz and Tahar (1982) reported the results of their Discrete Kirchhoff quadrilateral (DKQ) plate element compared to those of several previously established reference elements, including rectangular elements, quadrilateral elements and quadrilateral elements formed from four triangular elements. A more detailed description of the DKQ and reference elements can be found in Batoz and Tahar (1982). The results for the shell element of this thesis display very good agreement to the results of the DKQ element in Batoz and Tahar, presenting further evidence to the validity of this shell element. This is not surprising as the DKQ element proposed by Batoz and Tahar forms the basis for the plate bending formulations in the shell element of this thesis.

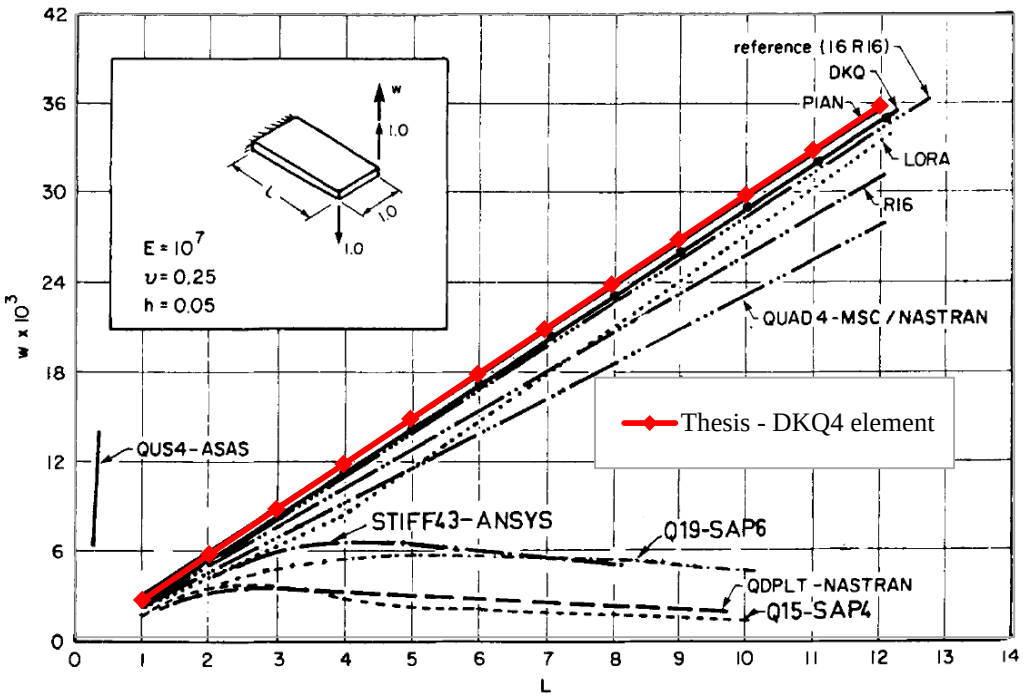

Figure 4.7: Elastic Cantilever Plate – Case 1. Batoz, J.-L., and Tahar, B. 1982, "Evaluation of a New Quadrilateral Thin Plate Bending Element." *International Journal for Numerical Methods in Engineering* 18 (11): 1655–77. Used under fair use, 2014.

4.6: Elastic Cantilever Plate – Case 2

Batoz and Tahar (1982) include another analysis where a plate is fixed on one end and twisted at the other, free end as seen in Figure 4.8. The free end is twisted by applying equal and opposite unit twisting moments at each free node. Again, one element is used to model the entire plate. The modulus of elasticity, Poisson's ratio and thickness of the cantilever plate element respectively are 10^7 ksi, 0.25 and 0.05 in. The length of the plate in the test is varied and the out-of-plane displacement, w, at the free end is plotted against the length as seen in Figure 4.8.

Batoz and Tahar (1982) reported the results of their Discrete Kirchhoff quadrilateral (DKQ) plate element compared to those of several previously established reference elements,

including rectangular elements, quadrilateral elements and quadrilateral elements formed from four triangular elements. A more detailed description of the DKQ and reference elements can be found in Batoz and Tahar (1982). The results for the shell element of this thesis display very good agreement to the results of the DKQ element in Batoz and Tahar, again presenting further evidence to the validity of this shell element. Again, this is not surprising as the DKQ element proposed by Batoz and Tahar forms the basis for the plate bending formulations in the shell element of this thesis.

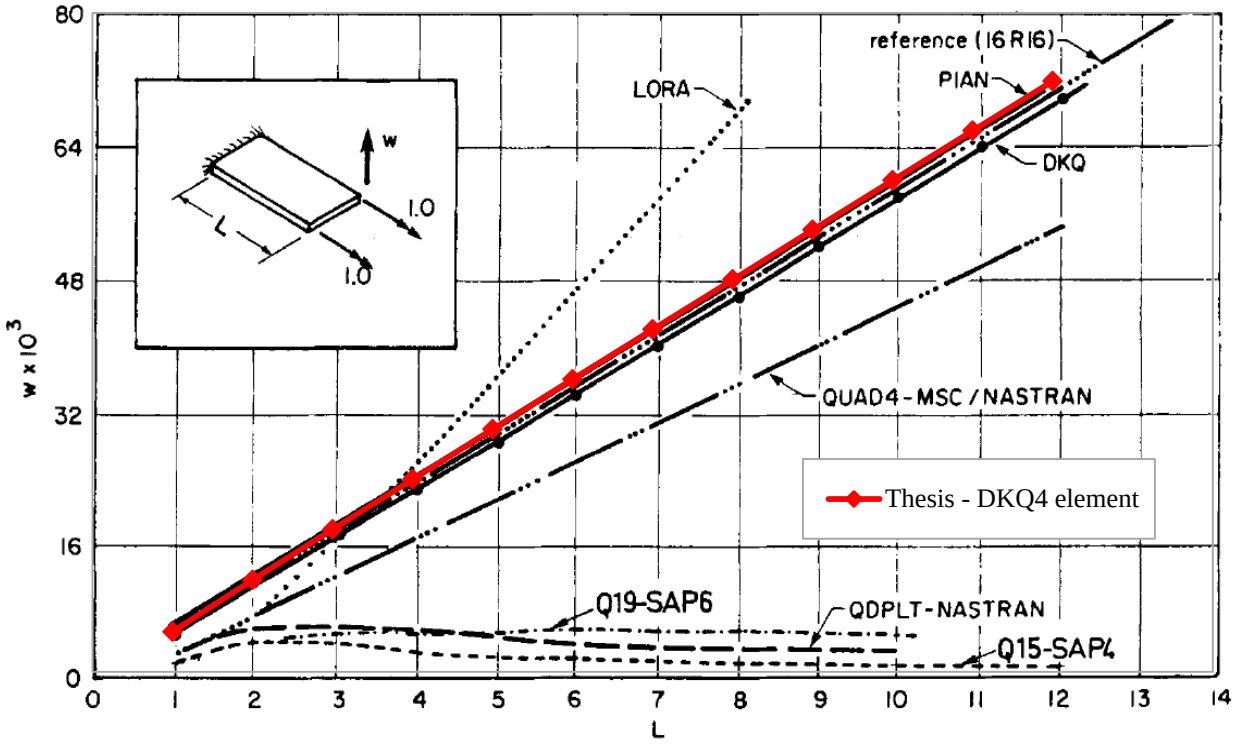

Figure 4.8: Elastic Cantilever Plate – Case 2. Batoz, J.-L., and Tahar, B. 1982, "Evaluation of a New Quadrilateral Thin Plate Bending Element." *International Journal for Numerical Methods in Engineering* 18 (11): 1655–77. Used under fair use, 2014.

4.7: Geometrically Nonlinear Elastic Wall

Two cases of an elastic cantilever wall were then analyzed using the proposed shell element. The purpose of these analyses was to validate the corotational formulation described in

Chapter 3 through comparison with benchmark results. The benchmark results were obtained by modeling the same structure in OpenSees (McKenna et al. 2000) using an included fiber beam model having a similar corotational approach.

4.7.1: Case 1 - Analysis of Vertical Cantilever Wall under Constant Vertical Loading and Increasing Horizontal Displacement

For the first case, an elastic cantilever wall was subjected at the tip with a constant vertical load and an increasing lateral, out-of-plane displacement. Geometric properties and loading conditions can be found in Figure 4.9. The modulus of elasticity was 5,000 ksi. The cantilever wall was discretized using ten shell elements along the height. Four different analyses were conducted; one where geometric nonlinearities were neglected and three with geometric nonlinearities considered. The three analyses where geometric nonlinearities were considered had different constant vertical loads of 10 kips, 40 kips and 100 kips.

For all four analyses, the lateral load at the top of the wall was plotted versus the lateral drift ratio at the top of the wall (Figure 4.10). The load-deformation response of each analysis is nearly identical to the load-deformation response of each benchmark result, providing evidence the corotational approach is working correctly in the proposed element. Also, as expected, the stiffness of the elastic wall decreases when going from neglecting geometric nonlinearities to considering them. Interestingly, at the highest vertical load case (100 kips), the structure requires a negative lateral force to keep it in static equilibrium.

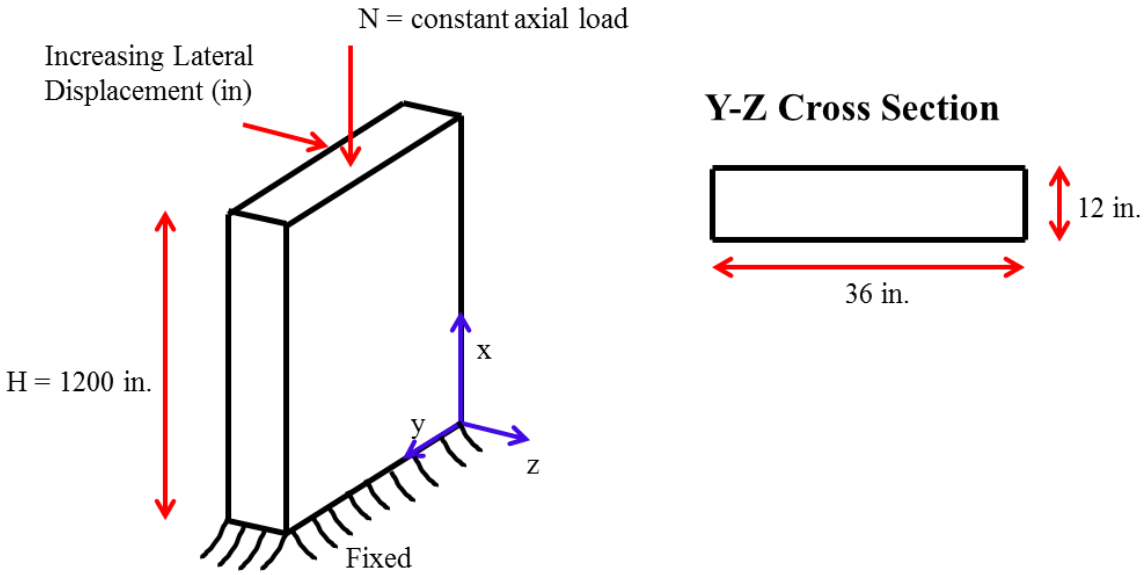

Figure 4.9: Case 1 - Geometric Properties and Loading

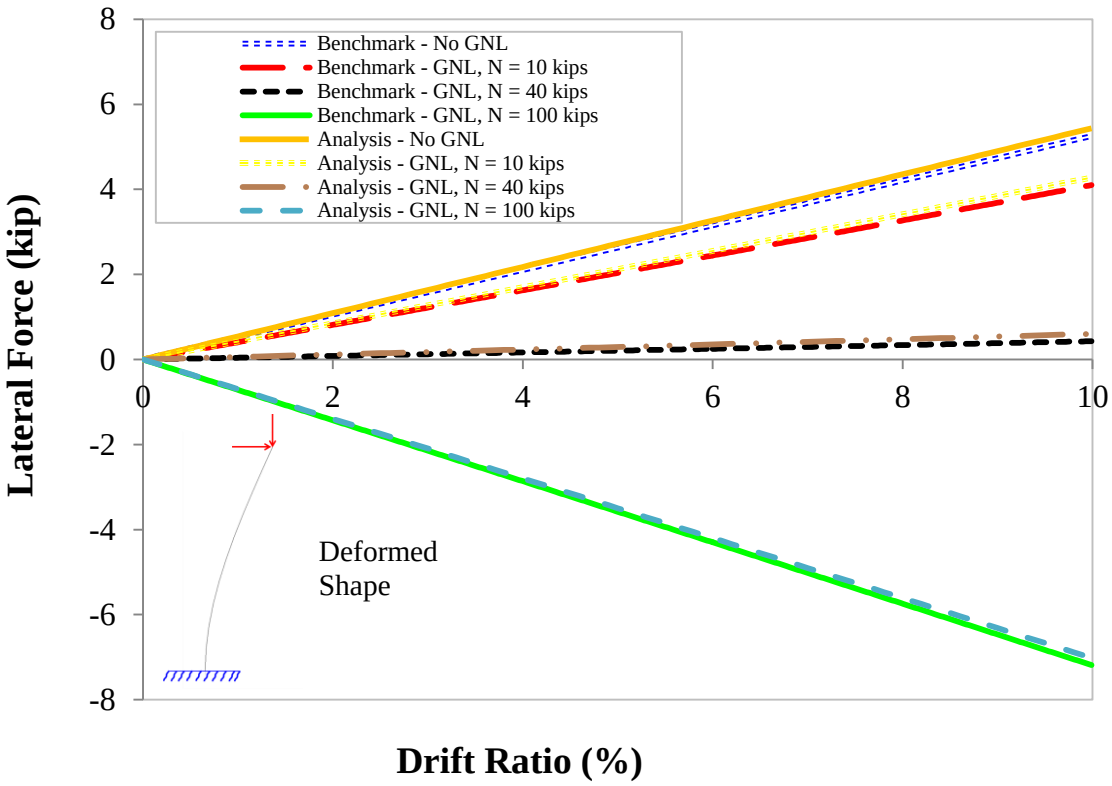

Figure 4.10: Case 1 - Lateral Load vs. Lateral Drift Ratio

4.7.2: Case 2 - Analysis of Wall with Increasing Eccentrically Applied Vertical Load

The second case is an extension of the first case with an additional cantilever shell element at the tip of the wall, so as to enable applying an eccentrically vertical load. Geometric nonlinearities were not considered for the additional cantilever element. The only applied loading was an imposed, increasing vertical displacement at the tip of the additional cantilever element. Geometric properties and loading conditions can be found in Figure 4.11. The additional cantilever element has a modulus of elasticity of 10,000 ksi. Two different analyses were conducted; one where geometric nonlinearities were neglected and one where geometric nonlinearities were considered for the wall. The vertical downward load versus the normalized vertical displacement at the tip of the additional element was plotted for each analysis and can be see in Figure 4.12.

As in Case 1, the load-deformation response of the Case 2 analyses match up exactly with the load-deformation response of the benchmark results. As expected, the load-deformation response when geometric nonlinearities are neglected remains linear with no loss of stiffness. Importantly, the load-deformation response where geometric nonlinearities are considered emulates the typical load-deformation response of a column with a load eccentricity. When geometric nonlinearities are considered, the elastic wall began to lose stiffness at low displacements and lost almost all of its stiffness at an approximate normalized vertical displacement of 0.4%. The load at this point was taken to be approximately 38.0 kips. This value can be compared to the Euler critical elastic buckling load (no load eccentricities or imperfections) found using the following equations.

$$P_{cr} = \frac{\pi^2 \times E \times I}{4 \times L^2} = \frac{\pi^2 \times 5{,}000\ ksi \times 5{,}184\ in.^4}{4 \times (1200\ in.)^2} = 44.41\ kips \quad \textbf{(72)}$$

$$where, E = Young's\ Modulus$$

$$I = Moment\ of\ Inertia = \frac{b \times h^3}{12} = \frac{36\ in. \times (12\ in.)^3}{12} = 5{,}184\ in.^4 \quad \textbf{(73)}$$

$$L = Height\ of\ Wall = 1200\ in.$$

As expected, and as shown in Fiqure 4.12, the approximate load when the wall loses most of its stiffness is smaller than the theoretical Euler critical elastic buckling load for the isolated cantilever wall, since the Euler solution does not include load eccentricities.

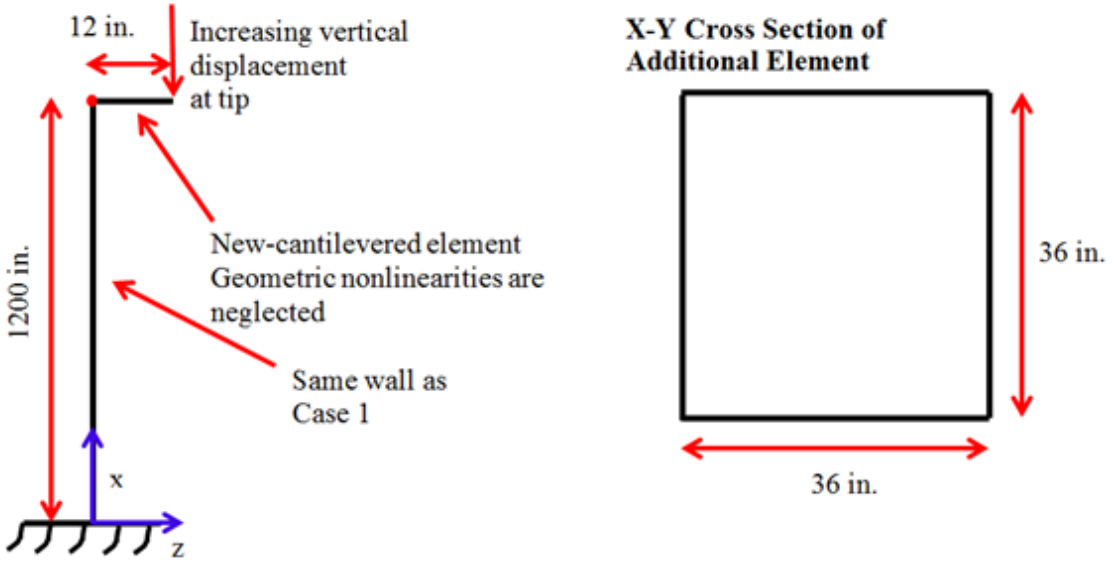

Figure 4.11: Case 2 Geometric Properties and Loading

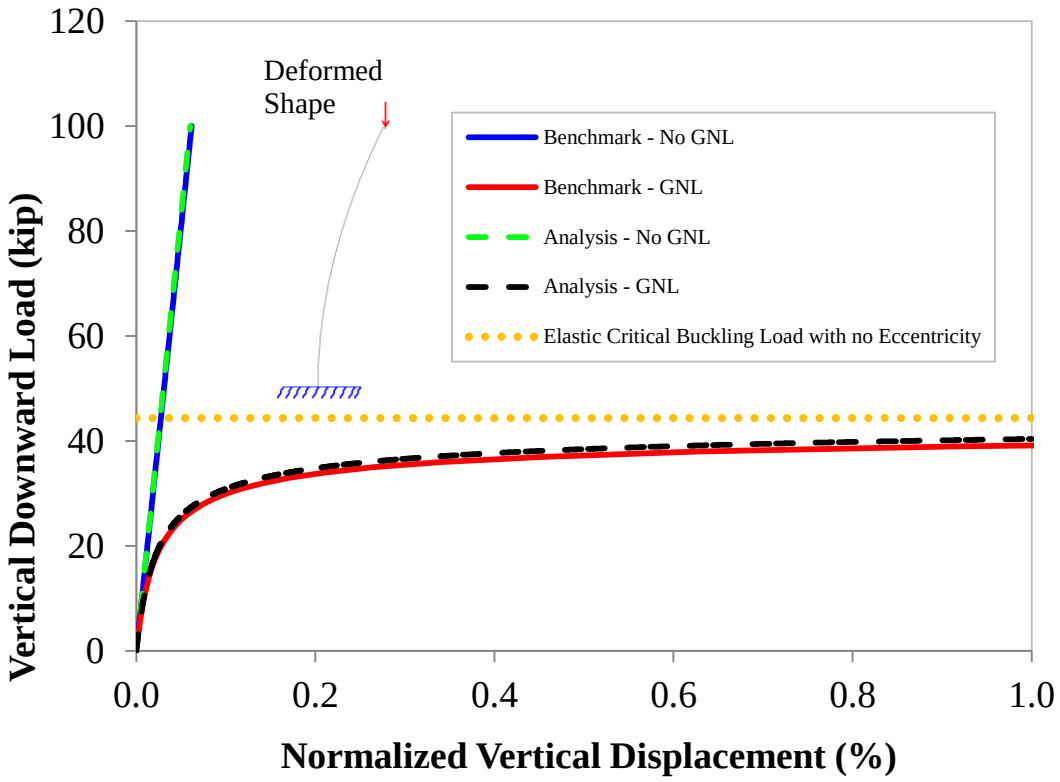

Figure 4.12: Case 2 – Vertical Downward Load vs. Normalized Vertical Displacement

4.8: Single Element subjected to Three-Dimensional Rigid Body Motion

The purpose of this analysis was to demonstrate the validity of the corotational approach. This was done by subjecting a single element to three-dimensional rigid body rotation. It is important to note if the element is subjected to only rigid body motion, the resulting internal forces should be negligible. The corotational approach subtracts out the rigid body displacements/rotations to obtain the deformational displacements/rotations. In this rigid body motion analysis, the total rotations/displacements correspond to only rigid body motion. The single element analysis setup can be seen in Figure 4.13 with pertinent geometric information.

The single element was subjected to three-dimensional rigid body rotation using the spatial rotational transformation matrix and process detailed in Zhang et al. (2003). For this

analysis, the element was subjected to a rotation (θ) of 0.2 radians about the unit vector (axis), which has equal projections of $(1/3)^{0.5}$ on all three axes (x, y and z). Table 4.1 shows the initial coordinates of each node. The first step was to find the coordinates of each node in the final configuration (Table 4.2) from the initial coordinates (Table 4.1) of each node using the spatial rotational transformation matrix. The units in this analysis are in kips and inches.

$$[XYZ_2]_i = [R] \times [XYZ_1]_i \quad \textbf{(74)}$$

$$[XYZ_2]_i = \text{Coordinates of a node i in the final configuration}$$

$$[XYZ_1]_i = \text{Coordinates of a node i in the original configuration}$$

Table 4.1: Initial Coordinates of each Node for Single Element subjected to Three-Dimensional Rigid Body Motion

	Node			
	1	2	3	4
X-Coordinate (in.)	-5.000	5.000	-5.000	5.000
Y-Coordinate (in.)	-5.000	-5.000	5.000	5.000
Z-Coordinate (in.)	0.000	0.000	0.000	0.000

Table 4.2: Final Coordinates of each Node for Single Element subjected to Three-Dimensional Rigid Body Motion

	Node			
	1	2	3	4
X-Coordinate (in.)	-4.395	5.475	-5.475	4.395
Y-Coordinate (in.)	-5.540	-4.330	4.330	5.540
Z-Coordinate (in.)	-0.065	-1.145	1.145	0.065

$$[R] = \begin{bmatrix} u_x^2 \times (1-\cos(\theta)) + \cos(\theta) & u_x \times u_y \times (1-\cos(\theta)) - u_z \times \sin(\theta) & u_x \times u_z \times (1-\cos(\theta)) + u_y \times \sin(\theta) \\ u_x \times u_y \times (1-\cos(\theta)) + u_z \times \sin(\theta) & u_y^2 \times (1-\cos(\theta)) + \cos(\theta) & u_y \times u_z \times (1-\cos(\theta)) - u_x \times \sin(\theta) \\ u_x \times u_z \times (1-\cos(\theta)) - u_y \times \sin(\theta) & u_y \times u_z \times (1-\cos(\theta)) + u_x \times \sin(\theta) & u_z^2 \times (1-\cos(\theta)) + \cos(\theta) \end{bmatrix} \quad \textbf{(75)}$$

$$[R] = \begin{bmatrix} 0.987 & -0.108 & 0.121 \\ 0.121 & 0.987 & -0.108 \\ -0.108 & 0.121 & 0.987 \end{bmatrix} \quad \textbf{(76)}$$

where $[R]$

$=$ Spatial Rotational Transformation Matrix for Three-Dimensional Rigid Body Rotation

$$u_x, u_y, u_z$$

$=$ Orthogonal projections on the x, y and z axes respectively of unit vector, $\mathbf{u}$, in which the three-dimensional body is rotating about $= \sqrt{\frac{1}{3}}$ for all three axes (x, y and z)

$\theta =$ Rotation of three-dimensional body about the unit vector, $\mathbf{u} = 0.2$ radians

The next step was to impose displacements at each node. These imposed displacements (Table 4.3) were determined by subtracting the original coordinate vector from the final coordinate vector at each node, as seen in the following equations.

$$[\Delta]_i = \text{ 3x1 Imposed Displacement Vector (in.) at each node i} = [XYZ_2]_i - [XYZ_1]_i \quad \textbf{(77)}$$

Table 4.3: Imposed Displacements at each Node for Single Element subjected to Three-Dimensional Rigid Body Motion

	Node			
	1	2	3	4
Δ_x (in.)	0.605	0.475	-0.475	-0.605
Δ_y (in.)	-0.540	0.670	-0.670	0.540
Δ_z (in.)	-0.065	-1.145	1.145	0.065

These displacements were gradually imposed at each node to enforce three-dimensional rigid body rotation. The nodal displacements were increased from zero to the specified values using 1,000 load steps. After the analysis was conducted, the internal moments were examined. As seen in Figures 4.14, 4.15 and 4.16, the internal moments across the entire element are

essentially zero. Since the element did not develop any internal moments, the element was successfully put into three-dimensional rigid body rotation and the corotational approach was validated.

The internal membrane forces were also compared to an analysis where geometric nonlinearities were not considered. The peak membrane forces N_{xx} when geometric nonlinearities were both considered and neglected were 0.42 kips and 26 kips respectively. The peak membrane forces N_{xy} when geometric nonlinearities were both considered and neglected were -0.16 kips and 8.67 kips respectively. The internal membrane forces for the analysis when geometric nonlinearities were considered were approximately zero, but not exactly zero. This may be due to the corotational approach being an approximate method, since it is second order accurate and its accuracy depends on the size of the load/step increments. The large increase in internal membrane forces between the two analyses (geometric nonlinearities considered and neglected) displays satisfactory and expected results. It is also important to note the final displacements and rotations of each node exactly matched the prescribed rigid body motion, when geometric nonlinearities were considered. These analyses verify the implemented corotational approach and the validity of the aforementioned transformation to enforce three-dimensional rigid body rotation.

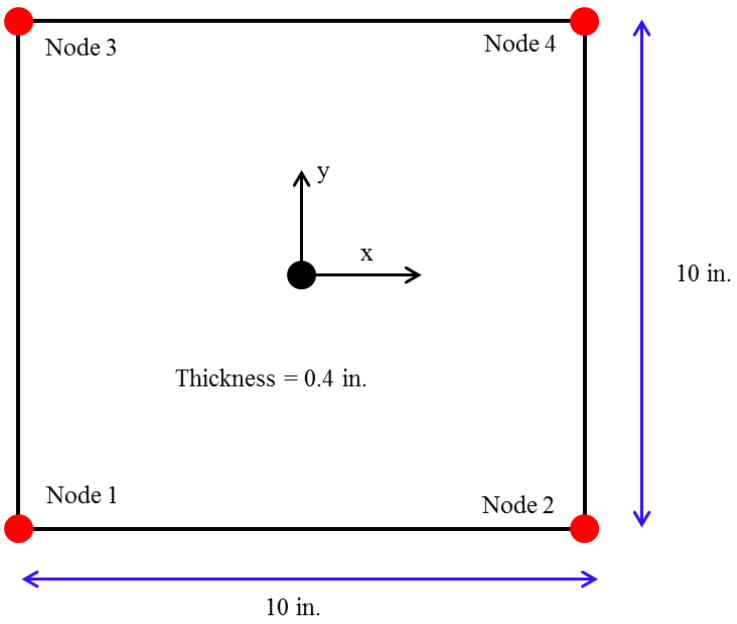

Figure 4.13: Single Element Analysis Setup in Original Configuration

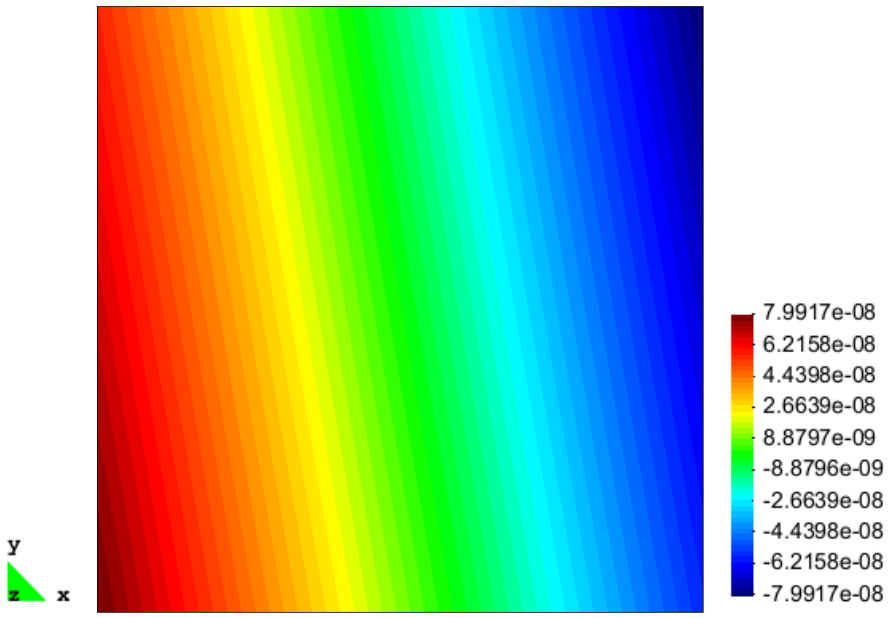

Figure 4.14: Contour Plot of Internal Moments M_{xx}

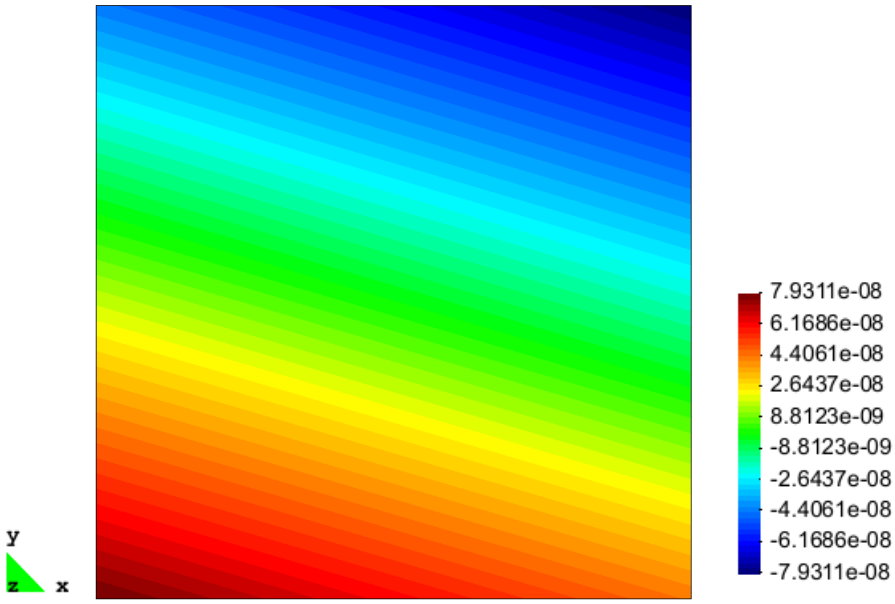

Figure 4.15: Contour Plot of Internal Moments M_{yy}

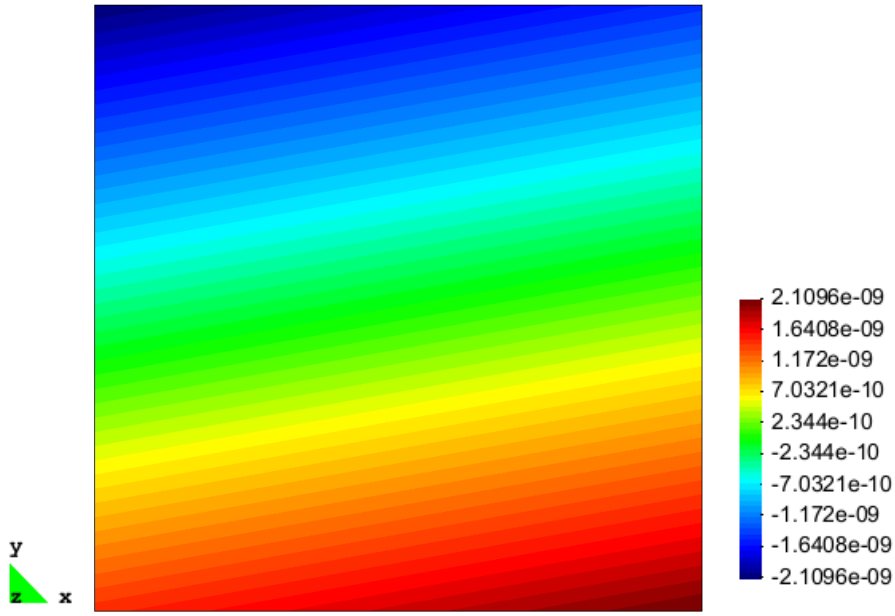

Figure 4.16: Contour Plot of Internal Moments M_{xy}

Chapter 5: Verification Analyses of Reinforced Concrete and Masonry Structures

5.1: Introduction

In this Chapter, the shell element formulations and material models are validated against experimental test results of reinforced concrete and reinforced masonry structures. These structures include an isolated reinforced concrete column, a seven-story reinforced concrete wall-slab building slice and a two-story reinforced masonry (fully-grouted) wall-slab building system. Material and/or geometric nonlinearities are considered in the analyses to correctly predict the response of these structures.

5.2: Reinforced Concrete Column

This section presents the analysis of an isolated reinforced concrete column subjected to a constant axial force and a static, lateral cylic displacement at the top of the column (Figure 5.1). The experiment of this isolated reinforced concrete column was conducted by Ang et al., as reported in Taylor et al. (1997). The column cross-sectional dimensions were 15.75 in. (400 mm) by 15.75 in. with 12.4 in. (315 mm) by 12.4 in. for the confined section. The length of the reinforced concrete column was 63 in. (1600 mm) as seen in Figure 5.1. The units in Figure 5.1 are in mm (25.4 mm = 1 in.). The steel reinforcement detailing can be see in Figure 5.1. The longitudinal steel reinforcement ratio was 0.0151. Additional transverse reinforcement was added to the base of the column to ensure there was ample ductility to form plastic hinges. The transverse steel reinforcement ratio in the plastic hinge region was 0.028. The concrete compressive strength was 3.42 ksi (23.6 MPa). The yield strength for longitudinal and transverse steel reinforcement was 62 ksi (427 MPa) and 47 ksi (320 MPa) respectively.

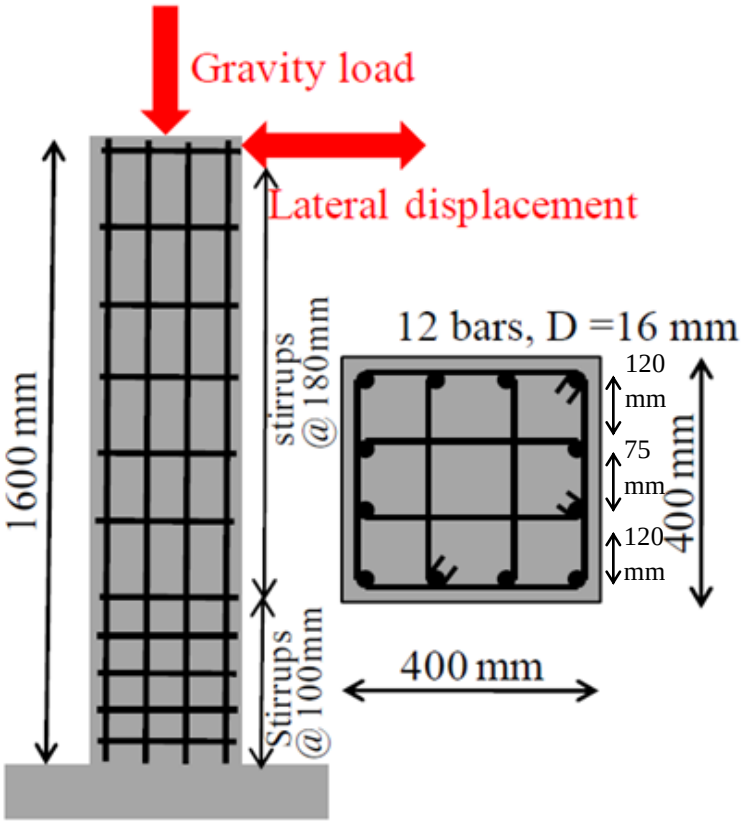

Figure 5.1: Reinforced Concrete Column tested by Ang et al. Taylor, A. W., Kuo, C., Wellenius, K., Chung, D. M. (1997), "A Summary of Cyclic Lateral Load Tests on Rectangular Reinforced Concrete Columns," *Report NISTIR 5984,* National Institute for Standards and Technology, Gaithesburg, Maryl., 101 pp. Used under fair use, 2014.

As seen in Figure 5.1, the base of the reinforced concrete column was fixed and the top was free. The constant axial load was 322 kips and the free end of the column was subjected to a static, cyclic lateral displacement. The primary purpose of analyzing this reinforced concrete column was to validate the shell element formulations and nonlinear material models against experimental results. The influence of utilizing an elasto-plastic versus Dodd-Restrepo material model for reinforcing steel was also studied. A set of simulations modeled the confined concrete core and the unconfined (cover) concrete while other simulations neglected the cover concrete. The differences and similarities between the results of the models were examined.

5.2.1: Description and Results of Full-width Finite Element Model using Smeared Reinforcement without Cover Concrete

The first finite element model (Figure 5.2) consisted of shell elements with dimensions of 3.94 in. by 3.5 in. This model assumed the whole column cross section was confined and replaced the softening portion of the concrete compression stress/strain curve by a constant line ignoring the sudden drop in strength at ultimate strain. The peak compressive strength of the concrete was increased following the Mander et al. (1988) model. In the Mander et al. (1988) confined concrete model, the softening portion of the stress/strain curve (with the aforementioned material parameters) is relatively flat until a strain of 0.014. Therefore, estimating the latter by a constant flat line would simplify the analysis and prevent strength degradation due to localization of compressive strain in certain elements. The adopted model was able to satifactorily predict the experimental data.

The steel reinforcement was smeared in both the longitudunal and transverse directions with Young's modulus set to 29,000 ksi and a linear strain hardening slope of 290 ksi. The steel yield strengths were the same as the specified strengths. The Young's modulus, compressive strength and tensile strength, respectively, of the concrete (again, all confined) were 3,440 ksi, 4.12 ksi and 0.44 ksi.

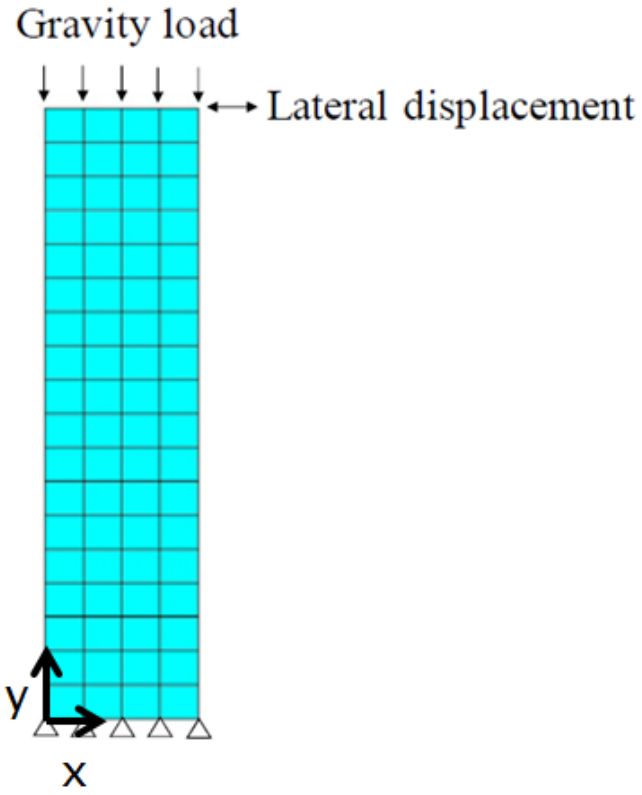

Figure 5.2: Initial Two-Dimensional Finite Element Model. Koutromanos, I. (2011), "Numerical Analysis of Masonry-Infilled Reinforced Concrete Frames Subjected to Seismic Loads and Experimental Evaluation of Retrofit Techniques." *Ph.D. Dissertation*, University of California, San Diego, La Jolla, CA, 355pp. Used under fair use, 2014.

Figure 5.3 shows a comparison of the lateral force vs. lateral displacement curves. There are three curves on this plot (Figure 5.3): the results from the experiment, the results from this specific model neglecting P-delta effects, and the results from this specific model including P-delta effects in the analysis. The P-delta effects were incoroparated in the analysis by adding an additional horizontal force to the free end of the column. The applied horizontal force was equal to the constant axial load (322 kips) multiplied by the imposed lateral displacement at the top row of nodes divided by the height of the column (63 in.).

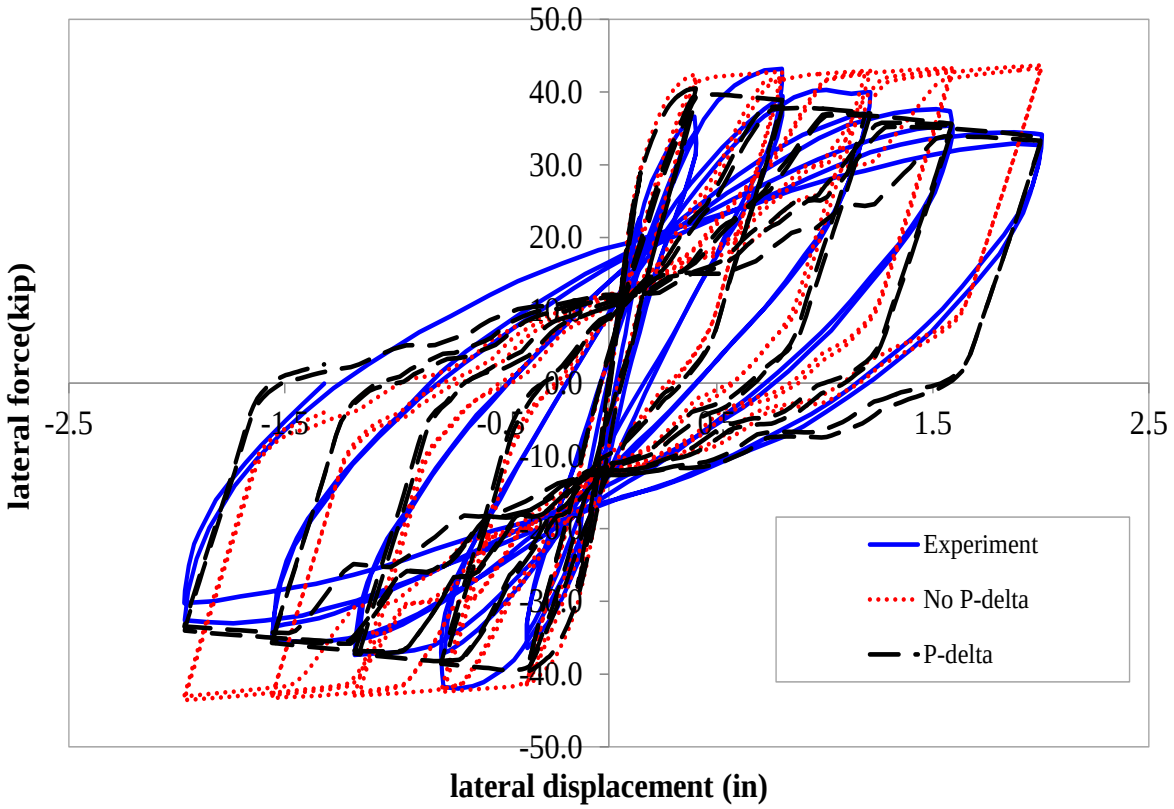

Figure 5.3: Lateral Force vs. Lateral Displacement using Smeared Reinforcement

As seen in Figure 5.3, this finite element model was able to predict the load-displacement response of the actual column when P-delta effects were both included and neglected. Both of the analyses overestimated the strength at very small displacements (less than 0.25 in.) because all of the concrete was assumed to be confined. The analysis that did not include P-delta effects slightly overestimated the strength of the column (especially at larger displacements) and did not reproduce strength degradation due to the cyclic effect. The analysis that included P-delta effects slightly underestimated the lateral strength at lateral displacements between 0.5 in. and 1.0 in., but accurately reproduced strength degradation due to the cyclic effect at the larger lateral displacements.

5.2.2: Description and Results of Full-width Finite Element Model with Elasto-Plastic Steel Truss Elements without Cover Concrete

For the next analysis, the steel reinforcement was modeled using steel truss elements with an elasto-plastic (with linear strain hardening) material model. A Young's modulus of 29,000 ksi and plastic modulus of 290 ksi (same as previous model) was used. Reinforcement ratios were kept constant. The distribution of longitudinal steel truss elements was consistent with the actual reinforced concrete column (Figure 5.1). A mesh similar to the previous simulation was used and the entire column was again assumed to be confined. The purpose of this analysis was to determine how much increased strength was developed when all of the concrete is assumed to be confined and the reinforcing steel is modeled as truss elements instead of smeared reinforcement. Figure 5.4 displays the hysteric response of the actual reinforced column as well as the analytical results when P-delta effects were both included and neglected.

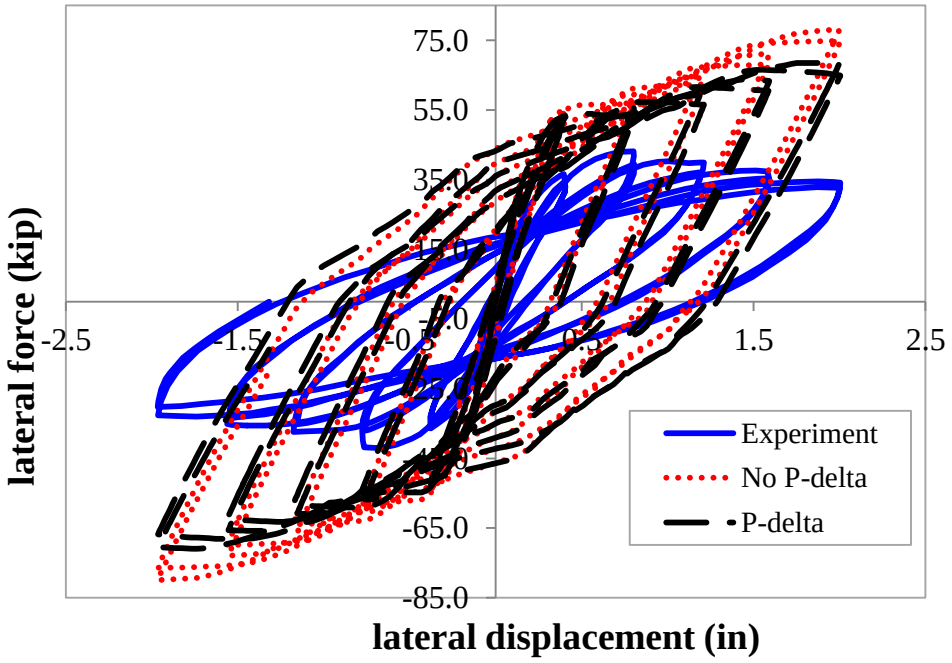

Figure 5.4: Lateral Force vs. Lateral Displacement using Elasto-Plastic Steel Truss Elements and Full-Width Cross Section

This model did not properly predict the experimental lateral force vs. lateral displacement hysteretic response. As expected, the strength was greatly overestimated because the entire cross section of the column was modeled as confined, and also because of how the longitudinal steel reinforcing was modeled. Most of the longitudinal reinforcing steel was located at the outer edges of the column where large strains occurred but the steel strength did not degrade due to the material model being elasto-plastic with linear hardening. This phenomenon is examined in further detail with the following analysis. This simulation also did not predict the degradation in strength due to the cyclic effect at higher lateral displacements. The strength actually increased after successive load cycles and higher lateral displacements.

5.2.3: Description and Results of Reduced-width Finite Element Model using Elasto-Plastic Steel Truss Elements without Cover Concrete

In this analysis, the model utilized a reduced overall column width to better represent the confined concrete width of the actual reinforced concrete column. The unconfined concrete was not accounted for in this analysis. The mesh cross-sectional dimensions were changed from 15.75 in. x 15.75 in. to 12.4 in. x 12.4 in. The same material properties were used for the confined concrete (entire mesh) and the reinforcing steel truss elements (elasto-plastic with linearly increasing strain hardening). The same amount of steel reinforcement was used as the previous analysis. Figure 5.5 represents the lateral force vs. lateral displacement hysteretic curves when P-delta effects are both included and neglected.

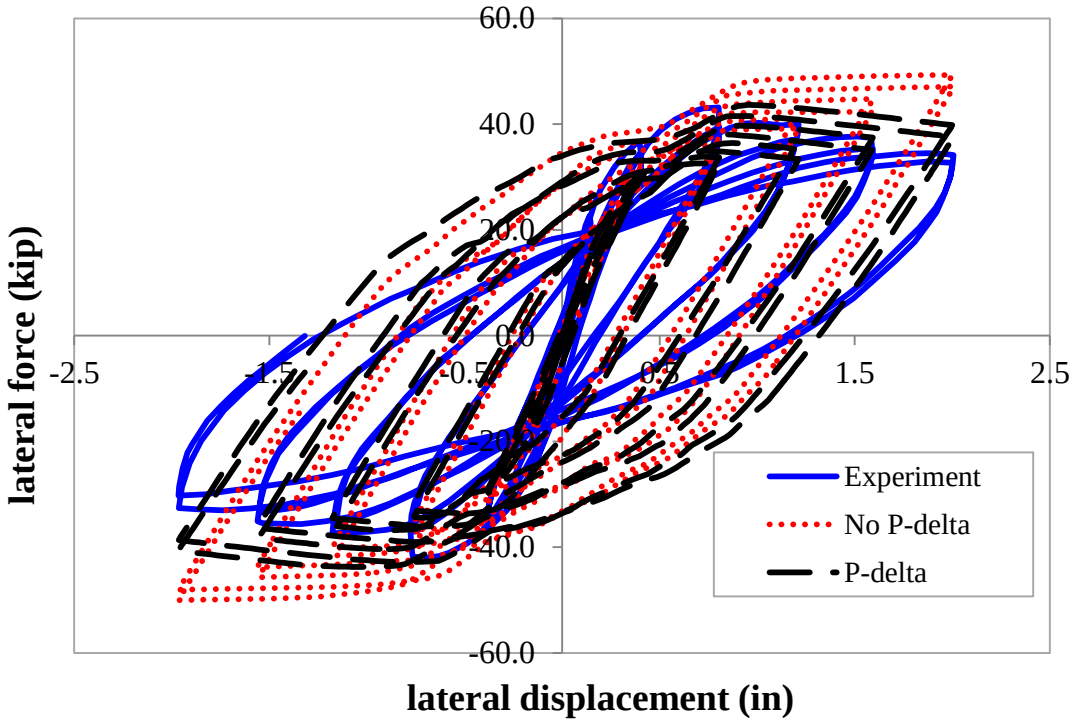

Figure 5.5: Lateral Force vs. Lateral Displacement using Elasto-Plastic Steel Truss Elements and Reduced-Width Cross Section

This analytical model provided an accurate prediction of the actual reinforced concrete column response. As expected, the lateral strength for this model was much smaller than the previous model because only the confined concrete area was used. The lateral strength was underestimated at smaller lateral displacements (< 0.25 in.) because only the confined concrete area was modeled rather than the gross concrete area (confined and unconfined/cover concrete). The strength at higher displacements was slightly overestimated because of the slightly crude material model for the steel truss elements (elasto-plastic with linearly increasing strain hardening) and the majority of the longitudinal reinforcing steel being placed at the outside edges of the column. During larger displacements, most of the strain in the column localized near the edges of the base. Since the steel truss elements were elasto-plastic with linearly increasing strain hardening and the majority of the longitudinal steel was located at the outer edges, the column's

strength did not degrade and thus the model overestimated the strength at higher displacements. This phenomenon is shown in the Figure 5.6, which is a contour plot of the maximum principal strain at the final load step (lateral displacement = -1.3 in.). Bond-slip was not accounted for in this model as well and this may have caused the differences in the unloading/reloading curves between the experimental and analytical results.

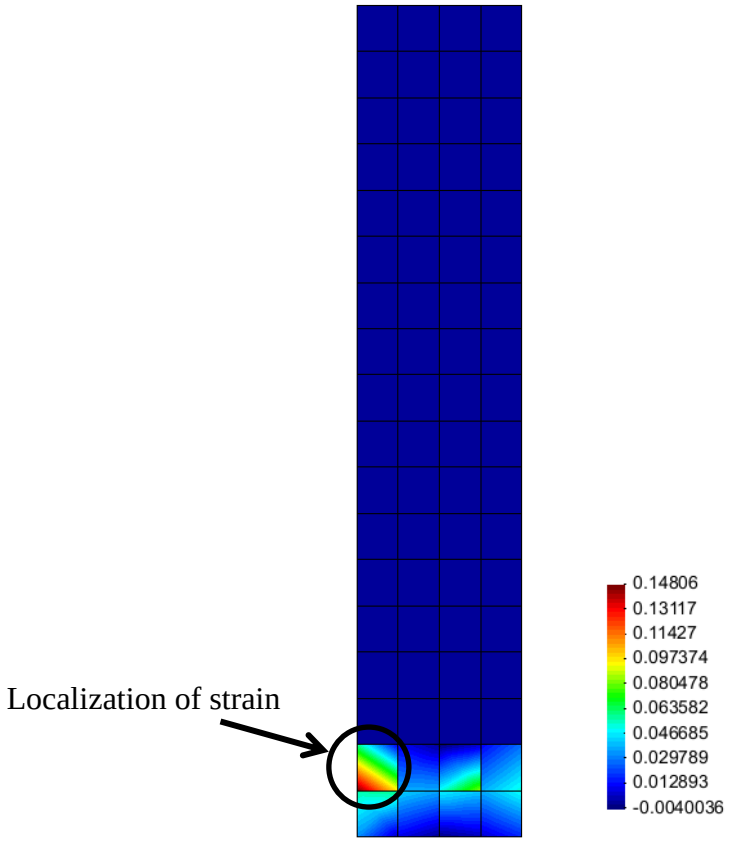

Figure 5.6: Maximum Principal Strain Contour Plot at Final Load Step

5.2.4: Description and Results of Full-width Finite Element Model using Elasto-Plastic Steel Truss Elements with Cover Concrete

For the next finite element model of the isolated reinforced concrete column, the same finite element mesh was used as the previous analysis but with cover elements (unconfined

concrete) added to the outer edges of the column as seen in Figure 5.7. The same material models were used for the confined concrete and the reinforcing steel (both transverse and longitudinal). An additional material model was implemented to account for the unconfined concrete or cover. The compressive strength, 3.42 ksi, from Taylor et al. (1997) was used for the cover (concrete) elements. The unconfined concrete was assumed to reach its peak compressive strength at a strain of approximately 0.0021 and crush at a strain of approximately 0.0024. At the point when the cover concrete crushes, the compressive strength of the unconfined concrete decreases exponentially. The purpose of this analysis was to determine how implementing the cover of the reinforced concrete column affected the accuracy of the model.

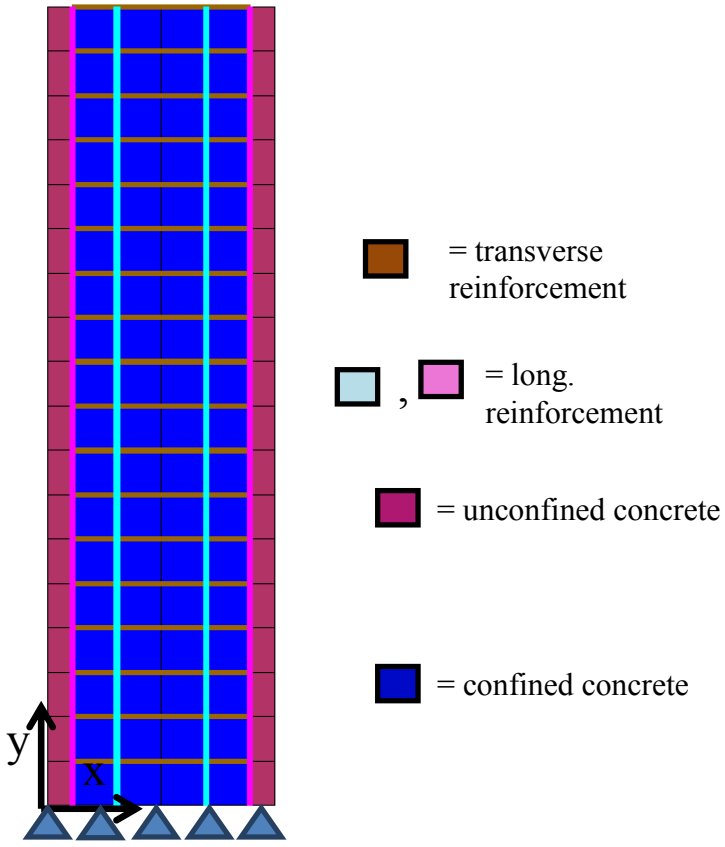

Figure 5.7: Finite Element Mesh with Confined and Unconfined Concrete using Steel Truss Elements

As seen in Figure 5.8, the analytical model was able to satisfactorily reproduce the actual hysteretic load-displacement response. The lateral strength of the model was slightly increased and was more accurate at smaller lateral displacements when compared to the confined concrete (reduced) width model that does not include cover elements. This was expected as the area of concrete was increased from 154 in.^{2} (confined area of the column) to 248 in.^{2} (gross area of the column). Including the cover elements did not however increase the lateral strength of the finite element model at higher lateral displacements when compared with the confined width model (no cover elements).

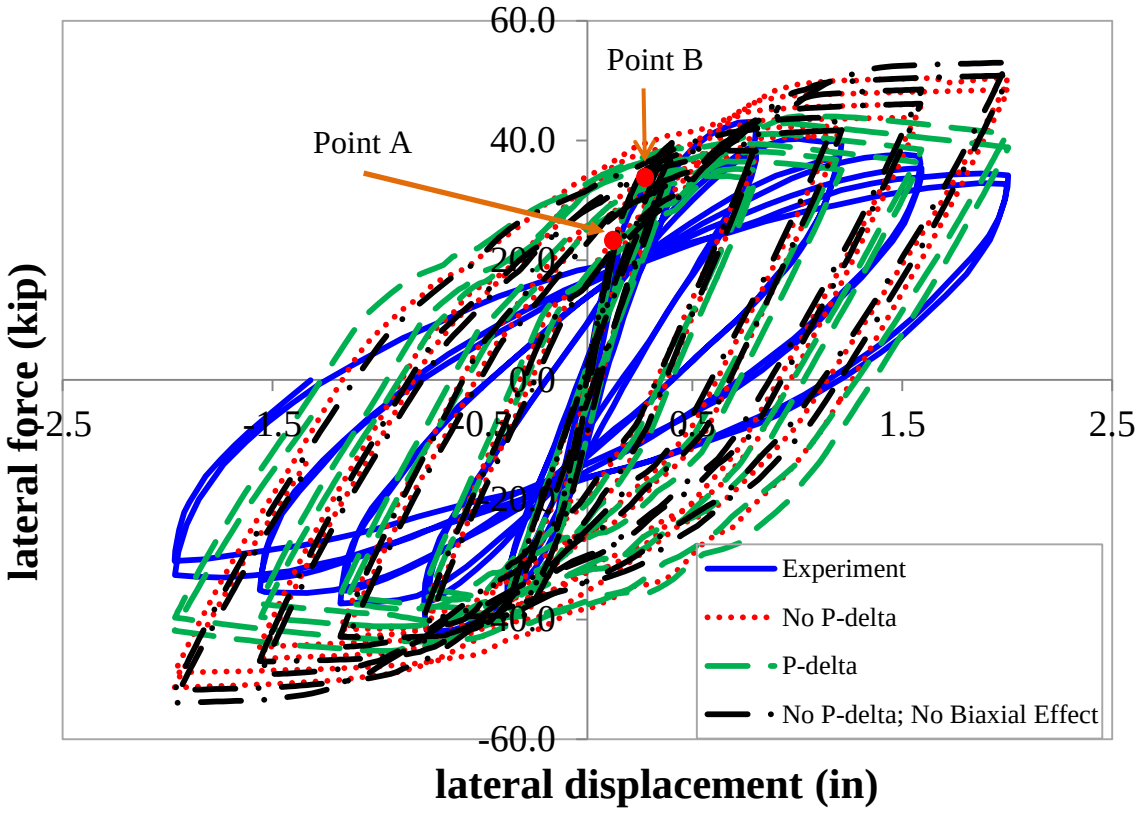

Figure 5.8: Lateral Force vs. Lateral Displacement using Elasto-Plastic Steel Truss Elements and Full-Width with Cover

As seen in Figures 5.8 and 5.9, the cover concrete at the base of the column began to lose most of its compressive strength at relatively low displacements. Point A represents the point when the cover concrete has reached its peak compressive strength (3.44 ksi). This occurred at a strain of 0.0021 and as seen in Figure 5.9(a) the minimum principal strain at Point A (0.00214) exceeded that value. Point B represents the point when the cover concrete at the base of the column was crushed and the compressive strength began to decrease exponentially. The cover concrete began to crush at a strain of 0.0024 and as seen in Figure 5.9(b) the minimum principal strain at Point B (0.003) exceeds this value. Since the cover concrete began to crush (and exponentially lose its compressive strength) at relatively low lateral displacements (0.24 in.), it may have not been necessary to model the cover/unconfined concrete.

Another purpose of this analysis was to examine how neglecting the biaxial effect altered the analytical results. The biaxial effect accounts for the reduction in peak compressive strength of cracked concrete due to it being in a state of biaxial stress. This additional analysis case neglected P-delta effects and the analytical results are shown in Figure 5.8. As expected, the model with the biaxial effect neglected overestimated the peak strength values more than the analysis when the biaxial effect was incorporated.

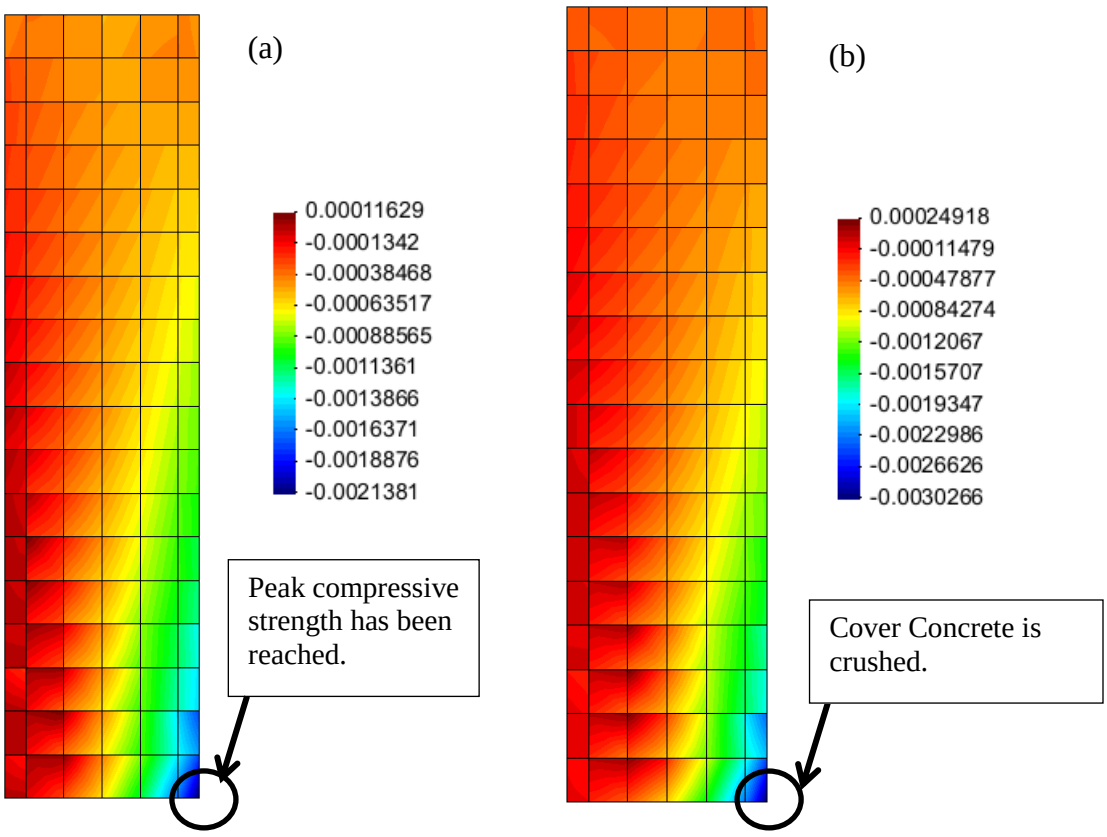

Figure 5.9: Minimum Principal Strain Contour Plot when (a) Peak Compressive Strength has been reached (b) Cover Concrete has begun to crush

5.2.5: Description and Results of Full-width Finite Element Model using Dodd-Restrepo Steel Truss Elements with Cover Concrete

The final analysis to model this reinforced concrete column used the Dodd-Restrepo material model for the steel truss elements, instead of assuming the steel material model was elasto-plastic with linearly increasing strain hardening. The Dodd-Restrepo model offers more robust and accurate cyclic and monotonic constitutive laws for reinforcing steel. The Dodd-Restrepo model is able to capture the Bauschinger Effect and has a clear, defined yield plateau and strain hardening region. Table 5.1 details the material parameters for the longitudinal and

transverse reinforcing steel from this analysis associated with using the Dodd-Restrepo material model.

Table 5.1: Dodd-Restrepo Steel Material Properties for the Analysis of a Reinforced Concrete Column

Material Properties	Longitudinal Steel	Transverse Steel
Yield Strength, Fy (ksi) =	62.0	47.0
Ultimate Strength, Fu (ksi) =	100.0	85.0
Ultimate Strain, εu =	0.15	0.19
Final Strain of Yield Plateau, εsh =	0.01	0.01
Intermediate Strain Value, εsh1 =	0.02	0.03
Intermediate Stress Value, σsh1 (ksi) =	75.0	60.0
Young's modulus (ksi) =	29000.0	29000.0

This analytical model was subjected to the same loading and boundary conditions as the previous analyses. Figure 5.10 shows the lateral force vs. lateral displacement plot with and without the consideration of P-delta effects. It is important to note the biaxial effect was considered for this model.

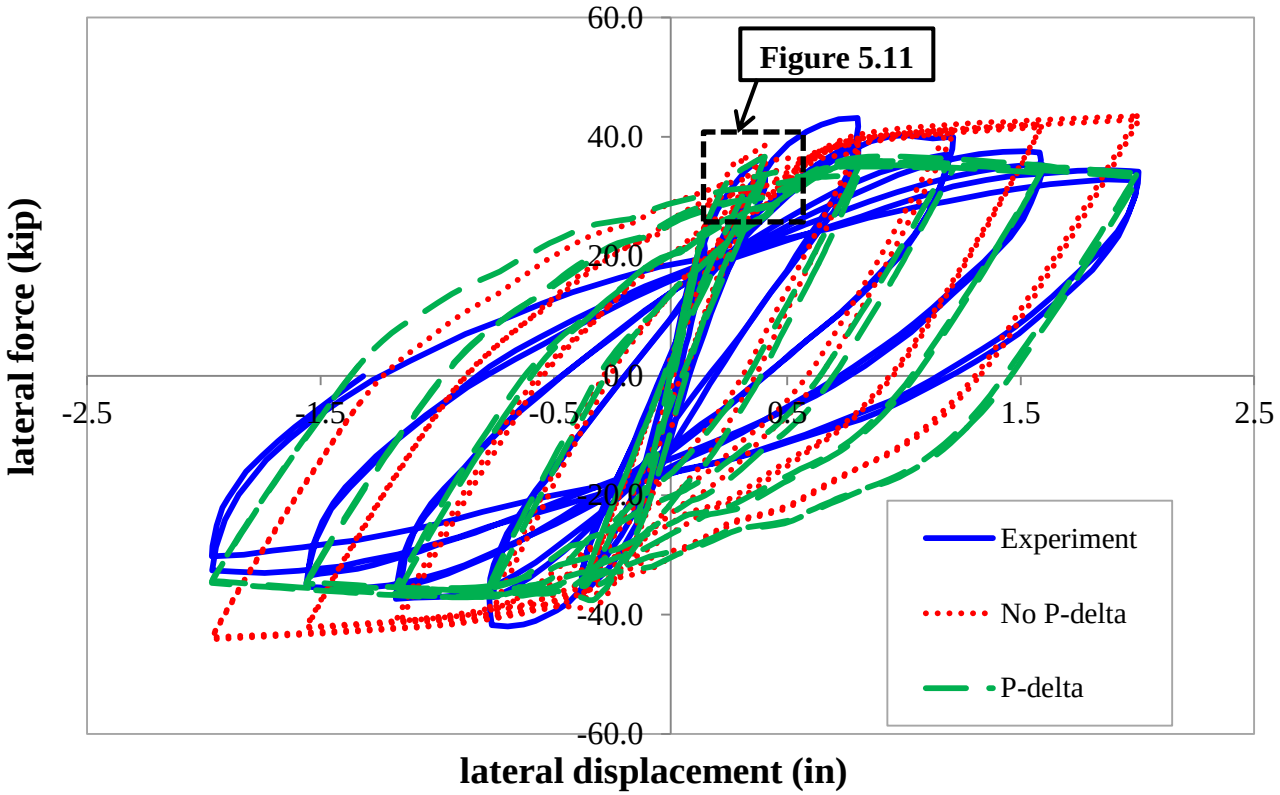

Figure 5.10: Lateral Force vs. Lateral Displacement Plot with Dodd-Restrepo Steel Truss Elements

As seen in Figure 5.10, the analytical model provided satisfactory results when compared to the experimental lateral force vs. lateral displacement hysteretic response. This model adequately captured the degradation of peak strength due to repeated unloading and reloading. Once again, the lateral strength at relatively small lateral displacements was correctly predicted by the analytical model, especially when implementing P-delta effects. Figure 5.11 provides a zoomed-in lateral force vs. lateral displacement plot of when the first cover concrete element begins to crush and depicts the accuracy of the model in predicting the strength degradation of the reinforced concrete column. Figure 5.11 also shows how closely the analytical lateral force-displacement curves were compared to the experimental results at relatively low lateral displacements, particularly for the analysis that included P-delta effects.

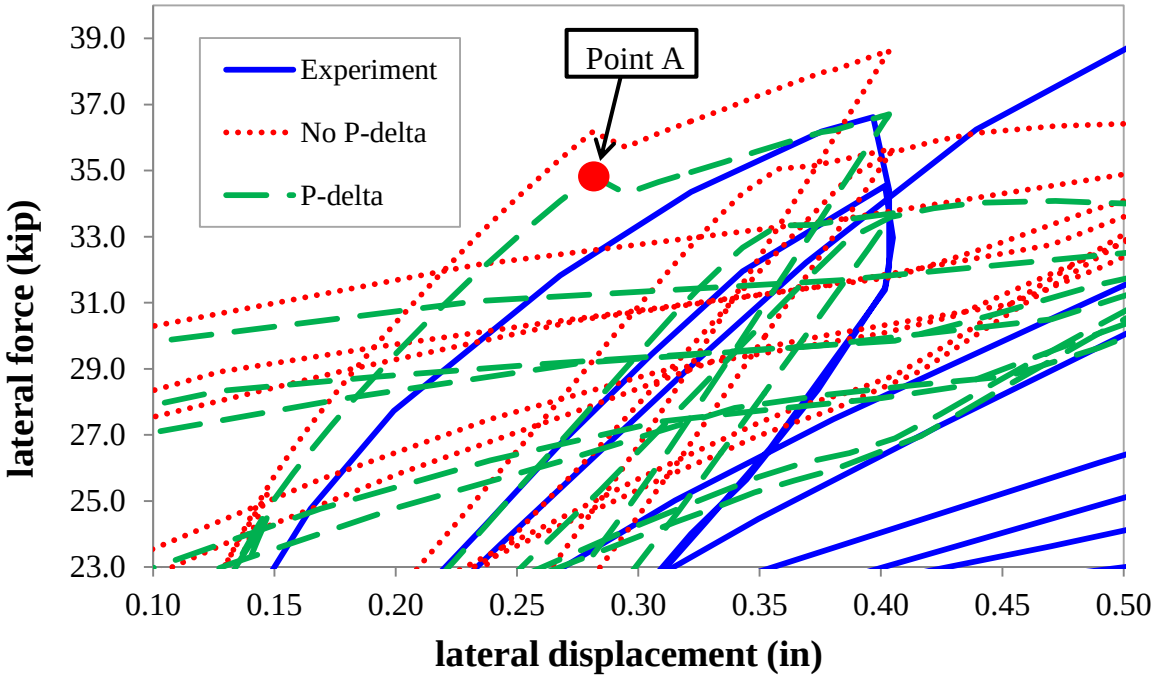

Figure 5.11: Lateral Force vs. Lateral Displacement Plot when Cover Concrete has begun to crush

The first cover concrete element (unconfined concrete) is crushed at Point A on the lateral load vs. lateral displacement plot (Figure 5.11). When P-delta effects were included, the lateral strength was slightly overestimated before concrete cover elements began crushing. After crushing began, the stiffness of the model reduced and the model more accurately represented the experimental column lateral strength for the remainder of the load cycle. Figure 5.12 shows the contour plot of the minimum principal strain at Point A. It can be seen that the base cover concrete elements incurred strains up to 0.003, which were greater than the strain in which the unconfined concrete is considered crushed (0.0024).

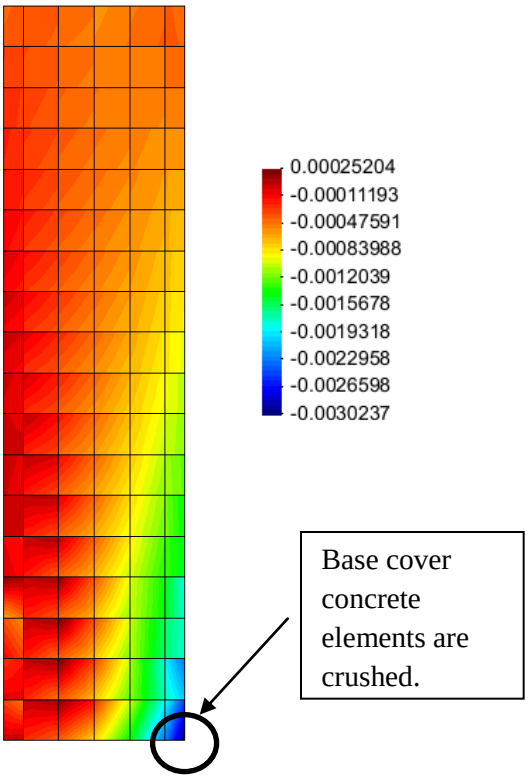

Figure 5.12: Minimum Principal Strain Contour Plot at Point A

5.2.6: Comparison of Full-width Finite Element Model using Elasto-Plastic Steel Truss Elements and Full-width Finite Element Model using Dodd-Restrepo Steel Truss Elements

Using the results of the prior analyses, this section compares the hysteretic response of the full-width finite element model (including cover concrete elements) using steel truss elements with an elasto-plastic (with linear strain hardening) material model vs. the Dodd-Restrepo material model. The lateral load vs. lateral displacement curves for both models (along with the experimental results) are plotted in Figure 5.13. The model that utilized the Dodd-Restrepo material model for reinforcing steel more accurately reproduced the actual hysteretic response of the reinforced concrete column. The analysis, which used the Dodd-Restrepo

material model, also more accurately reproduced the loss of strength due to repeated unloading and reloading. Conversely, the lateral strength of the model that utilized the elasto-plastic material model for reinforcing steel actually increased after repeated loading cycles. Neither of the models were able to capture the unloading/reloading response of the specimen. This may have been caused by neglecting bond-slip between steel and concrete and/or the initial stiffness unloading/reloading rule for concrete under compression. The actual column stiffness during unloading/reloading degraded after each subsequent cycle, and this was not captured by the initial stiffness unloading/reloading rule.

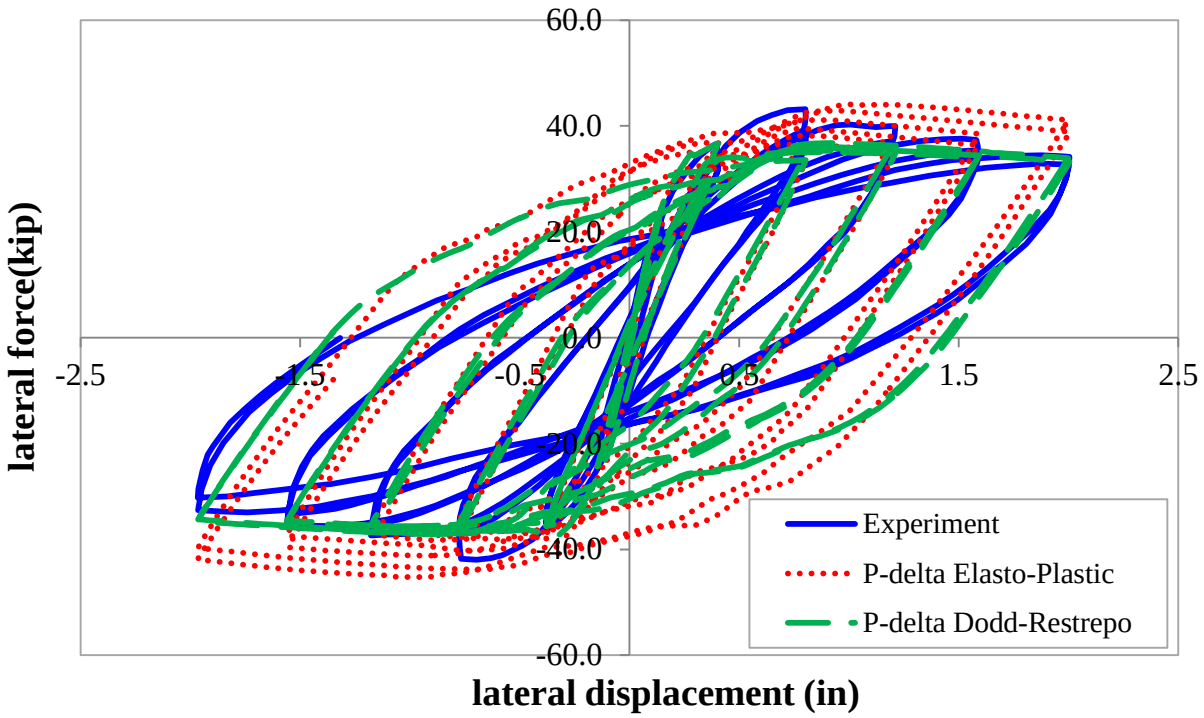

Figure 5.13: Lateral Load vs. Lateral Displacement Plot when using Dodd-Restrepo Steel Truss Elements or Elasto-Plastic Steel Truss Elements

5.3: Seven-story Reinforced Concrete Wall-Slab Building Slice

To validate the shell element formulations and material models for wall systems, analyses were conducted for a seven-story reinforced concrete specimen tested by Panagiotou et al. (2007)

at the University of California San Diego. The specimen was tested on an outdoor shake table. Figure 5.14 displays the seven-story reinforced concrete wall specimen. The wall structure consisted of a web wall and a perpendicular flange wall in a T-shape. The web wall was counted on to resist the majority of the lateral loading. A precast/post-tensioned segment wall was included to help provide additional lateral and torsional stability to the web wall. The precast segment wall was pin connected to each slab using horizontal diaphragm steel trusses. The gravity columns were made of strong steel pipes and filled with high performance grout. These columns were meant to resist some of the gravity load from the reinforced concrete slabs and remained elastic during the experimental tests. The slab between the web wall and the flange wall was designed as a slotted connection as seen in Figure 5.15. The purpose of the slotted connection was to provide a near pinned connection between the web wall and flange wall (Panagiotou and Restrepo 2010). This allowed for the transfer of in-plane forces but reduced out-of-plane moments and shear forces (Panagiotou and Restrepo 2010).

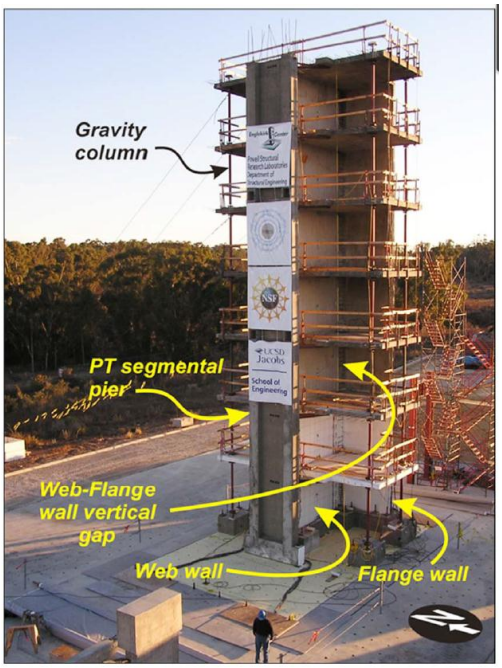

Figure 5.14: Picture of Seven-story Reinforced Concrete Building Slice. Panagiotou, M., and Restrepo, J. (2010), "Displacement-Based Method of Analysis for Regular Reinforced-Concrete Wall Buildings: Application to a Full-Scale 7-Story Building Slice Tested at UC–San Diego." *Journal of Structural Engineering* 137 (6): 677–90. Used under fair use, 2014.

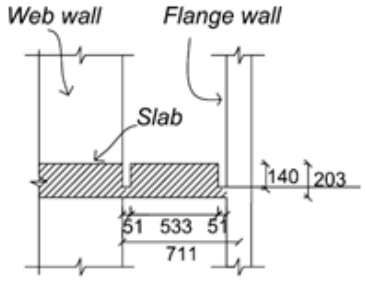

Figure 5.15: Slotted Connection. Panagiotou, M., and Restrepo, J. (2010), "Displacement-Based Method of Analysis for Regular Reinforced-Concrete Wall Buildings: Application to a Full-Scale 7-Story Building Slice Tested at UC–San Diego." *Journal of Structural Engineering* 137 (6): 677–90. Used under fair use, 2014.

A plan view of the web wall and flange wall steel reinforcement details can be seen in Figure 5.16. An elevation view of the steel reinforcement in the first two levels of the web wall can be seen in Figure 5.17. The units in both of these figures are in mm. (1 inch = 25.4 mm.). As seen in Figure 5.16, the first and seventh levels had the same reinforcement details and the

second through sixth levels had the same reinforcement details. The longitudinal and transverse steel reinforcement ratios, respectively, for the first and seventh levels were 0.66% and 0.31%. The longitudinal and transverse steel reinforcement ratios, respectively, for the second through sixth levels were 0.81% and 0.41%. It should be noted that the web wall and flange wall had a greater thickness on levels one and seven.

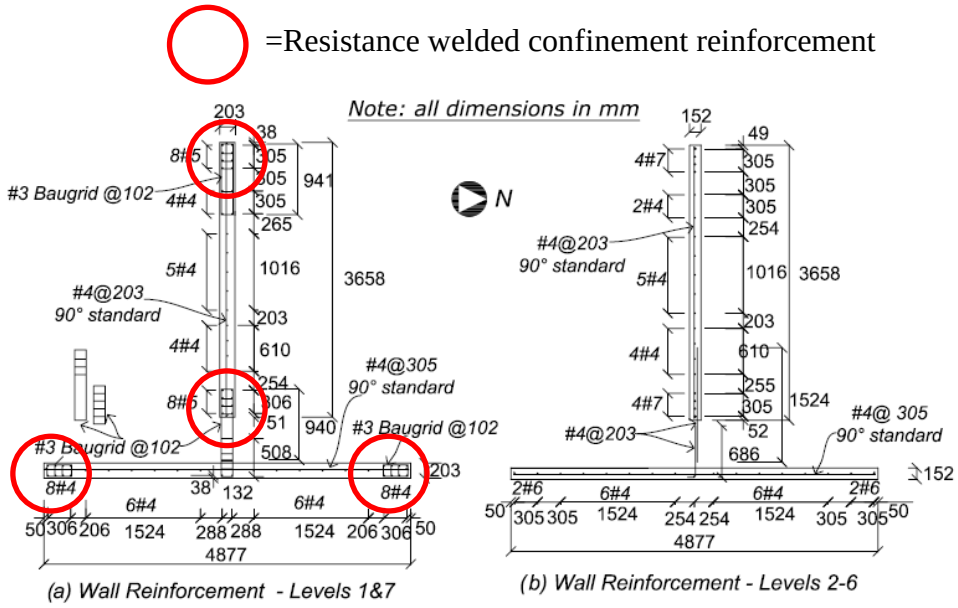

Fig. 7. Building—Plan view of reinforcement

Figure 5.16: Plan View of Web and Flange Wall Reinforcement. Panagiotou, M., and Restrepo, J. (2010), "Displacement-Based Method of Analysis for Regular Reinforced-Concrete Wall Buildings: Application to a Full-Scale 7-Story Building Slice Tested at UC–San Diego." *Journal of Structural Engineering* 137 (6): 677–90. Used under fair use, 2014.

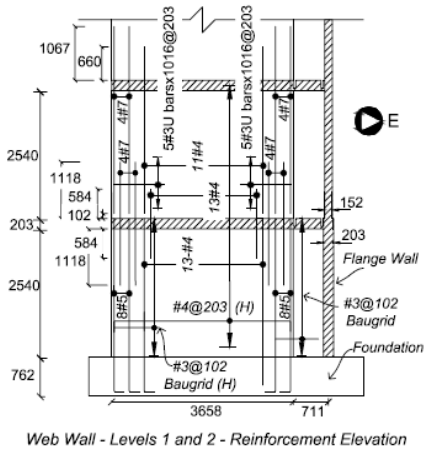

Fig. 8. Web wall elevation Levels 1 and 2 showing longitudinal and transverse reinforcement

Figure 5.17: Elevation View of Web Wall Reinforcement for Levels 1 and 2. Panagiotou, M., and Restrepo, J. (2010), "Displacement-Based Method of Analysis for Regular Reinforced-Concrete Wall Buildings: Application to a Full-Scale 7-Story Building Slice Tested at UC–San Diego." ***Journal of Structural Engineering*** **137 (6): 677–90. Used under fair use, 2014.**

Resistance welded confinement reinforcement was used in the outer regions of the web and flange walls at the first and seventh levels as seen in Figure 5.16. This type of reinforcement was intended to confine the concrete, which in turn provided ample ductility to form plastic hinges in these locations. More information on the resistance welded confinement reinforcement can be found in Panagiotou et al. (2007). The rest of the transverse and longitudinal reinforcement consisted of mild steel reinforcing bars (not resistance welded). These bars are termed mild steel reinforcing bars for the remainder of the study. Levels two through six did not have any confined concrete regions and used only mild steel reinforcing bars (for both transverse and longitudinal reinforcement). The compressive strength of the concrete was 5.5 ksi, the yield strength of the mild steel reinforcement was 66.0 ksi and the yield strength of the resistance welded confinement reinforcement was 75.1 ksi.

The seven-story reinforced concrete wall-slab building slice was subjected to four different earthquake ground motions (Figure 5.18) in the direction of the web wall. The first three ground motions were recordings from the 1971 San Fernando earthquake while the fourth ground motion was a recording from the 1994 Northridge earthquake. All four of the applied ground motions lasted 30 seconds. Each subsequent ground motion was slightly greater in magnitude to avoid sudden collapse/failure. The base shear/moment and lateral drift were measured using experimental equipment. Further detail on the instrumentation used in the experimentation of this seven-story reinforced concrete wall-slab building slice can be found in Panagiotou et al. (2007).

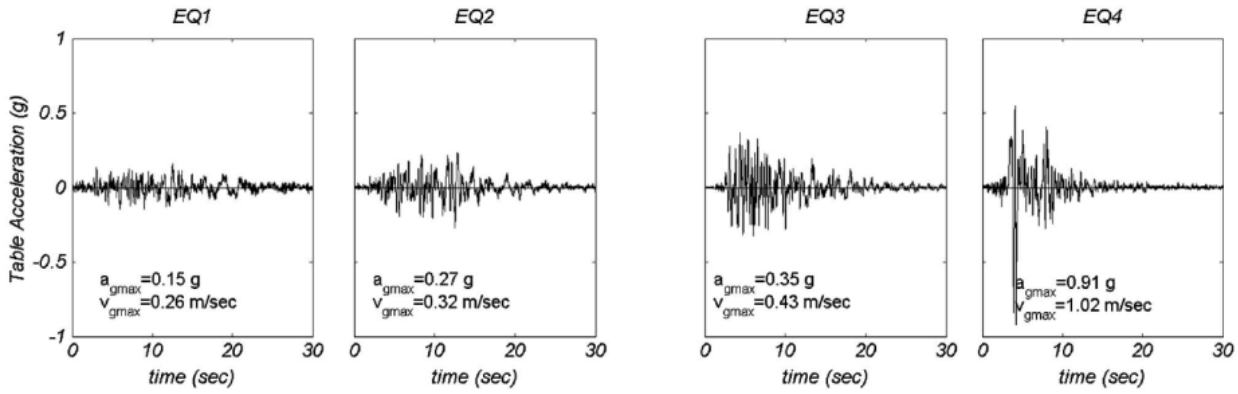

Figure 5.18: Applied Earthquake Ground Motions. Panagiotou, M., Restrepo, J., and Conte, J. (2010), "Shake-Table Test of a Full-Scale 7-Story Building Slice. Phase I: Rectangular Wall." *Journal of Structural Engineering* 137 (6): 691–704. Used under fair use, 2014.

5.3.1: Description of Finite Element Model and Nonlinear Static Analysis Results/Comparison

The reinforced concrete wall-slab building slice was modeled as seen in Figure 5.19. The positive loading direction was in the West direction. Shell elements were used to model all of the slabs, walls and slot connections. The approximate element size was 12 inches for the web and

flange walls. Steel truss elements utilizing the Dodd-Restrepo material model were used to model the longitudinal and transverse steel reinforcement in the web and flange walls. The steel reinforcement in the slabs and slot connections was smeared. The precast segment wall was assumed to be elastic. The gravity columns and diaphragm trusses, which connected the slabs to the precast segment wall, were both modeled as elastic truss elements. A -3.0 inch offset was utilized when modeling the slot connections. The outer regions (pink regions) of the web wall and the flange wall at the first and seventh levels represented confined concrete, which is consistent with the specimen. The remaining regions of the web and flange walls were unconfined concrete. The slabs did not include any confined concrete, which is consistent with the specimen.

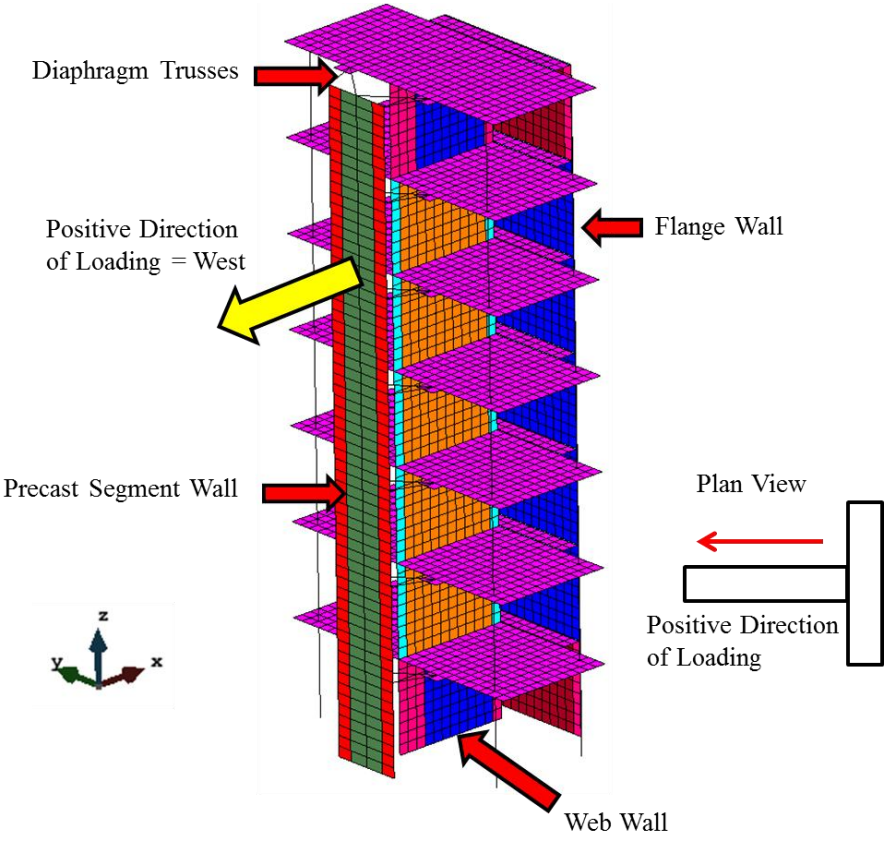

Figure 5.19: Finite Element Model of Seven-story Reinforced Concrete Wall-Slab Building Slice

The material properties for the unconfined concrete were kept consistent with the material tests performed by Panagiotou et al. (2007) where the compressive strength was 5.5 ksi and the tensile strength was 0.55 ksi. Compressive softening was included in the material model for the unconfined concrete with a crushing strain of approximately 0.003. The confined concrete utilized the same material properties but the compressive strength was increased to 7.0 ksi according to the model proposed by Mander et al. (1988) and in addition the compressive softening was eliminated. According to the Mander et al. (1988) model, the softening of confined concrete remains relatively flat until ultimate failure (when the first hoop fractures). For this reason, the compressive softening portion of the stress-strain curve for the confined concrete was assumed to be flat. This was employed to simplify the analysis and prevent strength degradation due to localization of strain in certain confined concrete elements. The calculated ultimate compressive strain using Mander et al. (1988) model was 0.011, which was not exceeded during the analyses, as shown below. Although the model did not account for either the slight softening of the confined concrete after the peak compressive strength was exceeded, or the sudden drop in compressive strength when the first hoop fractured, this confined concrete material model generated satisfactory results. A Young's modulus of 4,000 ksi was used for all of the concrete including the elastic, precast segment wall. The tension softening factor, m_t, was taken to be 1500 for both the confined and unconfined concrete regions. Geometric nonlinearities (large rotations and displacements) were accounted for using the aforementioned corotational approach. The biaxial effect was also implemented in which the peak compressive strength is reduced in cracked concrete due to the concrete being in a state of biaxial stress.

The longitudinal and transverse reinforcement in the web and flange walls was modeled using truss elements with the Dodd-Restrepo material model. The longitudinal and transverse

reinforcement in the slabs was modeled as smeared reinforcement with an elasto-perfectly plastic material model. The material properties of the steel reinforcement in the model were consistent with the material test data from Panagiotou et al. (2007). The modulus of elasticity of the steel reinforcement was set equal to 29,000 ksi. The reinforcement ratios were also consistent with the specimen.

A nonlinear static pushover analysis was performed on the analytical model. The load was applied at the fifth level, which was 70% of the height. Such analyses can provide valuable insight on the nonlinear behavior of a structure without resorting to a computationally intensive dynamic analysis. A nonlinear static analysis can also accurately reproduce the envelope of the hysteretic response of the actual structure when subjected to dynamic loading. The base moment vs. roof drift ratio analytical results were then compared to the experimental, dynamic results as seen in Figure 5.20. The base moment was determined by summing the resolved, horizontal axial forces from the diaphragm trusses at each level multiplied by the respective height. The diaphragm trusses connect the precast segment wall to the slabs and can be seen in Figure 5.19.

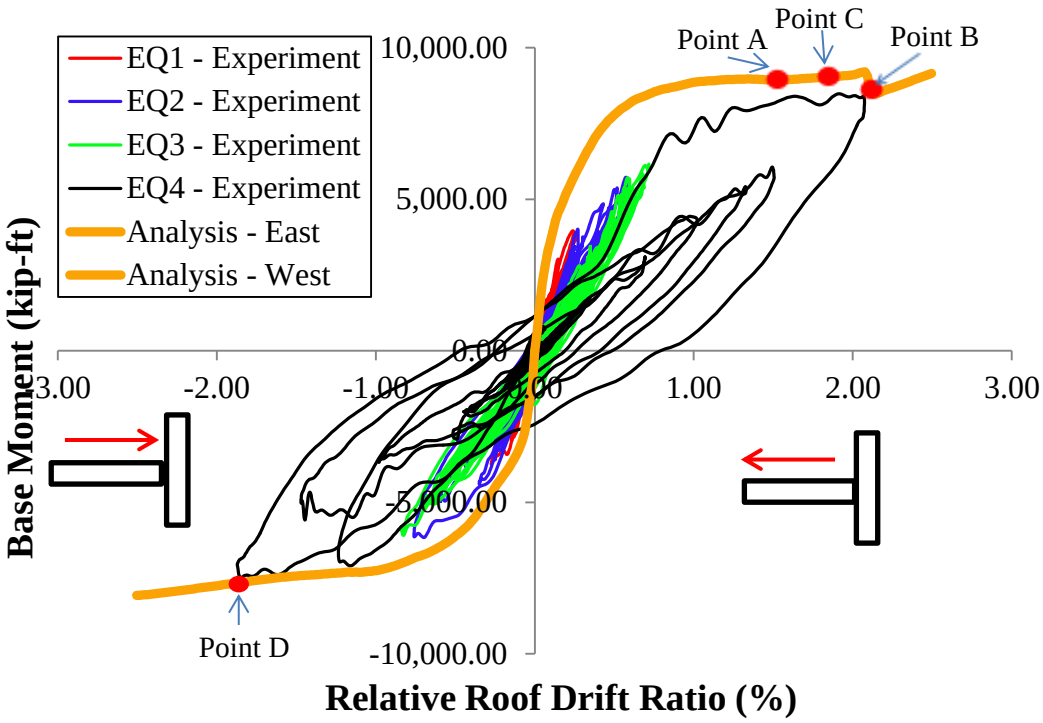

Figure 5.20: Seven-story Reinforced Concrete Wall-Slab Building Slice – Base Moment vs. Roof Drift Ratio

As seen in Figure 5.20, the analytical model was able to satisfactorily reproduce the envelope of the hysteretic response of the specimen. The analytical model was slightly stiffer at smaller roof drift ratios than the experimental results when the structure was loaded in the positive direction. This was likely caused by the assumption that the steel remains perfectly bonded to the concrete and bond-slip is neglected. In fact, when the wall is loaded in the positive direction, the longitudinal steel in the flange as well as a portion of the longitudinal steel in the web wall goes into tension, leading to a stiffer response under the perfect bond assumption.

When the structure was loaded in the west (positive) direction, the strength suddenly reduced at a roof drift ratio of approximately 2.0%. This was caused by localization of compressive strain in the bottom of the second level. It is important to note there was no confinement in the second through sixth levels of the wall-slab building slice. This localization

of compressive strain is displayed in Figure 5.21. Figure 5.21(a) represents the minimum principal strain at a roof drift ratio of approximately 1.51% (Point A) while Figure 5.21(b) represents the minimum principal strain at a roof drift ratio of approximately 2.0% (Point B). At Point A, the compressive strain localizes in the first and second levels. At Point B, the compressive strain localizes in the second level, causing a significant amount of strength reduction in those outer concrete elements. Points A and B are seen in Figure 5.20 as well.

Also seen in Figure 5.20, the lateral strength begins to increase again shortly after this localization of strain in the second level. This is due to the material of the vertical reinforcing bars reaching the strain-hardening region, thus increasing the strength of the structure. A sudden drop in strength due to high compressive strains did not occur when the wall was loaded in the negative direction. This was likely caused by the slot connections and flange wall being engaged in the compressive response of the structure. It can also be seen from Figure 5.21 that the minimum principal strains in the confined concrete regions (edges of web and flange walls on first and seventh levels) did not exceed the ultimate compressive strain (0.011) calculated from the Mander et al. (1988) model. This proves that eliminating the compressive softening of the material model for confined concrete is an adequate assumption.

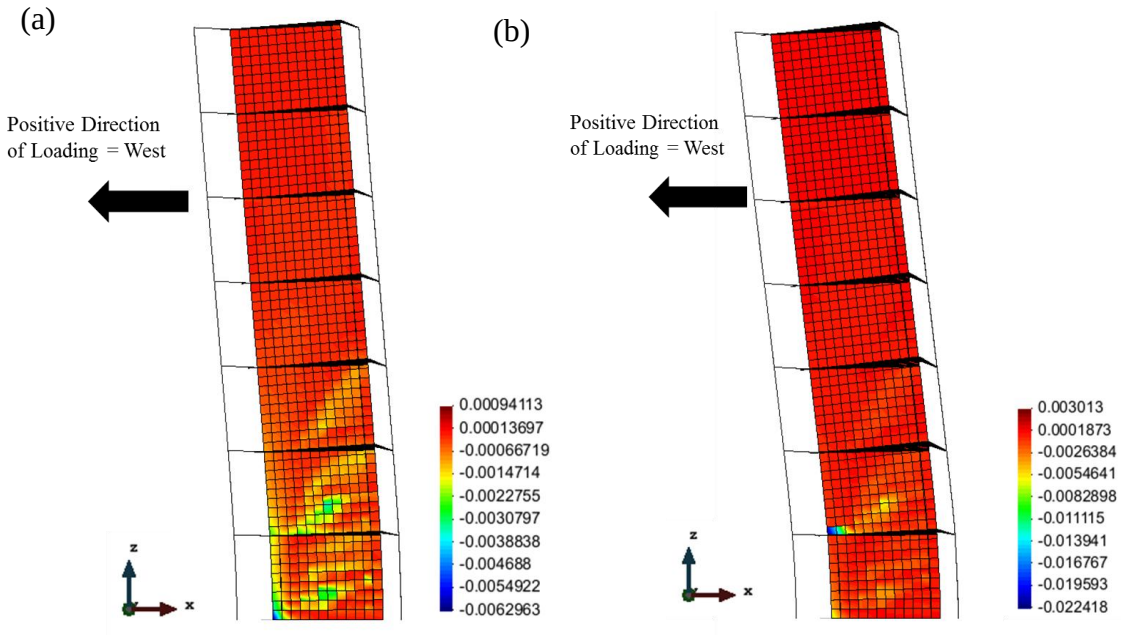

Figure 5.21: Minimum Principal Strain Contour Plot and Deformed Shape at (a) Point A and (b) Point B (deformation scaled by 5)

The capability of the model to reproduce damage/crack patterns of the actual reinforced concrete wall-slab building slice was also examined. Figures 5.22(a) and 5.22(b) represent the maximum principal strain of the analytical model at a drift ratio of 1.80% loaded in the positive (Point C) and negative (Point D) directions respectively. Points C and D are also seen in Figure 5.20. Figures 5.23 and 5.24 depict the damage pattern of the actual web wall on the first and second levels, respectively, after final loading. As seen in Figures 5.23 and 5.24, the damage/crack pattern is flexure-dominated with horizontal cracks near the outside regions at levels one and two of the web wall. Comparing Figures 5.22, 5.23 and 5.24, it can be seen that the analytical model captured this flexure-dominated crack pattern fairly well. As seen in Figure 5.22, the cracks extended to a longer depth in the web wall when the structure was loaded in the negative direction. This phenomenon can be explained by the location of the neutral axis. Due to the T-shaped wall configuration, the neutral axis lies towards the flange wall or the East end of

the web wall and thus, the depth of the tension portion of the web wall is greater when loaded in the negative direction.

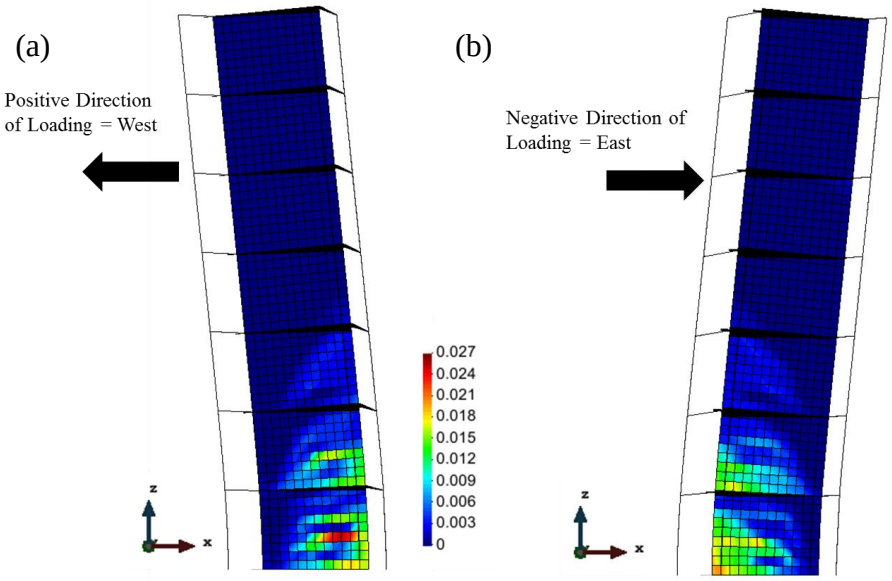

Figure 5.22: Maximum Principal Strain Contour Plot and Deformed Shape at (a) Point C and (b) Point D (deformation scaled by 5)

Figure 5.23: Crack Pattern on 1st level of Seven-story Reinforced Concrete Specimen after Final Loading. Panagiotou, M., Restrepo, J., and Conte, J. (2007), "Shake Table Test of a 7-story Full Scale Reinforced Concrete Structural Wall Building Slice Phase I: Rectangular Wall Section" *Report No. SSRP–07-07*, San Diego, CA. Used under fair use, 2014.

Figure 5.24: Crack Pattern on 2nd level of Seven-story Reinforced Concrete Specimen after Final Loading. Panagiotou, M., Restrepo, J., and Conte, J. (2007), "Shake Table Test of a 7-story Full Scale Reinforced Concrete Structural Wall Building Slice Phase I: Rectangular Wall Section" *Report No. SSRP–07-07*, San Diego, CA. Used under fair use, 2014.

5.4: Two-story Reinforced Masonry Wall-Slab Building System

The element and material formulations were also validated using the experimental results of a two-story reinforced masonry (fully-grouted) wall-slab building system. The experiment was performed at the Large Outdoor Shake Table of the University of California at San Diego (Mavros 2013). The experimental results and figures were obtained from Mavros (2013). A plan view of the reinforced masonry wall-slab building system can be seen in Figure 5.25. The middle wall was the web wall and the two, orthogonal walls were the flange walls. An elevation view of the web wall and one set of flange walls, respectively, can be seen in Figures 5.26 and 5.27. There were openings included in both sets of walls to simulate doors and windows that exist in actual reinforced masonry buildings. Pertinent masonry prism material properties at each floor can be seen in Table 5.2.

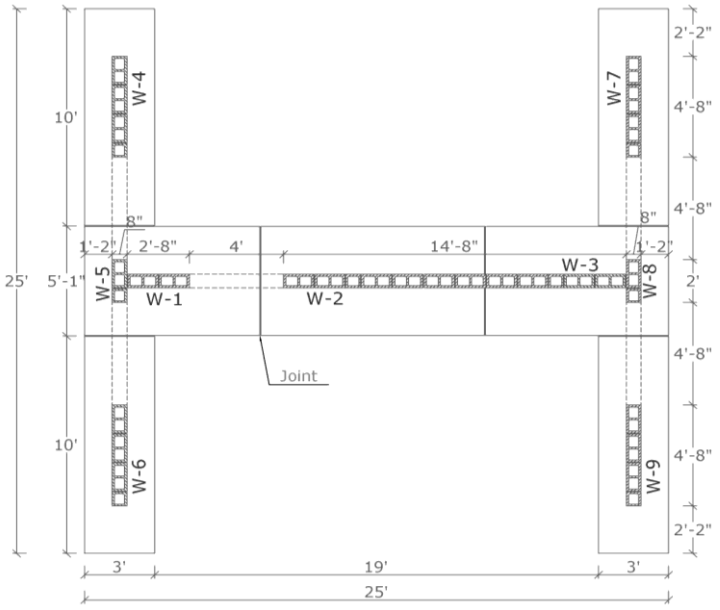

Figure 5.25: Plan View of Two-story Reinforced Masonry Wall-Slab Building System. Mavros, M. 2013. Personal Communication. Used under fair use, 2014.

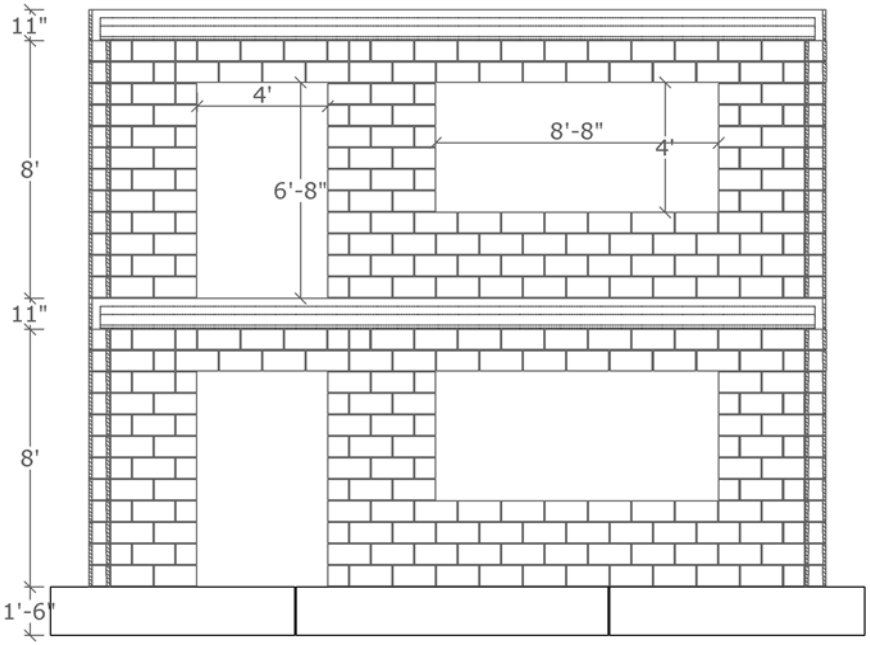

Figure 5.26: Elevation View of Web Wall Sections. Mavros, M. 2013. Personal Communication. Used under fair use, 2014.

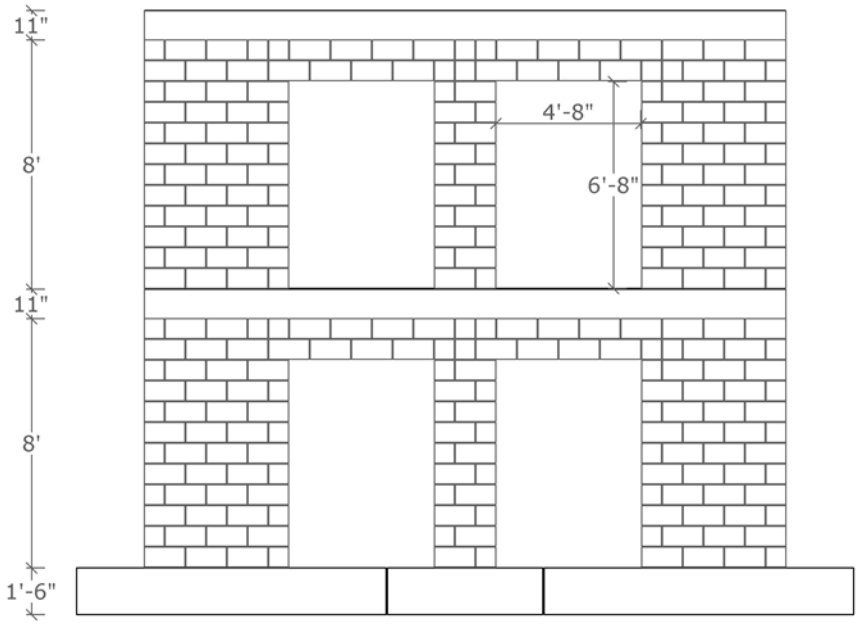

Figure 5.27: Elevation View of a Flange Wall. Mavros, M. 2013. Personal Communication. Used under fair use, 2014.

Table 5.2: Masonry Prism Material Properties for a Two-story Reinforced Masonry Wall-slab Building System. Mavros, M. 2013. Personal Communication. Used under fair use, 2014.

Floor	Modulus of Elasticity (ksi)	Compressive Strength (ksi)	Strain at Peak Compressive Strength
2	1095.0	1.62	0.0018
1	1100.0	2.26	0.0023

Both the flange walls and the web wall were reinforced (horizontal and vertical) using #4 steel reinforcing bars. Figures 5.28 and 5.29, respectively, show an elevation view of the reinforcing details for both the web wall and a flange wall. The roof/floor system utilized an eight inch deep hollow core plank with a three inch thick concrete topping. Reinforced concrete beams were cast above the web wall at each level. The hollow core planks were 40 inches wide

and were reinforced with eight 3/8 inch diameter 270 K strands and two 5/16 inch diameter 250 K strands. More details on the hollow core planks can be found from Mavros (2013). The three inch deep concrete topping was reinforced with #4 steel bars at every 16 inches running parallel to the web wall. The reinforced concrete beams above the web wall at each story were reinforced using four #4 steel bars (one at each corner of the cross section). The compressive strength of concrete was 4.0 ksi. It is important to note the floor and roof systems (along with the respective steel reinforcement) ran parallel to the web wall. Reinforcing steel material properties can be seen in Table 5.3.

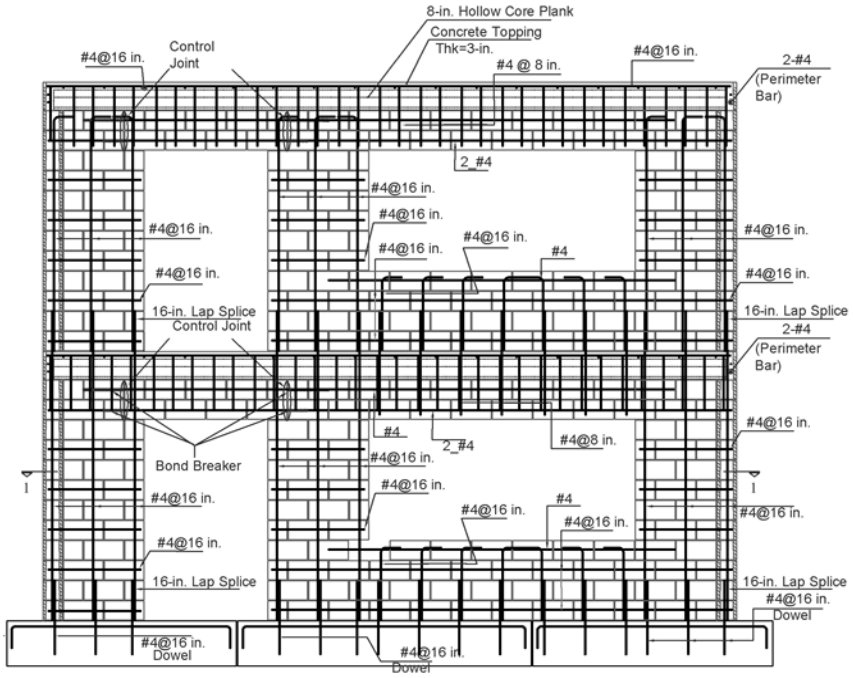

Figure 5.28: Steel Reinforcement Details of Web Wall Sections. Mavros, M. 2013. Personal Communication. Used under fair use, 2014.

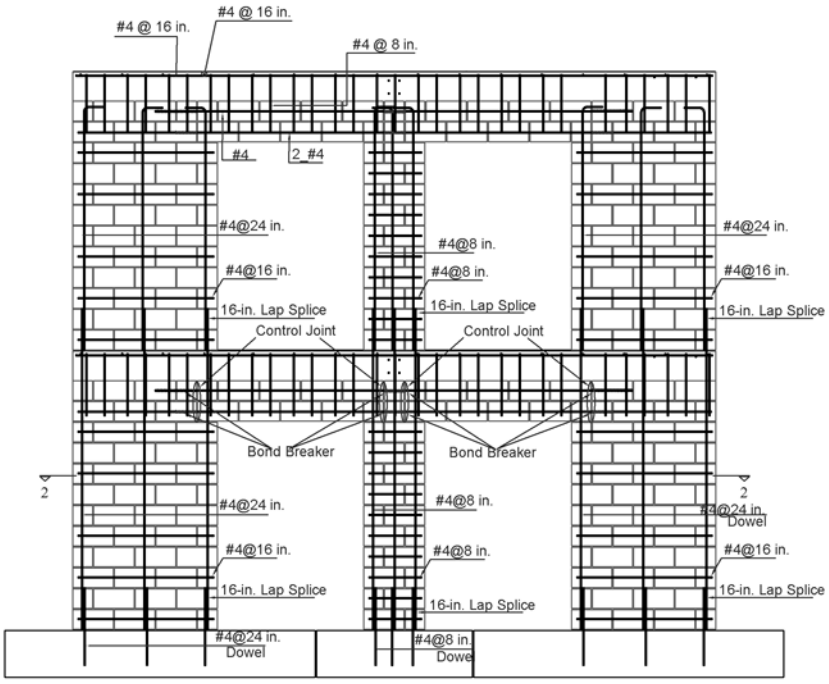

Figure 5.29: Steel Reinforced Details of Flange Walls. Mavros, M. 2013. Personal Communication. Used under fair use, 2014.

Table 5.3: Reinforcing Steel Material Properties for a Two-story Reinforced Masonry Wall-slab Building System. Mavros, M. 2013. Personal Communication. Used under fair use, 2014.

	Yield Stress (ksi)	Tensile Strength (ksi)	Modulus of Elasticity (ksi)	Ultimate Strain
Walls	65.0	98.4	28600.0	0.136
Floors	73.0	104	29400.0	0.107

The two-story reinforced masonry specimen was subjected to a series of scaled earthquake ground motions. The applied ground motions were scaled from the El Centro recording of the 1979 Imperial Valley earthquake. The ground motions were applied parallel to the web wall by use of a shake table, with the web wall expected to resist the majority of the lateral load. The magnitudes of the ground motions were initially relatively small and then gradually increased to prevent sudden collapse or failure. Although the specimen was subjected

to a plethora of scaled earthquake ground motions, the four ground motions that caused the majority of structural damage had scale factors of 0.43, 0.86, 1.08 and 1.45 on the 1979 El Centro recording. The hysteretic response of the specimen when subjected to these four ground motions was used to compare with the analytical results.

5.4.1: Description of Finite Element Model and Nonlinear Static Analysis Results/Comparison

The two-story reinforced masonry wall-slab building system was modeled as seen in Figure 5.30. Shell elements were used to model the concrete and fully-grouted masonry. The vertical and horizontal steel reinforcement in both the web and flange walls was modeled with steel truss elements using the Dodd-Restrepo material model. The eight inch hollow core plank and three inch concrete topping were modeled as one entity with the compressive strength equal to 4.0 ksi. The reinforcement in the floor and roof systems was modeled by smearing the steel reinforcement. The experimental material properties were implemented in the web and flange walls of the analytical model.

A nonlinear static analysis was performed on the analytical model with the load applied evenly at the two stories as seen in Figure 5.30. The specimen had a soft-story failure and this loading technique is an accepted way of reproducing this behavior. The nonlinear static analysis results were compared to the hysteretic load-displacement experimental results as seen in Figure 5.31. The analytical model was able to provide a satisfactory envelope of the nonlinear hysteretic response of the actual two-story reinforced masonry wall-slab building system. When the wall was loaded in the negative direction, the strength was overestimated at drift ratios less than approximately -0.15%. When the wall was loaded in the positive direction, the strength was overestimated at drift ratios greater than 0.25%. This overestimation of strength at larger drift

ratios is due to the tendency of smeared-crack continuum elements to overestimate strengths when large diagonal shear cracks occur. This phenomenon is due to the weak representation of displacement discontinuities in the smeared-crack approach, in which cracks are smeared over a nonzero crack-band length. These effects can be more pronounced when elements experiencing large diagonal cracks are confined by adjacent elements.

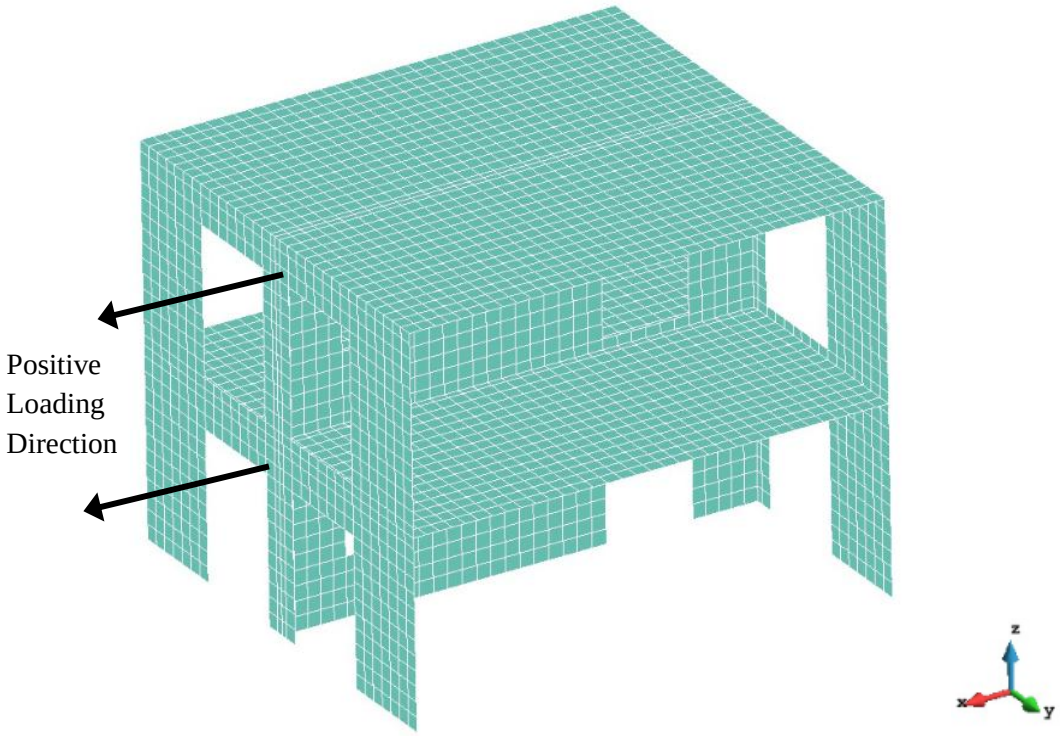

Figure 5.30: Finite Element Model of Two-story Reinforced Masonry Wall-Slab Building System

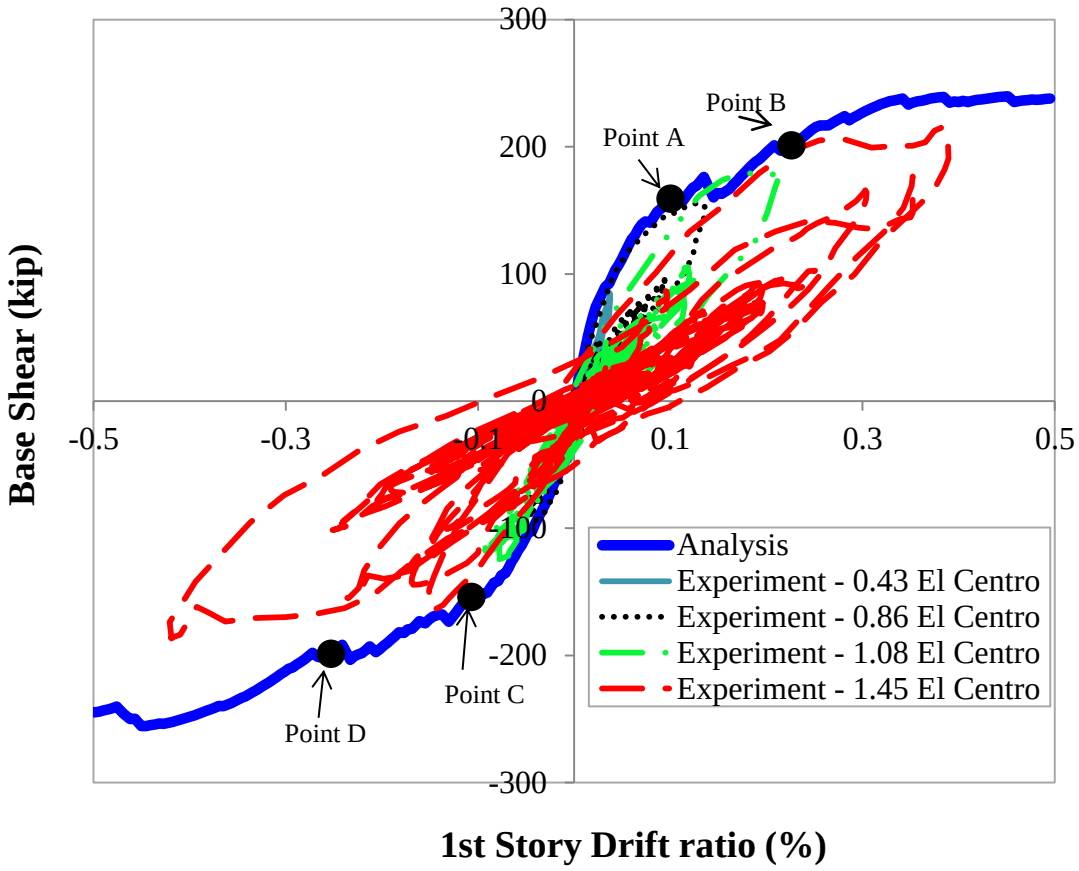

Figure 5.31: Nonlinear Static Analysis Results of Two-Story Reinforced Masonry Specimen

The capability of the model to reproduce crack patterns from the specimen was also examined. In doing so, the crack progression results were compared at Points A, B, C and D in Figure 5.31. Figures 5.32, 5.33 and 5.34 display the maximum principal strain contour plots at Point A, Point B and final loading when the web wall was loaded in the positive direction. These figures provide the progression of diagonal shear cracks in the W-2 (Figure 5.25) and W-3 (Figure 5.25) piers on the first level as the load increases in the positive direction. Figures 5.35, 5.36 and 5.37 display the maximum principal strain contour plots at Point C, Point D and final loading when the web wall was loaded in the negative direction. These figures provide the

progression of diagonal shear cracks in W-1 (Figure 5.25), W-2 and W-3 on the first level as the load increases in the negative direction. As seen in Figure 5.38, the specimen suffered significant diagonal cracks in W-2 and W-3 and minor flexural cracking at the base of W-1 and cracking near the second floor openings. Comparing Figures 5.34 and 5.37 to Figure 5.38, it can be deduced that these cracking patterns were captured fairly well by the analytical model.

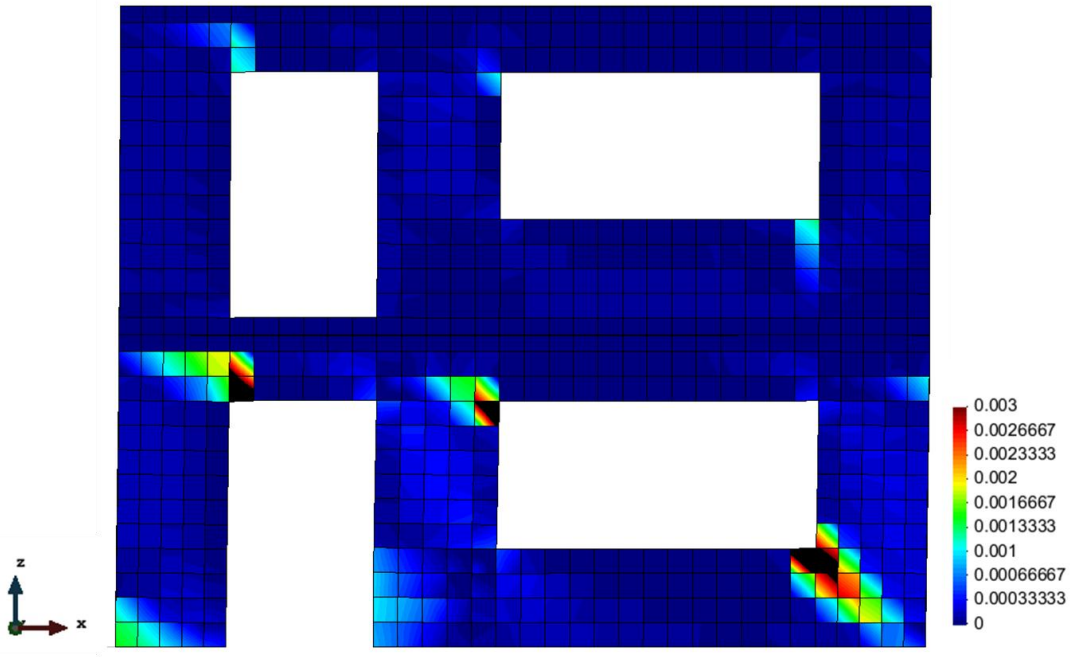

Figure 5.32: Deformed Shape and Maximum Principal Strain Contour Plot at Point A (deformation scale factor = 10)

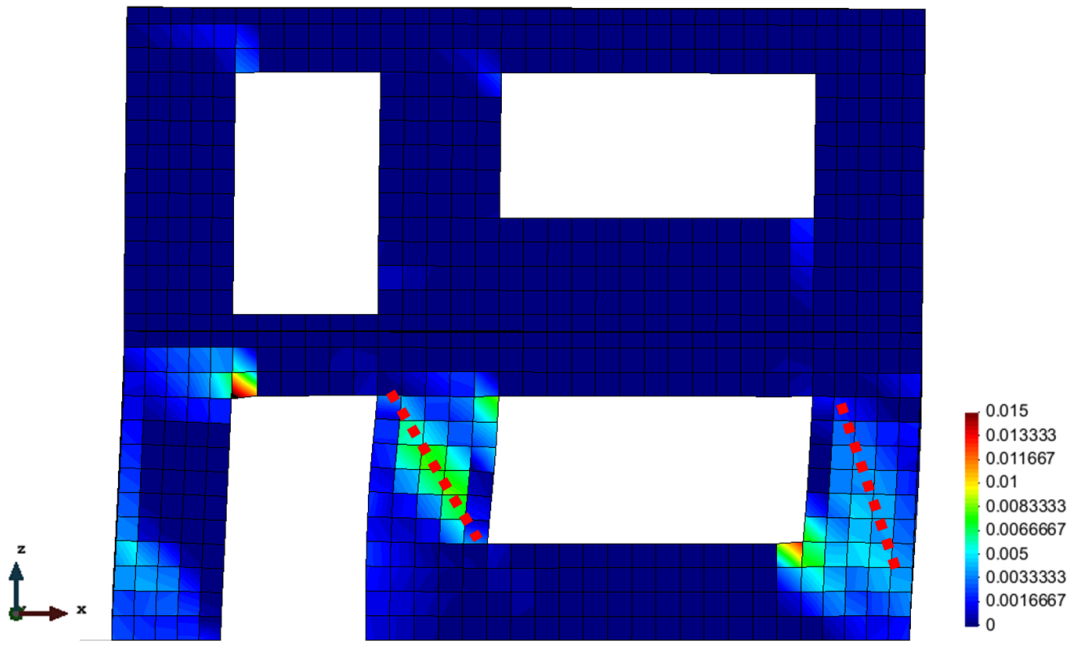

Figure 5.33: Deformed Shape and Maximum Principal Strain Contour Plot at Point B (deformation scale factor = 10)

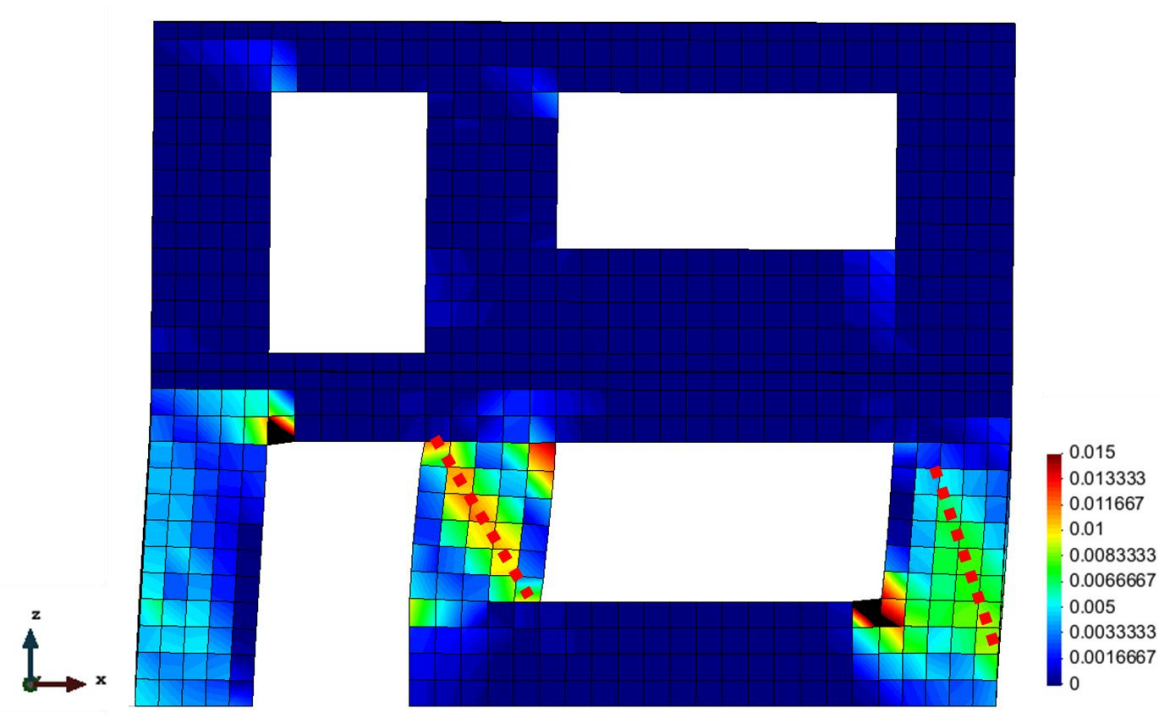

Figure 5.34: Final Deformed Shape and Maximum Principal Strain Contour Plot of Web Wall Loaded in Positive Direction (deformation scale factor = 10)

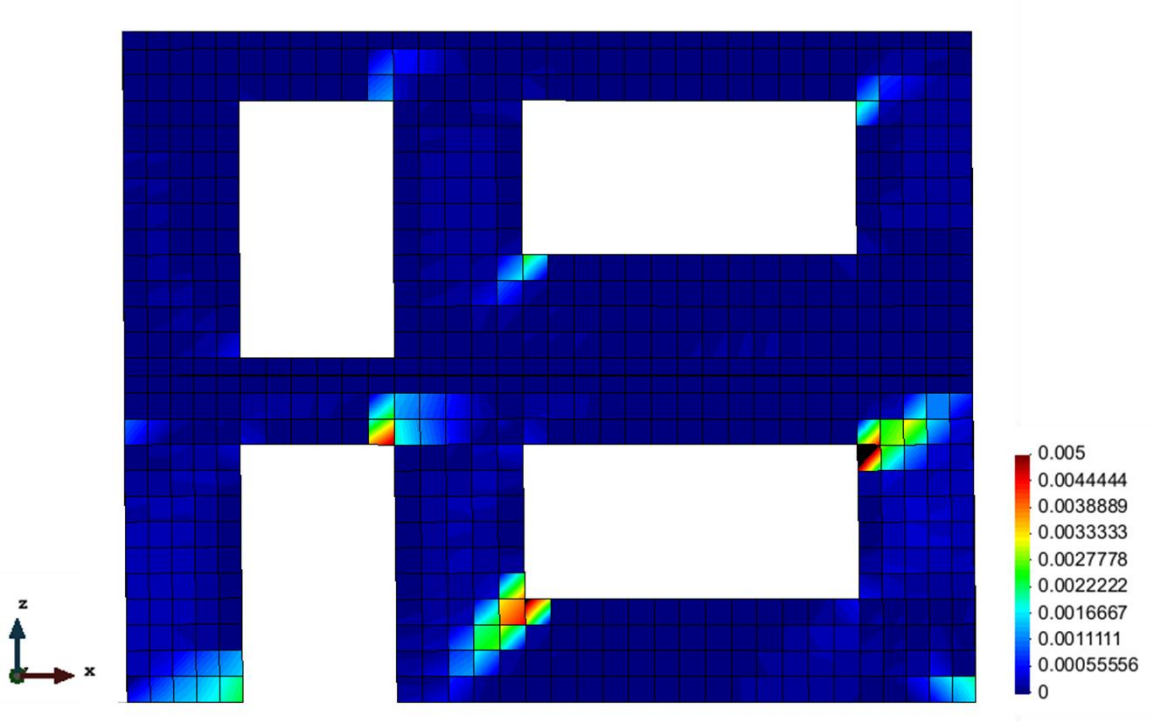

Figure 5.35: Deformed Shape and Maximum Principal Strain Contour Plot at Point C (deformation scale factor = 10)

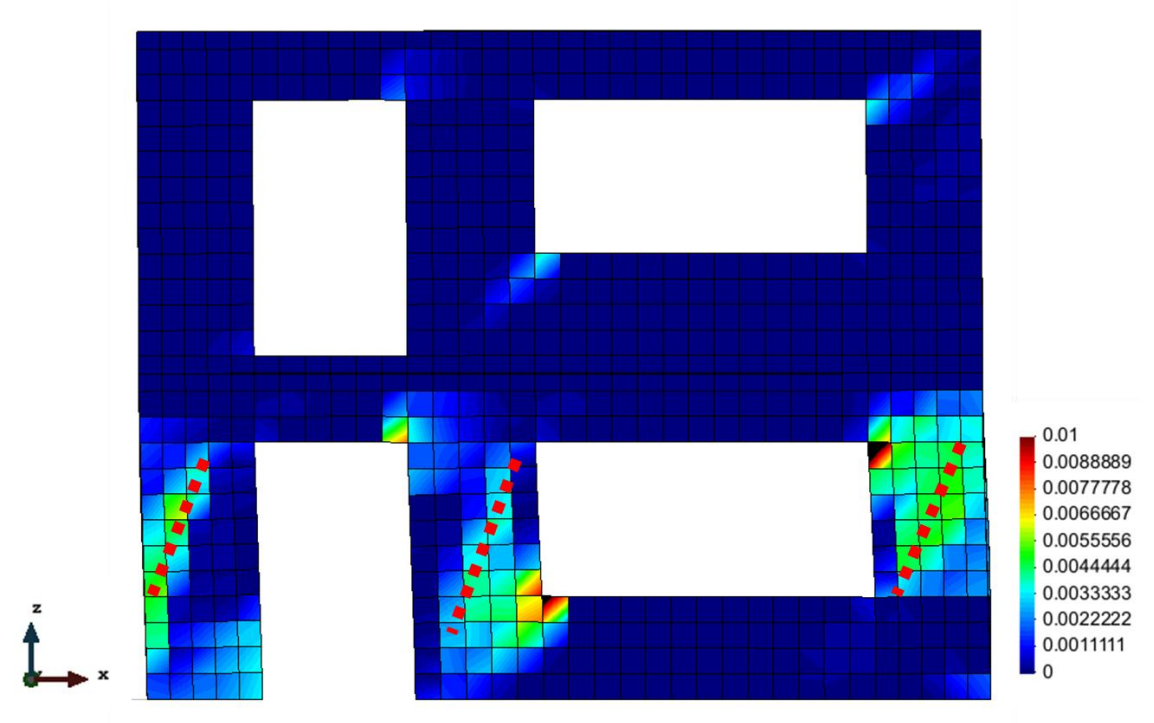

Figure 5.36: Deformed Shape and Maximum Principal Strain Contour Plot at Point D (deformation scale factor = 10)

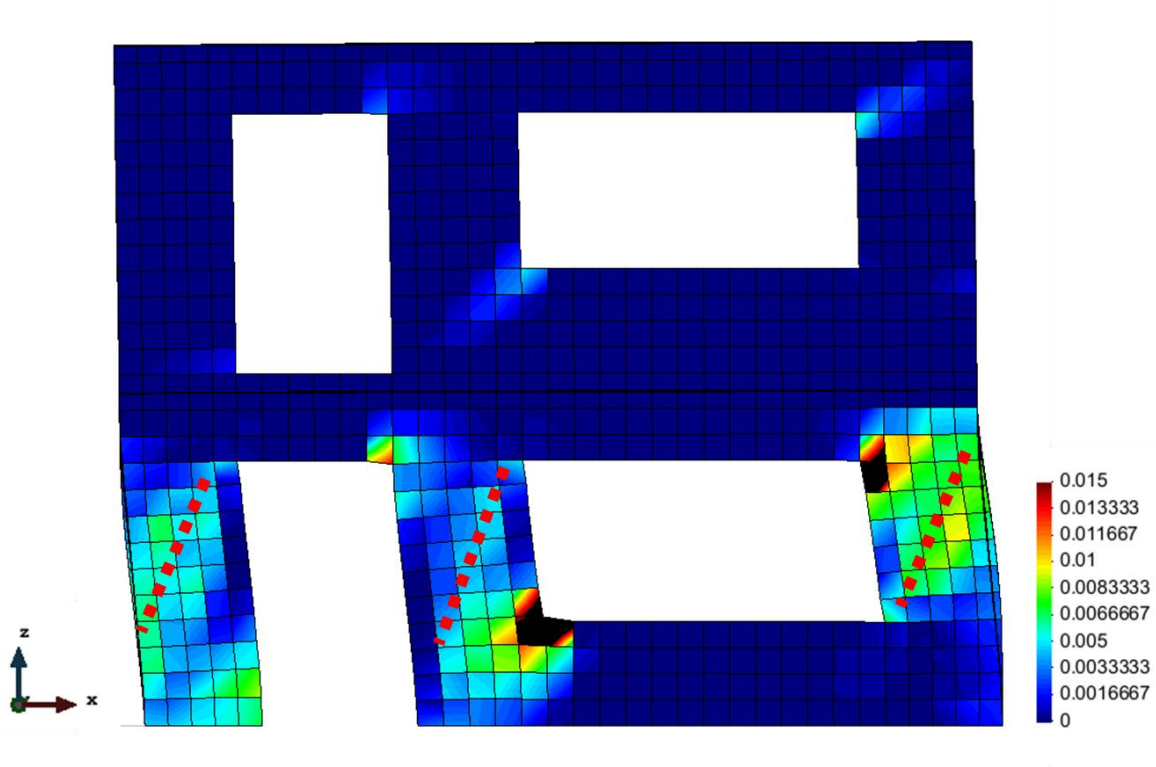

Figure 5.37: Final Deformed Shape and Maximum Principal Strain Contour Plot of Web Wall Loaded in Negative Direction (deformation scale factor = 10)

Figure 5.38: Structural Damage of Web Wall after Final Ground Motion. Mavros, M. 2013. Personal Communication. Used under fair use, 2014.

The model was then utilized to gain a better understanding of how the load traveled through the web wall and into the foundation. Figures 5.39 and 5.40 contain the minimum principal membrane force contour plots of the web wall loaded in the positive and negative directions, respectively. The force was distributed through the wall by idealized compression struts and the vertical and horizontal steel truss elements. The idealized compression struts in the piers tend to be of the same orientation for both levels except for the second level of W-2 when the web wall was loaded in the positive direction. The idealized diagonal compression strut in this location occurs at a slightly smaller angle than the other idealized compression struts in the piers and this is likely due to the unsymmetrical nature of the structure.

Figures 5.41 and 5.42 detail the stresses in the vertical and horizontal steel truss elements. Yielding of the reinforcing bars occurs along the predicted crack patterns in W2 and W3 on level 1 as well as near certain openings. This is due to a high concentration of strain in these locations as seen in Figures 5.34 and 5.37. The knowledge gained from understanding the orientation of the idealized compression struts and the load transfer in the reinforcing bars could be used to improve simplified models such as strut and tie models for the analysis/design of similar structures. Simplified models are often used by practitioners in lieu of three-dimensional finite element models to reduce computational costs.

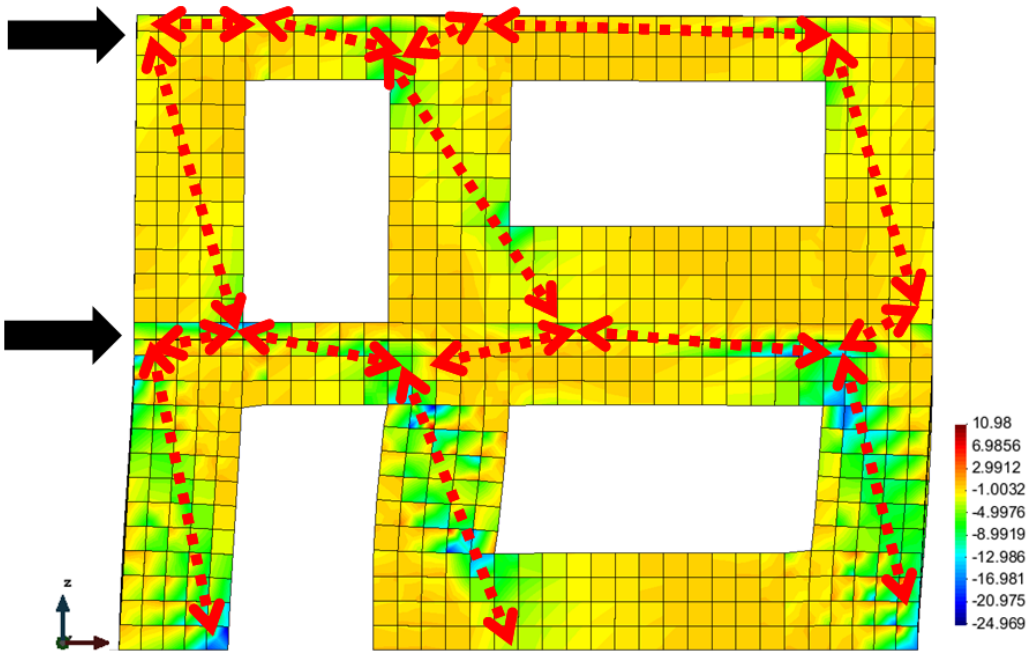

Figure 5.39: Final Deformed Shape and Minimum Principal Membrane Force Contour Plot of Web Wall loaded in the Positive Direction (deformation scale factor = 10)

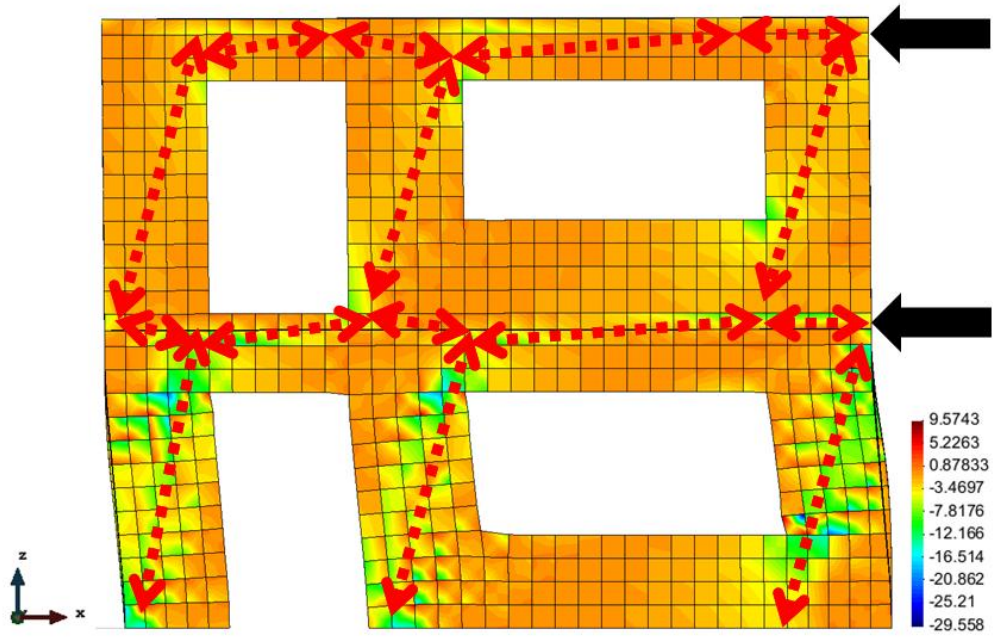

Figure 5.40: Final Deformed Shape and Minimum Principal Membrane Force Contour Plot of Web Wall loaded in the Negative Direction (deformation scale factor = 10)

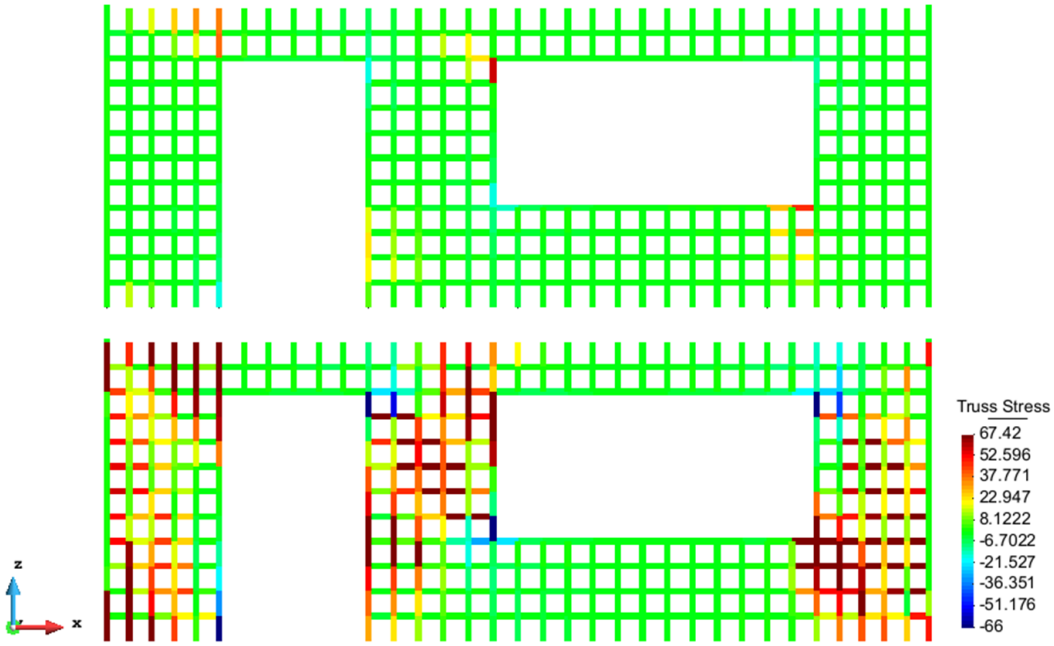

Figure 5.41: Steel Stresses when the Wall is loaded in the Positive Direction

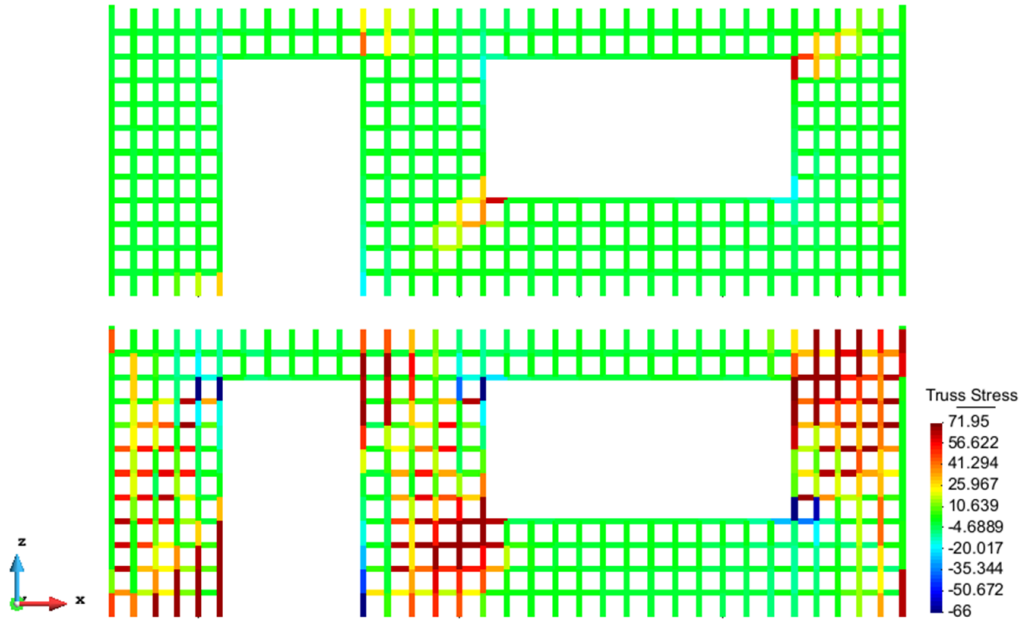

Figure 5.42: Steel Stresses when the Wall is loaded in the Negative Direction

The strength coupling effect between the floor systems and the web wall masonry piers (W-1, W-2, and W-3) was examined by plotting the moment M_{yy} contours of the first and second level floor systems as shown in Figures 5.43 and 5.44. The red dashed lines in these figures represent the three masonry piers in the web wall (wall loaded in-plane). In these figures, higher magnitudes of coupling moments near the edges of each pier were observed with decreasing magnitudes at further distances along the Y-axis from the web wall. The concentration of these moments at the vicinity of the web wall indicates the building actually behaves as one system in resisting the lateral load. In fact, the flange walls (walls loaded out-of-plane) add to the lateral resistance of the building through the intermediate slabs that connect the different vertical components at each story level. This phenomenon can be clearly seen in Figures 5.43 and 5.44 where concentrations of maximum moments also occur near the flange walls.

The coupling effect between the flange walls and the slabs as well as between the slabs and the wall piers is of great significance to represent actual lateral system behavior. Three-dimensional models, such as the model presented herein, capture such coupling effects and provide insights on how to account for coupling in simpler two-dimensional models. For instance, two-dimensional models approximate the coupling effect of the slabs through a system of connecting beams with an effective width. Three-dimensional models provide methods to determine the appropriate value of the beam effective width, which should cover the area where high coupling moment magnitudes occur.

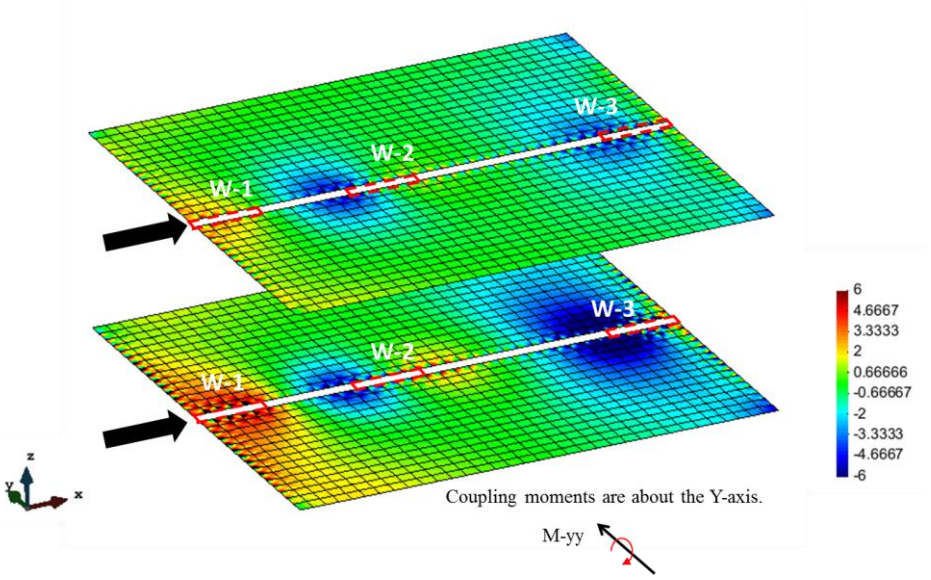

Figure 5.43: Coupling Moments in Slabs at a Drift Ratio of 0.5%

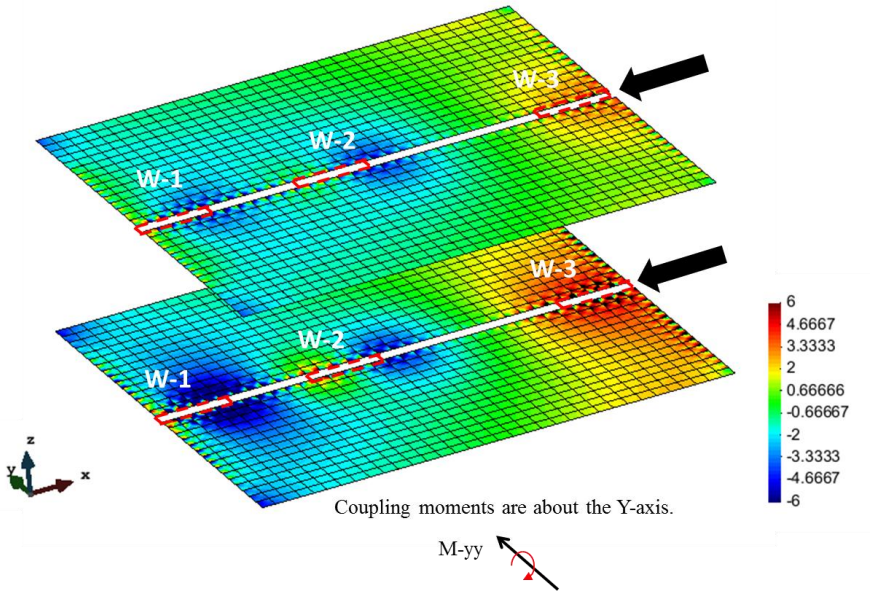

Figure 5.44: Coupling Moments in Slabs at a Drift Ratio of -0.5%

Chapter 6: Conclusions and Recommendations for Future Research

6.1: Summary and Conclusions

This thesis presented the formulation and validation of an enhanced 4-node Discrete Kirchhoff quadrilateral shell element intended to model the nonlinear response of reinforced concrete and fully-grouted reinforced masonry structures under quasi-static and dynamic loadings. The element enhancements consist of a corotational approach to account for geometric nonlinearities and nonlinear material models for both concrete/masonry and the reinforcing steel.

The validation studies of this model compared experimental data and theoretical solutions with linear and nonlinear finite element analyses. The elastic response of the proposed shell element was checked against theoretical and benchmark linear elastic results. The corotational approach validations succeeded in capturing the three-dimensional rigid body rotation of a single element and in replicating benchmark results of an elastic cantilever wall. The nonlinear response of the element was verified by several two-dimensional nonlinear (material and geometric) analyses of an isolated reinforced concrete column. The computational results were in good agreement with the hysteretic load-displacement behavior of the quasi-static experimental results indicating that the Dodd-Restrepo material model was able to better capture the nonlinear response of the specimen.

The shell element was also used to analyze two shear wall structures: a seven-story reinforced concrete wall-slab building slice, and a two-story reinforced masonry (fully-grouted) wall-slab building system. Nonlinear static analyses performed on these structures show that the model is able to reproduce the envelope of the hysteretic response of the experimental dynamic results. Further, the model was able to capture the axial-shear-flexural interactions including flexure-dominated and shear-dominated damage patterns.

The enhanced shell element proposed in this thesis accurately simulates nonlinear reinforced concrete/masonry shear wall structures. It not only allows researchers and industry to better understand reinforced concrete/masonry shear wall behavior but also provides a viable tool to perform sensitivity analyses leading to structurally efficient and cost effective designs.

6.2: Recommendations for Future Research

The research work presented in this thesis validates the formulation of the enhanced shell element to reproduce dynamic experimental results using nonlinear static analyses. Further research is recommended to verify the results of the model using nonlinear dynamic analyses. Once dynamic analyses are validated, the shell element could be utilized to gain even further knowledge of the actual hysteretic behavior of reinforced concrete/masonry buildings subjected to significant dynamic loading events.

The formulation of the current element implements the smeared-cracked approach to model concrete/masonry nonlinearities. This approach tends to overestimate the strength and ductility of shear-dominated wall structures. More research is needed to update the material models to better represent the nonlinear response of brittle shear wall structures undergoing large shear cracks. A systematic comparison with other material models, such as the damage-plasticity model, can further clarify the applicability of the proposed smeared-crack model.

Additional work to improve the computational efficiency of the proposed shell element is also suggested. A possible way to reduce computational cost is to implement a 1x1 (one integration point) two-dimensional Gauss quadrature rule instead of the 2x2 (four integration points) quadrature rule currently applied. This implementation is expected to decrease computational time by approximately 75%.

REFERENCES

Batoz, J.-L., and Tahar, B. (1982), "Evaluation of a New Quadrilateral Thin Plate Bending Element." *International Journal for Numerical Methods in Engineering* 18 (11): 1655–77.

Belytschko, T., and Hsieh, B.J. (1973), "Non-linear Transient Finite Element Analysis with Convected Co-ordinates." *International Journal for Numerical Methods in Engineering* 7 (3): 255–271.

Cervera, M., Hinton, E., and Hassan, O. (1987), "Nonlinear Analysis of Reinforced Concrete Plate and Shell Structures Using 20-noded Isoparametric Brick Elements." Computers & Structures 25 (6): 845–869.

Chang, T.Y., Taniguchi, H. and Chen, W.F. (1987), "Nonlinear Finite Element Analysis of Reinforced Concrete Panels." Journal of Structural Engineering 113 (1): 122–140.

Clough, R., Benuska, K., and Wilson, E. (1965), "Inelastic Earthquake Response of Tall Buildings." In Proceedings, Third World Conference on Earthquake Engineering, New Zealand. Vol. 11.

Fish, J., and Belytschko, T. (2007), *A First Course in Finite Elements*. John Wiley and Sons.

Hu, H.-T., and Schnobrich, W.C. (1991), "Nonlinear Finite Element Analysis of Reinforced Concrete Plates and Shells Under Monotonic Loading." Computers & Structures 38 (5): 637–651.

Hughes, T. (2000), *The Finite Element Method: Linear Static and Dynamic Finite Element Analysis*. Dover Publications, Inc.

Ile, N., and Reynouard, J. (2000), "Nonlinear Analysis of Reinforced Concrete Shear Wall under Earthquake Loading." *Journal of Earthquake Engineering* 4 (2): 183–213.

Kim, T.-H., Lee, K.-M., and Shin, H.M. (2002), "Nonlinear Analysis of Reinforced Concrete Shells Using Layered Elements with Drilling Degree of Freedom." ACI Structural Journal 99 (4).

Koutromanos, I., and Shing, B. (2010), "Trial Application: Reinforced Masonry Shear Wall Structures." In Evaluation of the FEMA P-695 Methodology for Quantification of Building Seismic Performance Factors. *National Institute of Standards and Technology, USA.*

Koutromanos, I. (2011), "Numerical Analysis of Masonry-Infilled Reinforced Concrete Frames Subjected to Seismic Loads and Experimental Evaluation of Retrofit Techniques." *Ph.D. Dissertation*, University of California, San Diego, La Jolla, CA, 355pp.

Koutromanos, I. 2013. Personal Communication.

Koutromanos, I. 2014. Personal Communication.

Lee, J., and Fenves, G. (1998), "Plastic-Damage Model for Cyclic Loading of Concrete Structures." *Journal of Engineering Mechanics* 124 (8): 892–900.

Liu, Y., and Teng, S. (2008), "Nonlinear Analysis of Reinforced Concrete Slabs Using Nonlayered Shell Element." Journal of Structural Engineering 134 (7): 1092–1100.

Lotfi, H. R., and Shing, P. B. (1991), "An Appraisal of Smeared Crack Models for Masonry Shear Wall Analysis." *Computers & Structures* 41 (3): 413–25. doi:10.1016/0045-7949(91)90134-8.

Lubliner, J., Oliver, J., Oller, S., and Oñate, E. (1989), "A Plastic-Damage Model for Concrete." *International Journal of Solids and Structures* 25 (3): 299–326. doi:10.1016/0020-7683(89)90050-4.

Mahin, S., and Bertero, V. (1975), *An Evaluation of Some Methods for Predicting Seismic Behavior of Reinforced Concrete Buildings.* Vol. 75. Earthquake Engineering Research Center, College of Engineering, University of California.

Mander, J., Priestley, M. , and Park, R. (1988), "Theoretical Stress-Strain Model for Confined Concrete." *Journal of Structural Engineering* 114 (8): 1804–1826. doi:10.1061/(ASCE)0733-9445(1988)114:8(1804).

Massicotte, B., MacGregor, J., and Elwi, A. (1990), "Behavior of Concrete Panels Subjected to Axial and Lateral Loads." Journal of Structural Engineering 116 (9): 2324–2343.

Mavros, M. 2013. Personal Communication.

Mazars, J., Kotronis, P., and Davenne, L. (2002), "A New Modelling Strategy for the Behaviour of Shear Walls under Dynamic Loading." Earthquake Engineering & Structural Dynamics 31 (4): 937–54.

McKenna, F., Fenves, G. L., and Scott, M. H. (2000), *Open system for earthquake engineering simulation*, University of California, Berkeley, CA.

Nour-Omid, B., and Rankin, C. C. (1991), "Finite Rotation Analysis and Consistent Linearization Using Projectors." *Computer Methods in Applied Mechanics and Engineering* 93 (3): 353–84.

Otani, S., and Sozen, M. (1972), Behavior of Multistory Reinforced Concrete Frames during Earthquakes. University of Illinois.

Panagiotou, M., and Restrepo, J. (2010), "Displacement-Based Method of Analysis for Regular Reinforced-Concrete Wall Buildings: Application to a Full-Scale 7-Story Building Slice Tested at UC–San Diego." *Journal of Structural Engineering* 137 (6): 677–90.

Panagiotou, M., Restrepo, J., and Conte, J. (2007), "Shake Table Test of a 7-story Full Scale Reinforced Concrete Structural Wall Building Slice Phase I: Rectangular Wall Section" *Report No. SSRP–07-07*, San Diego, CA.

Panagiotou, M., Restrepo, J., and Conte, J. (2010), "Shake-Table Test of a Full-Scale 7-Story Building Slice. Phase I: Rectangular Wall." *Journal of Structural Engineering* 137 (6): 691–704.

Panagiotou, M., Restrepo, J., Schoettler, M., and Kim, G. (2012), "Nonlinear Cyclic Truss Model for Reinforced Concrete Walls." ACI Structural Journal: 205–214.

Polak, M., and Vecchio, F. (1993), "Nonlinear Analysis of Reinforced-Concrete Shells." Journal of Structural Engineering 119 (12): 3439–3462.

Rankin, C.C., and Brogan, F.A. (1986), "An Element Independent Corotational Procedure for the Treatment of Large Rotations." Journal of Pressure Vessel Technology 108 (2): 165–74.

Simulia. (2006), "*Abaqus student edition – Version 6.6*," Providence, RI.

Takayanagi, T., and Schnobrich, W. (1976), "Computed Behavior of Reinforced Concrete Coupled Shear Walls." Structural Research Series 434.

Taucer, F., Spacone, E., and Filippou, F. (1991), *A Fiber Beam-Column Element for Seismic Response Analysis of Reinforced Concrete Structures*. Vol. 91. 17. Earthquake Engineering Research Center, College of Engineering, University of California.

Taylor, A. W., Kuo, C., Wellenius, K., and Chung, D. M. (1997), "A Summary of Cyclic Lateral Load Tests on Rectangular Reinforced Concrete Columns," *Report NISTIR 5984*, National Institute for Standards and Technology, Gaithesburg, Maryl., 101 pp.

Taylor, R. L., (2007), *FEAP—A Finite Element Analysis Program, Version 8.1.a9*.

Vallenas, J., Bertero, V., and Popov, E. (1979), "Hysteric Behavior of Reinforced Concrete Structural Walls." NASA STI/Recon Technical Report N 80: 27533.

Vecchio, F., and Collins, M. (1986), "The Modified Compression-Field Theory for Reinforced Concrete Elements Subjected to Shear." ACI J. 83 (2): 219–31.

Vecchio, F. (1989), "Nonlinear Finite Element Analysis of Reinforced Concrete Membranes." ACI Structural Journal 86 (1): 26–35.

Vecchio, F., and Collins, M. (1982), "The Response of Reinforced Concrete to in-Plane Shear and Normal Stresses." University of Toronto, Department of Civil Engineering.

Zhang, Y., Finger, S., and Behrens, S. (2003), *Introduction to Mechanisms*. Carnegie Mellon University.